This document is downloaded from DR-NTU (https://dr.ntu.edu.sg)
Nanyang Technological University, Singapore.

Optical and dielectric properties of nanosolid silicon

Pan, Likun

2005

Pan, L. K. (2005). Optical and dielectric properties of nanosolid silicon. Doctoral thesis, Nanyang Technological University, Singapore.

https://hdl.handle.net/10356/3111

https://doi.org/10.32657/10356/3111

Nanyang Technological University

Downloaded on 28 Apr 2025 17:57:42 SGT

ATTENTION: The Singapore Copyright Act applies to the use of this document. Nanyang Technological University Library

OPTICAL AND DIELECTRIC PROPERTIES OF NANOSOLID SILICON

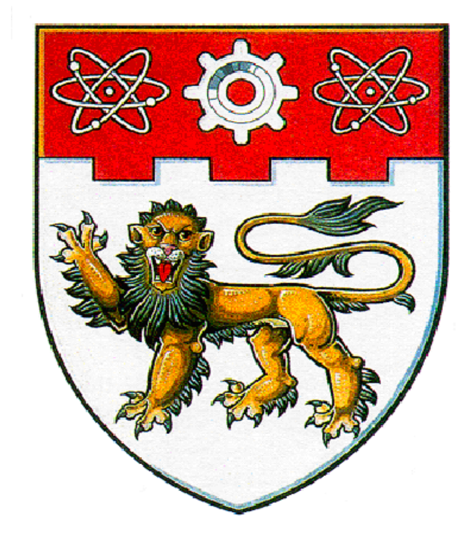

PAN LIKUN

SCHOOL OF ELECTRICAL AND ELECTRONIC ENGINEERING
NANYANG TECHNOLOGICAL UNIVERSITY

2005

ATTENTION: The Singapore Copyright Act applies to the use of this document. Nanyang Technological University Library

Optical and Dielectric Properties of Nanosolid Silicon

Pan Likun

School of Electrical & Electronic Engineering

A thesis submitted to the Nanyang Technological University

in fulfillment of the requirement for degree of

Doctor of Philosophy

2005

ATTENTION: The Singapore Copyright Act applies to the use of this document. Nanyang Technological University Library

To my parents,

for their encouragement and love

ATTENTION: The Singapore Copyright Act applies to the use of this document. Nanyang Technological University Library

Acknowledgements

I would like to express my sincere gratitude to my supervisor, Associate Professor Sun Changqing, for his invaluable instruction and support throughout the course of the research. Within these three years, I learned not only specialized knowledge but also working attitude from him. This work would not have been completed without his patient guidance and persistent encouragement.

I would like to express my sincere thanks to Dr Fu Yongqing, Dr. Yu Guoqing, Dr. Huang Haitao, and Dr. Zhang Qinyuan for their assistance and helpful discussions in the work.

I would like to thank all of my friends, graduate students, the faculty, and technicians at the Ion Beam Processing Laboratory. All of my experience and interactions with them have shaped me and my work, and helped making my graduate experience worthwhile and unforgettable.

I would also like to acknowledge the School of EEE, Nanyang Technological University, Singapore, for awarding me the research scholarship and providing me with excellent research facilities.

Finally, I would like to thank my parents for teaching me to understand the value of hard work and supporting me during my education as well as in life. Their love and support are always the greatest inspiration to me from the first day I came to the world.

ATTENTION: The Singapore Copyright Act applies to the use of this document. Nanyang Technological University Library

Summary

Nanosolid/porous silicon has been fabricated, passivated with fluorine, characterized and analyzed. Emphasis is devoted to the optical and dielectric properties depending on size and passivation conditions. Consistent insight has been obtained into the band gap (E_G) expansion, the blue shift in photoluminescence (PL) and photoabsorption (PA), the electron-phonon (e-p) interaction, and the Si-2*p* level and the Raman frequency shift as well as the dielectric suppression induced by size reduction. The size dependence has been formulated in terms of the original Bond-Order-Length-Strength (*BOLS*) correlation theory [C. Q. Sun, Phys. Rev. B 69, 045105, 2004].

It has also been found that CF_4 plasma-passivation further enhances the size dependence of the blue shift in PL and PA, the Si-2*p* level shift, the E_G expansion, the e-p interaction, and the dielectric suppression. Dielectric impedance measurements within the frequency range of 50 Hz–1.0 MHz and temperature range of 298–798 K reveal three semicircles in a Cole–Cole plot when the temperature is raised to 773 K. The enhancement in conductivity by heating follows an Arrhenius law with an activation energy transition from 0.07 to 0.79 eV at ~565 K. Moreover, a Serial-Parallel capacitance structural model for the porosity and oxidation extent dependence of dielectrics has been developed, which provides a practical means to measure the oxidation extent.

Consistency between the *BOLS* predictions and the experimental results, as well as the data sourced from the literature, shows that the E_G expansion, the PL

ATTENTION: The Singapore Copyright Act applies to the use of this document. Nanyang Technological University Library

and PA and Si-2*p* level blue shift, the Raman red shift, and the dielectric suppression relate directly to the crystal binding energy, the atomic cohesive energy, or the electron-phonon coupling. Most Strikingly, extension of the *BOLS* correlation enables the single energy level of the 2*p* electrons of an isolated Si atom and vibration frequency of a Si–Si dimer bond and their shift upon bulk and nanosolid formation to be quantified by matching predictions to the observed size and shape dependence of the XPS and Raman data, which are beyond the scope of currently available approaches.

ATTENTION: The Singapore Copyright Act applies to the use of this document. Nanyang Technological University Library

Table of Contents

Acknowledgements i

Summary ii

List of Figures viii

List of Tables xvi

Nomenclature xvii

Chapter 1 Introduction 1

1.1 Overview 1

1.2 Motivation 3

1.3 Objective 4

1.4 Major Achievement 4

1.5 Organization of the Thesis 5

Chapter 2 Theory Consideration 7

2.1 Introduction 7

2.2 Existing Models 8

2.3 “Bond-Order-Length-Strength” Correlation 15

2.3.1 Surface Bond Contraction 15

2.3.2 Hamiltonian and Band Structure 18

2.3.3 Photoluminescence, Photoabsorption and Electron-Phonon Interaction 24

2.3.4 Core Level Shift 28

2.3.5 Dielectric Suppression 30

2.3.6 Raman shift 33

2.4 Summary 38

ATTENTION: The Singapore Copyright Act applies to the use of this document. Nanyang Technological University Library

Chapter 3 Experimental Approaches 39
3.1 Sample Preparation: Porous Silicon 39
3.1.1 Electrochemical formation 39
3.1.2 Dissolution Chemistry 40
3.1.3 Pore Formation 43
3.1.4 Drying of the samples 44
3.2 Size Control 45
3.2.1 Porosity 45
3.2.2 Fabrication Method 45
3.2.3 Surface Morphology 46
3.3 Surface Passivation 48
3.4 Surface Metalization 50
3.5 Characterization Equipment 52
Chapter 4 Optical and Dielectric Properties 55
4.1 Introduction 55
4.2 Experimental Details 55
4.3 Size Dependent Property Variations 57
4.3.1 Band Gap Expansion 57
4.3.2 Core Level Shift 61
4.3.3 Dielectric suppression 63
4.3.4 Raman shift 68
4.4 Summary 70
Chapter 5 Surface Passivation 71

ATTENTION: The Singapore Copyright Act applies to the use of this document. Nanyang Technological University Library

5.1 Surface Fluorination 71

5.1.1 Introduction 71

5.1.2 Experimental Details 72

5.1.3 Results and Discussion 72

5.1.4 Summary 79

5.2 Surface Fluorination Enhanced Size Dependency 79

5.2.1 Introduction 79

5.2.2 Experimental Details 80

5.2.3 Results and discussion 80

5.2.4 Summary 85

5.3 Surface Oxidation Correlated Dielectrics 85

5.3.1 Introduction 85

5.3.2 Model 87

5.3.3 Summary 94

Chapter 6 Surface Metalization 95

6.1 Introduction 95

6.2 Experimental Details 97

6.3 Results and Discussion 97

6.3.1 Before Annealing 97

6.3.2 After Annealing 101

6.4 Summary 104

Chapter 7 Critical Anodization Temperature for Optical Transition 106

7.1 Introduction 106

ATTENTION: The Singapore Copyright Act applies to the use of this document. Nanyang Technological University Library

7.2 Experimental Details 107
7.3 Results and Discussion 107
7.3.1 Critical Anodization Temperature 107
7.3.2 Mechanism 110
7.4 Summary 111
Chapter 8 Dielectric Relaxation and Transition 112
8.1 Introduction 112
8.2 Experimental Details 112
8.3 Results and Discussion 113
8.3.1 Impedance Response 113
8.3.2 Equivalent Circuit 116
8.3.3 Conductivity and Activation Energy 117
8.3.4 Dielectric Relaxation and Transition 120
8.4 Summary 124
Chapter 9 Conclusions and Recommendations 126
9.1 Conclusions 126
9.2 Recommendations for Further Research 127
Author's Publications 128
Bibliography 130

ATTENTION: The Singapore Copyright Act applies to the use of this document. Nanyang Technological University Library

List of Figures

Figure 2.1 The six groups of existing models proposed to explain the luminescence of PS. (a) Crystalline Si covered by a layer of hydrogenated amorphous Si, where radiative recombination occurs. (b) A hydride passivated Si surface with mono-, di- and tri-hydride terminations. Radiative recombinations occur at the Si-H bonds. (c) Partially oxidized Si containing defects proposed as radiative centers. (d) Siloxene molecule proposed to exist on the large inner PS surface and act as luminescence center. (e) Si dot with surface states that localize carriers and holes separately (upper part) or together (lower part, radiative recombination). (f) Section of an undulating crystalline quantum wire. A surface defect rends an undulation non-radiative, while an exciton localized in the neighboring undulation recombines radiatively. (from Ref. 38) 8

Figure 2.2 Illustration of the *BOLS* correlation mechanism which states that the bond length reduces with the reduction of the atomic $CN(z_i)$; the bond energy of the shortened bond will rise. Large open circles and the squares are data after Goldschmidt[68] and Feibelman[73]. (from Ref. 71)... 17

Figure 2.3 Evolution of the energy level of an isolated atom to the band of a solid. The work function ϕ, band gap E_G, core-level shift ΔE_v, and bandwidth E_B are indicated. The number of allowed sublevels in a certain band equals the number of atoms of the solid. (from Ref. 36).. 19

Figure 2.4 Schematic illustration of the models of (a) the quantum well developed from the convention for a single atom and (b) the surface bond contraction. Model (b) adds the effect of surface bond contraction to the crystal field of an extended

ATTENTION: The Singapore Copyright Act applies to the use of this document. Nanyang Technological University Library

solid without involving the terms of e-h Coulomb, correlation interaction and any other assumption. The spontaneous bond contraction at the surface lowers the wells of potential energy near the surface while the periodic muffin-tin potential trapping wells remain inside the solid. (from Ref. 36).. 20

Figure 2.5 Mechanisms for E_{PA} and E_{PL} of a nano-semiconductor, involving crystal binding (E_G) and e-p coupling (W). Insert shows the Stokes shift from E_{PA} to E_{PL}. Electron is excited by absorbing a photon with energy E_G+W from the ground minimum to the excited state and then undergoes a thermalization to the excited minimum, and then transmits to the ground emitting a photon with energy E_G–W. (from Ref. 51) 25

Figure 2.6 Comparison of predictions with observations on the D dependence of the E_{PL} of PS. Theoretical results: Data-1,[91] Data-2,[92] Data-3,[90] Data-4,[93] Data-5,[94] Data-6,[95] Data-7,[96] and Data-8.[97] Measurements: Data-9[98] and Data-10[69]. (from Ref. 74) 27

Figure 2.7 Comparison between predictions (solid line) and observations on D dependence of the E_{PA} of PS with Data-1,[99] Data-2,[65] Data-3,[100] and Data-4[98]. (from Ref. [101]) 27

Figure 2.8 Generation and blue-shift of the LFR spectra where the solid, dotted and dashed lines are the corresponding results of the least-squares fitting. The Si-a (A_1 mode), Si-b (T_2 mode), and Si-c (E mode) are calculated from the lattice-dynamic matrix by using a microscopic valence force field model;[130] The Si-d and Si-e are the experimental results.[121] (from Ref. 133) 36

Figure 3.1 Cross-sectional view of a lateral anodization cell. 40

ATTENTION: The Singapore Copyright Act applies to the use of this document. Nanyang Technological University Library

Figure 3.2 Silicon dissolution scheme proposed by Lehmann and Gösele. (from Ref. 15) 42

Figure 3.3 XRD spectra of PS and c-Si recorded at a glancing angle of 0.5º which exhibit a peak at 2θ ≈ 55.9º correlating to (311) planes. 47

Figure 3.4 Three-dimensional AFM image of PS surface (R_{rms}=1.5 nm) 48

Figure 3.5 A schematic diagram of the PECVD system 49

Figure 3.6 Schematic diagram of the FCVA deposition system 51

Figure 3.7 $(\alpha h\nu)^{1/2}$ vs. $h\nu$ plot for PS sample. α is the absorption coefficient and $h\nu$ is the photon energy. The square root of $\alpha\hbar\nu$ is a linear function of photon energy, as expected for an indirect band gap semiconductor.[169] The figure shows the resolution of the absorption spectrum into separate contributions (Urbach's tail and defect aborption).[170] The E_{PA} value is obtained by linear extrapolation to zero absorption. 53

Figure 3.8 Schematic diagram of the dielectric measurement. 54

Figure 4.1 RT PL spectra of PS samples. (from Ref. 101) 55

Figure 4.2 The FTIR spectra of PS samples with different particle sizes 57

Figure 4.3 Room temperature (a) reflection spectra, and (b) absorption spectra of PS samples with different particle sizes, from which the E_{PA} is obtained with the Tauc plot fitting. (from Ref. 101) 58

Figure 4.4 Comparison between predictions (solid line, Equation 2.11) and measurements on the size dependence of the E_G measured using STS[183] and optical method, Data –1[100] ($E_G = E_{PA} - W$), Data –2 (current work, $E_G = (E_{PL} + E_{PA})/2$). (from Ref. 101) 60

ATTENTION: The Singapore Copyright Act applies to the use of this document. Nanyang Technological University Library

Figure 4.5 XPS profiles showing the size dependence of the 2*p* level shift of nanosolid Si. (from Ref. 184) 61

Figure 4.6 (a) Least-root-mean-square linearization of the energy shift gives $E_{2p}(D)$ = 99.06 + 4.52/*D* ± 0.04. The slope is used to derive the atomic trapping and crystal binding of the bulk solid; the intercept is used to calibrate the equipment due to the surface electrostatic charge effect. Panel (b) shows the agreement between prediction (solid line) and the measured size dependence of the Si-2*p* core level shift, where *K* = *D*/2*d*. The calculation is based on Equation 2.16 using the parameters given in Table 4.4. (from Ref. 184).. 62

Figure 4.7 Size dependent Cole–Cole plots of PS. The dots represent the data measured by the *RCL* meter at RT and the lines correspond to simulation using the *RC* parallel circuit model (inset) for typical dielectric materials. 64

Figure 4.8 Cross section view of PS sample. 66

Figure 4.9 Comparison of the predictions on the size–dependent dielectric constants of silicon nanosolids with the sophisticated calculation and measurement results. Calculated Data–1, 2, 3 are after Ref. 191 . Calculated Data–4 and 5 are after Ref. 109. Data–6 is the current experimental results. *d* is the bond length of bulk silicon. *K* is the number of atoms arranged along the radius of a spherical dot or a rod. 67

Figure 4.10 Comparison of the predictions with observations on the size-dependent TO shift of the nanosolid silicon. Theoretical results: Si-1 calculated using correlation length model; Si-3 (dot)[192] and Si-4 (rod) calculated using the bulk dispersion relation of phonons;[193] Si-5 calculated from the lattice-dynamic

ATTENTION: The Singapore Copyright Act applies to the use of this document. Nanyang Technological University Library

matrix;[130] Si-7 calculated using phonon confinement model[194] and Si-8 (rod), Si-9 (dot), calculated using bond polarizability model.[120] Measurements: Si-2;[195] Si-6;[196] Si-10 and Si-11.[122] *d* is the bond length of bulk silicon. *K* is the number of atoms arranged along the radius of spherical dot or a rod. (from Ref. 133)........... 68

Figure 5.1 XPS spectra of the fluorinated and as-grown PS samples showing the existence of fluorine in fluorinated samples. Processing conditions are given in Table 5.1. The existence of a little fluorine in the as-grown sample results from HF acid remnants inside voids after preparation. (from Ref. 202) 73

Figure 5.2 Fluorination effect on the FTIR spectra of PS. The absorption peaks at 667 cm^{-1} and 977/940 cm^{-1}correspond to the Si–H deformation mode and the Si–F stretching mode, respectively. With the increase of rf power upon the fluorination of PS, the absorption peak at 667 cm^{-1} decays while the absorption peaks at 977 and 940 cm^{-1} become stronger. (from Ref. 202).. 75

Figure 5.3 Fluorination effect on Si 2*p* XPS spectra of the PS. There is obvious shift from 101.7 eV for sample F as grown to 102.8 eV for sample J highly fluorinated. (from Ref. 202)... 75

Figure 5.4 (a) RT PL spectra, (b) Reflection spectra, and (c) Absorption spectra of the fluorinated and as-grown PS. (from Ref. 202).. 78

Figure 5.5 Comparison of the E_G of the fluorinated PS with the as-grown PS. The rf power is used to control the fluorine contents in the fluorinated samples. (from Ref. 202) 78

ATTENTION: The Singapore Copyright Act applies to the use of this document. Nanyang Technological University Library

Figure 5.6 Size-dependent PL spectra of as-grown (dash line, refer to Figure 4.1) and fluorinated (solid line) p-Si samples. The data of sizes are given in Table 5.2. (from Ref. 210) 81

Figure 5.7 (a) RT reflection spectra of PS samples as-grown (inset, refer to Figure 4.3) and fluorinated; and, (b) RT absorption spectra of PS samples as-grown (inset, refer to Figure 4.3) and fluorinated, from which the PA energies are derived with the Tauc plot method. (from Ref. 210) 82

Figure 5.8 Size-dependent XPS Si-2p profiles of as-grown (dash line, refer to Figure 4.5) and fluorinated (solid line) p-Si samples. (from Ref. 210) 83

Figure 5.9 Comparison of the predicted with the measured PA and PL peak energies and the E_G and E_{2p} shift of clean (m = 4.88) and fluorinated (m = 5.32) PS. The E_{2p} and E_G data for the clean PS are from ref. 184 and 101, respectively. The arrow indicates the fluorination effect which displace the E_G and E_{2p} line up. (from Ref. 210) 84

Figure 5.10 (a) Serial and parallel models[222,223] of PS consisting of void and silicon and (b) Serial-Parallel model assuming PS as a two-phase granulated compound medium with identical air inclusions placed uniformly inside a homogeneous silicon matrix. 88

Figure 5.11 Top view of Serial-Parallel cell structure of (a) unpassivated and (b) surface oxidized PS... 89

Figure 5.12 (a) Relation between the porosity, dielectric constant and oxidation degree of PS. Experimental data: Data-a[224] and Data-b[225] for PS; Data-c,[226] Data-d[227] and Data-e[228] for porous silica. (b) Relation between the porosity, refractive

ATTENTION: The Singapore Copyright Act applies to the use of this document. Nanyang Technological University Library

index and oxidation degree of PS. Experimental data: Data-1,[217] Data-2,[229] Data-3,[230] Data-4,[231] Data-5,[232] Data-6,[218] and Data-7[233] for PS. *F* = 0 and *F* = 1 corresponds to pure PS and pure porous silica. 92

Figure 5.13 Evolution of the refractive index of PS layers with different oxidation degree. Experimental data: Data-8a, Data-8b, Data-8c and Data-8d,[234] Data-9a and Data-9b,[134] Data-10a and Data-10b,[235] Data-11a and Data-11b[221] for PS. The filled and the unfilled symbols denote the measured refractive index of PS before and after oxidation, respectively. *F* = 0 and *F* = 1 corresponds to pure PS and pure porous silica. 93

Figure 6.1 XPS spectra of the as-grown and metal-deposited PS samples showing the existence of different metals (Table 6.1) in metal-deposited samples. 97

Figure 6.2 Effects of surface metal deposition on (a) the RT PL spectra, (b) the absorption and reflection spectra (inset), and (c) XPS Si-2*p* profiles of PS samples. 99

Figure 6.3 XRD spectra of the as-grown and metal-deposited PS samples (Table 6.2) after annealing at 800 ºC. 101

Figure 6.4 Effects of annealing at 800 ºC on (a) the RT PL spectra, (b) the absorption and reflection spectra (inset) and (c) XPS Si-2*p* profiles of as-grown and metal-deposited PS samples. 104

Figure 7.1 Anodization temperature dependence of the RT PL spectra of PS. 108

Figure 7.2 Anodization temperature dependence of the absorption and reflection spectra (inset) of PS samples, which give the PA edge energy. 109

ATTENTION: The Singapore Copyright Act applies to the use of this document. Nanyang Technological University Library

Figure 7.3 Anodization temperature dependence of Si-2*p* profiles of PS measured using XPS at RT. 109

Figure 7.4 Anodization temperature dependence of E_G of PS measured by averaging the PL and PA energies. 110

Figure 8.1 Circuit model for describing the dielectric behavior of PS, where R_B and C_B are the bulk-grain resistance and capacitance, R_G and C_G are the grain-boundary resistance and capacitance, and R_E and C_E are the electrode/film-interface resistance and capacitance, respectively. (from Ref. 187) 113

Figure 8.2 Cole–Cole plots of PS at different temperatures: (a) 298–523K, (b) 573–648 K, (c) 673–723 K, and (d) 748–798 K. The dots represent the data measured by the *RCL* meter at different temperatures and the lines correspond to simulation using the *RC* parallel circuit model (inset) for typical dielectric materials. (from Ref. 187) 116

Figure 8.3 Arrhenius plot of the conductivity of PS with an activation energy transition from 0.07 to 0.79 eV at about 565 K. (from Ref. 187) 118

Figure 8.4 Schematic diagram of the distribution of the density of states showing the conductivity activation energy E_a, the average conduction energy E_{TR}, and the Fermi energy E_F (from Ref. 51). 120

Figure 8.5 (a) Real part ε′ and (b) imaginary part ε″ of the permittivity of PS as a function of the frequency at different temperatures. (from Ref. 187) 122

Figure 8.6 Plot of $B'(T)$ vs $1000/T$ with a transition at about 561 K. (from Ref. 187) 124

ATTENTION: The Singapore Copyright Act applies to the use of this document. Nanyang Technological University Library

List of Tables

Table 4.1 Measured E_{PL} and derived information on particle size D of PS. 56

Table 4.2 E_{PA} and derived information on E_G of PS. 59

Table 4.3 Parameters for the E_G expansion of PS.. 60

Table 4.4 Measured E_{2p} with different particle size D and the derived information on atomic $E_{2p}(1)$ and bulk shift $\Delta E_{2p}(\infty)$ of nanosolid Si. 63

Table 4.5 Summary of the D-dependent $\varepsilon_{nano\text{-}Si}$ derived from the measured E_{PL}, porosity and ε_{eff} of PS.. 65

Table 5.1. Summary of the fluorination process parameters and corresponding results.. 72

Table 5.2 Measured E_{PL}, E_{PA} and E_{2p} of F-passivated PS with particle size D 81

Table 6.1 Summary of the results for PS samples deposited with different metals before annealing... 98

Table 6.2 Summary of the results for PS samples deposited with different metals after annealing... 103

ATTENTION: The Singapore Copyright Act applies to the use of this document. Nanyang Technological University Library

Nomenclature

AFM: Atomic force microscopy

BOLS: Bond–Order–Length–Strength

CN: Coordination number

c-Si: Crystalline Si

e-h: Electron-hole

e-p: Electron-phonon

FCVA: Filtered cathodic vacuum arc

FTIR: Fourier-transform infrared spectroscopy

FWHM: Full width at half maximum

PECVD: Plasma enhanced chemical vapor deposition

PA: Photoabsorption

PL: Photoluminescence

PS: Porous silicon

QC: Quantum confinement

rf: Radio frequency

RT: Room temperature

SEM: Scanning electron microscopy

TO: Transverse optical

XPS: X-ray photoelectron spectroscopy

XRD: X-ray diffraction

D: Nanosolid size

E_G: Band gap

ATTENTION: The Singapore Copyright Act applies to the use of this document. Nanyang Technological University Library

E_{PL}: PL peak energy

E_{PA}: Absorption edge

d: Bond length

E_b: Bond energy

δ_{surf}: The effect of surface relaxation

$\delta_{e\text{-}p}$: The effect of electron-phonon coupling

C_i: Bond contraction coefficient

K: The number of atoms lined along the radius of a spherical dot or the thickness of a thin plate

z: Coordination number

γ_i: Surface-to-volume ratio

m: BOLS Coefficient

$2W$: Stokes shift

E_v: Core-level energy of an isolated atom

p: Porosity

$\varepsilon_{nano\text{-}Si}$: Dielectric constant of nano-Si

ε_{eff}: Effective dielectric constant of PS

χ: Dielectric susceptibility

ω: Raman frequency

ATTENTION: The Singapore Copyright Act applies to the use of this document. Nanyang Technological University Library

Chapter 1 Introduction

1.1 Overview

Porous silicon (PS) is not a new material, but it is only relatively recently that its true microstructure and surprising properties have come under close scrutiny. PS was first made[1] some 40 years ago by the Uhlirs at Bell Labs, USA. During studies of the electropolishing of Si in HF-based solutions they observed that the surfaces often developed “a matte black, brown or red deposit”. The deposits were “tentatively supposed to be a Si suboxide” and for the next decade largely remained an unwanted scientific curiosity. One year after the original work, Fuller and Ditzenberger[2] reported that similar films could develop in HF-HNO_3 solutions without any externally applied electrical bias to the Si. The “anodized” films first received more detailed study by Turner[3] and the chemical “stain” films by Archer[4]. These films were not recognized as being PS, let alone a Si nanostructure, for many years. It was Watanabe and co-workers[5,6] who first reported their porous nature and the ease with which the material could be converted into thick Si oxide films. Pioneering Japanese work[7,8] on utilizing this for dielectric (trench) isolation of active Si devices was followed in the 1970’s. However, it was Imai’s so-called full isolation by porous oxidized Si process[9] developed at NTT Labs, Tokyo, that prompted a significant rise in the perceived potential of the material in the 1980’s. A number of approaches to realizing Si-on-insulator circuitry were subsequently developed.[10,11,12,13] Nevertheless, before 1990, there were less than 200 papers published on PS, spanning a period of 35 years.

ATTENTION: The Singapore Copyright Act applies to the use of this document. Nanyang Technological University Library

There is a dramatic increase of interest in PS after tunable efficient, room temperature (RT) light output from the material [14] generated in 1990. Independently, Lehman and GÖsele[15] reported in 1991 that PS could exhibit an increased E_G compared with bulk Si. This property, as well as the formation mechanism itself, involved quantum size effects. Within a year, not only multicolor (red-green) PL[16] but also efficient forms of visible electroluminescence had been achieved,[17] generating considerable excitement.[18] The origin of the luminescence, however, quickly became a very controversial topics and a plethora of models emerged, each supported by specific observations of the microstructure of the material and the spectroscopic nature of the light emission process.

The current worldwide interest in PS is particularly intriguing for three reasons. Firstly, PS has a silicon structure; and bulk silicon is spectacularly inefficient at emitting light, even at cryogenic temperature. Secondly, the light emitting nanostructure can be “made in a bucket” within minutes, without resort to either the costly lithographic or epitaxial techniques that were at the time, the conventional approaches to realizing exceedingly small structures. Thirdly, silicon is the most technologically important material known to mankind, dominating the microelectronics revolution that influences our daily lives. Light-emitting silicon devices could eventually result in a new generation of silicon chips and extend the functionality of silicon technology from microelectronics into optoelectronics.

ATTENTION: The Singapore Copyright Act applies to the use of this document. Nanyang Technological University Library

1.2 Motivation

The development of PS electronic devices needs to proceed in parallel with the fundamental studies of the correlation between optical, dielectric and structural properties. The possibility of efficient use of PS in optoelectronic devices relies on the full comprehension of the physical phenomena that control its optical and dielectric properties. Given the large and varied body of work on PS, there still remains a basic lack of knowledge regarding the structure and composition of the species actually responsible for the optical and dielectric activity. At least four factors contribute to this uncertainty: (1) Heterogeneity: anodic etching in HF produces material consisting of macroscopic regions of unetched crystalline silicon (c-Si) separating areas of variously sized nanoscale PS structures. The observed luminescence wavelength and efficiency depend on the size distribution of these nanostructures, and the distribution varies with details of the etching conditions and of the starting silicon-wafer properties. (2) Chemical reactivity: the nanostructure surfaces in freshly prepared PS are passivated with H, and these are generally unstable with respect to subsequent exposure to air. The presence or absence of H or O on the surfaces of nanosized silicon structures could in principle affect the optical and dielectric properties of the PS samples. (3) Characteristic sizes: optically active structures smaller than 2 nm are beyond in practice detection limits of standard microscopy and diffraction methods. Accordingly, the smallest dimensions for structures observed and reported with these techniques are ≥ 2 nm. (4) Calculational uncertainties: various theoretical studies correlating band gap (E_G) with silicon size report nanoscale particle or wire dimensions for a given E_G

ATTENTION: The Singapore Copyright Act applies to the use of this document. Nanyang Technological University Library

which vary by more than 100%.[19,20,21,22] Little attention is usually given to the size regime of structures < 2 nm. Because of the above reasons, it is of scientific interests to understand the properties of this material and the factors dominating the property change in order to obtain devices which work in a predictable way.

1.3 Objective

The main objective of this project is to provide

1. Consistent understanding of the physical and chemical effects on the properties of nanomaterials.
2. New freedom to gain certain kinds of information that is beyond traditional approaches to explore the nanoproperties.
3. Controllable and predictable work for the guidelines to design and fabricate the nanodevices.

1.4 Major Achievement

The contributions to the work are as follows:

1. PS samples are prepared by electrochemical etching method; and their size is controlled by changing the anodization current density.
2. The surface of PS is passivated with F and metalized by Cu, Al, and Ti.
3. The size effects on the optical and dielectric properties of PS are studied; a newly proposed surface bond relaxation mechanism is used to explain the size-induced variation of various properties consistently.

ATTENTION: The Singapore Copyright Act applies to the use of this document. Nanyang Technological University Library

4. The surface passivation/metalization effects on the optical and dielectric properties of PS are investigated and a corresponding explanation is provided.
5. The temperature effects on the dielectric performance of PS are examined and a corresponding explanation is provided.
6. Single energy level of the 2*p* electrons of an isolated Si atom, vibration frequency of a Si–Si dimer bond, and their shift upon bulk and nanosolid formation are quantified by matching predictions to the observed size and shape dependence of the XPS and Raman data. This method is beyond the scope of currently available approaches.

1.5 Organization of the Thesis

The thesis will start, in Chapter 1, with a brief overview on PS studies and the reason for current worldwide interests in this topic. Chapter 2 will describe previous various models used to explain the optical properties of PS and their deficiency, and introduce a more reasonable "Bond–Order–Length–Strength" (*BOLS*) correlation mechanism proposed by Dr Sun to explain the size-induced variations of properties. Chapter 3 will describe the sample preparation methods including size control and surface passivation/metalization. In Chapter 4, observations on the E_G expansion, Si-2*p* level blue shift, the Raman red shift, and the dielectric suppression of a number of typical samples are systematically analyzed based on the core idea of the *BOLS* correlation for deep insight and generalized information. Single energy level of the 2*p* electrons of an isolated Si

ATTENTION: The Singapore Copyright Act applies to the use of this document. Nanyang Technological University Library

atom and vibration frequency of a Si–Si dimer bond and their shift upon bulk and nanosolid formation have been quantified. Chapter 5 will report the surface passivation effects on the optical and dielectric properties. The effect of surface passivation has been distinguished from the effect of size on the photonic and electronic behavior of PS based on *BOLS* correlation. Moreover, a Serial-Parallel capacitance structural model has been proposed to determine the extent of surface oxidation by measuring porosity dependent dielectrics of oxygenated PS. Chapters 6 and 7 will examine the effects of surface metalization and anodization temperature on optical and dielectric properties, respectively. Chapter 8 will introduce dielectric impedance variations with frequency and temperature which reveal three semicircles in a Cole–Cole plot and an activation energy transition at high temperature. The thesis will end (Chapter 9) with a summary of the main conclusions and recommendations for further research.

ATTENTION: The Singapore Copyright Act applies to the use of this document. Nanyang Technological University Library

Chapter 2 Theory Consideration

2.1 Introduction

One of the recent remarkable trends in semiconductor physics is the interaction between physics, materials sciences and technology. Many researchers are producing complex structures and composites that have unique physical properties.[23] Nanometer-sized semiconductor crystallites are a subset of the notable examples of complex structures.[24] Nanosolids have large surface-to-volume ratios, and surface effects take on significance that is normally inconsequential for bulk materials. The small volume can confine free carriers, allowing observation of quantum behavior. While of immense intrinsic interest, the study of nanosolids is also propelled by technological promise. Various physical properties such as mechanical strength,[25,26] plasticity,[27] thermal stability,[28] sintering ability,[29,30] diffusion,[31] and electronic structures[32,33] as well as the chemical reactivity[34,35] are dependent upon particle size. There have been numerous studies on the relationship between the size of nanosolids and their properties. Unfortunately, consistent insight into the size and shape dependency of the nanostructured solid is still lacking. As a result, further exploration is necessary. In this chapter, a new mechanism-*BOLS* correlation [36,37] is introduced to explain size-dependent properties of PS.

ATTENTION: The Singapore Copyright Act applies to the use of this document. Nanyang Technological University Library

2.2 Existing Models

Quantum confinement (QC) of carriers in Si wires was the first model proposed to explain PS luminescence.[14] Afterwards, many other alternative explanations have been proposed.[38] Figure 2.1 illustrates the main six models. Except for the QC model, all the others assume an extrinsic origin for the luminescence.

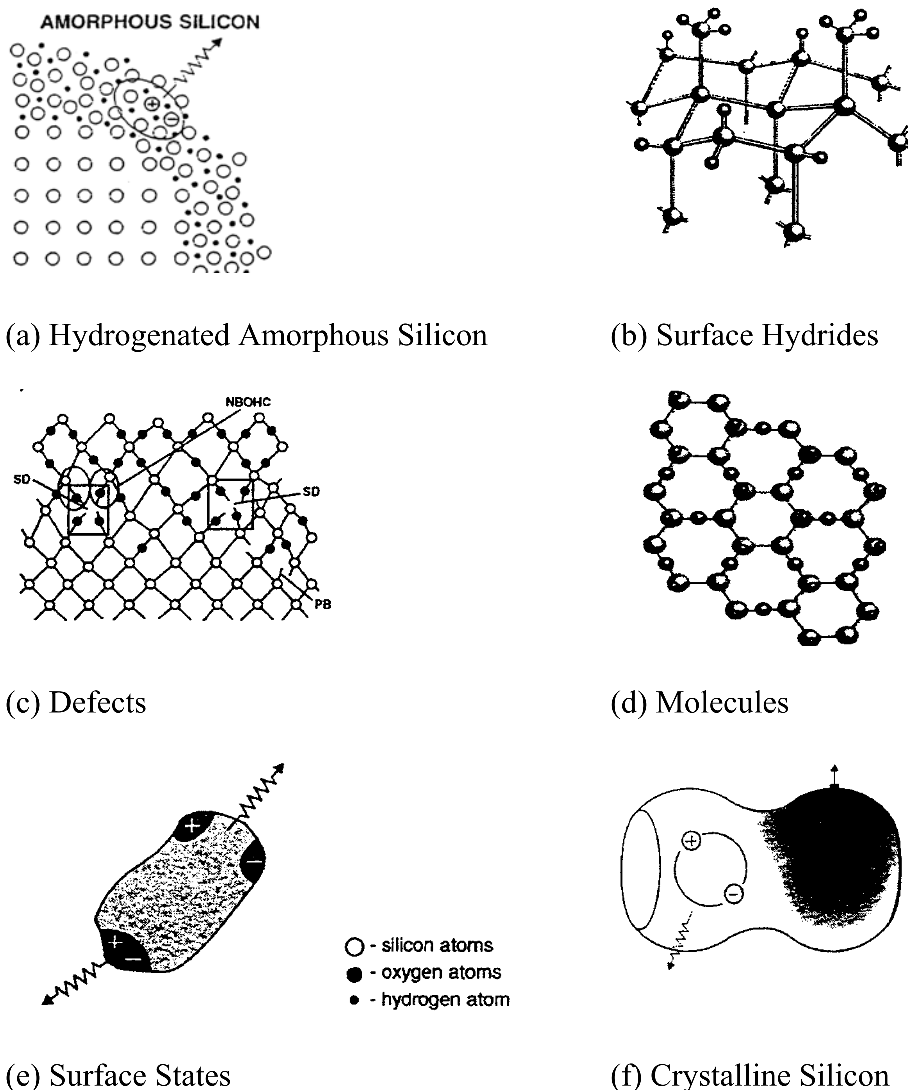

(a) Hydrogenated Amorphous Silicon (b) Surface Hydrides

(c) Defects (d) Molecules

(e) Surface States (f) Crystalline Silicon

Figure 2.1 The six groups of existing models proposed to explain the luminescence of PS. (a) Crystalline Si covered by a layer of hydrogenated amorphous Si, where radiative recombination occurs. (b) A hydride passivated Si surface with mono-, di- and tri-hydride terminations. Radiative recombinations occur at the Si-H bonds. (c) Partially oxidized Si

ATTENTION: The Singapore Copyright Act applies to the use of this document. Nanyang Technological University Library

containing defects proposed as radiative centers. (d) Siloxene molecule proposed to exist on the large inner PS surface and act as luminescence center. (e) Si dot with surface states that localize carriers and holes separately (upper part) or together (lower part, radiative recombination). (f) Section of an undulating crystalline quantum wire. A surface defect rends an undulation non-radiative, while an exciton localized in the neighboring undulation recombines radiatively. (from Ref. 38)

A. Hydrogenated amorphous silicon model (Figure 2.1a)

It has been proposed that PS luminescence is due to a hydrogenated amorphous phase (*a*-Si:H) which is formed during anodization.[39,40] *a*-Si:H possesses a PL band[41] in the visible range, and the tunability of the PL from PS is suggested to be explained with alloying effects and with the variation of hydrogen and oxygen percentages. In addition, the time resolved measurements are thought to indicate that the disorder plays a key role in the recombination dynamics.[42]

Against this model, recent transmission electron microscopy (TEM) studies where sample damage has been minimized show that there is little amorphous Si in PS.[38] Moreover, the *a*-Si:H PL band is strongly quenched from cryogenic to RT, while the PL intensity of PS is enhanced as the temperature is raised.[43] Finally, the number, energies and relative strengths of the phonon replicas observed in resonantly excited PL spectra convincingly show that the luminescent material in PS has both electronic and vibrational band structure of crystalline Si (c-Si), and consequently cannot be amorphous in nature.[44]

B. Surface hydrides model (Figure 2.1b)

Since the PS luminescence decreases dramatically if the hydrogen on the surface is thermally desorbed, and the PL intensity can be recovered with

ATTENTION: The Singapore Copyright Act applies to the use of this document. Nanyang Technological University Library

immersion in HF, which restores the hydrogen coverage,[45,46] SiH_x surface species were suggested to be responsible for the luminescence in PS.[47]

Against this model there are many evidences. Fourier-Transform Infrared Spectral (FTIR) studies have demonstrated that luminescence is totally quenched when the majority of hydrogen is still on the PS surface,[48] and the luminescence loss is probably related to the formation of dangling bonds and efficient non-radiative decay channel. Another evidence comes from the simple fact that when the hydride coverage is replaced by a good quality oxide layer, the PL process is still efficient.[49,50] Furthermore, no correlation of the PL intensity with hydride coverage is observed for PS samples with different morphologies; macroporous Si can have a large hydride passivated internal surface and yet exhibits no visible PL. It is, therefore, clear that hydride passivated PS is only one of a number of possible luminescent forms of this material and hydrogen passivation can improve the quantum efficiency but has nothing to do with the E_G.[51]

C. Defect models (Figure 2.1c)

In defect models the luminescence originates from carriers localized at extrinsic centers, i.e. defects in the silicon or silicon oxide that covers the surface.[52,53]

However, luminescent nanocrystalline Si can be created in many different ways, and passivated either with hydrogen or with oxygen, and it is then very unlikely that the same impurity or defect is always present. In any case the defects in the silicon oxide are ruled out, because SiO_2 is not present in fresh PS.[54] Also the

ATTENTION: The Singapore Copyright Act applies to the use of this document. Nanyang Technological University Library

tunability of the PL band is difficult to justify, because the emission from defects is expected to be almost insensitive to the size of the Si structure they exist in.

D. Siloxene model (Figure 2.1d)

Siloxene, an Si:H:O based polymer, supposedly created during PS anodization, was proposed as the origin of PS luminescence.[55] This model is supported by the fact that the optical properties of siloxene are somehow similar to those of PS.[56] Siloxene possesses a visible-red PL band; and its IR spectrum closely relates to that of aged PS.

Many experiments have evidenced the deficiency of this model. It is now well demonstrated that freshly etched PS has no detectable oxygen content. PS can still be luminescent at temperatures above 800°C, while siloxene or other related molecules are totally decomposed at such a high temperature. In addition to the spectroscopic evidences which show a crystalline nature of the emission, synchrotron radiation measurements show that SiO groups have no role in the emission process.[57]

E. Surface states model (Figure 2.1e)

The enormous inner surface of PS has led to proposal that it is involved in the luminescence process.[58] The excitons, quantum confined in Si nanocrystals, should know the existence of the surface and of its reconstruction. For this reason, the model has also been called smart quantum well model.[58] In this model, absorption occurs in quantum-confined structures, but radiative recombination involves localized surface states. Either the electron, or the hole, or both or none can be

ATTENTION: The Singapore Copyright Act applies to the use of this document. Nanyang Technological University Library

localized. Hence, a hierarchy of transitions is possible, which explains the various emission bands of PS. The energy difference between absorption and emission peaks is well explained in this model, because photoexcited carriers relax into surface states. The dependence of the luminescence from external factors or from the variation of the PS chemistry is naturally accounted for by surface states change.

Resonantly excited PL results are against the attribution of PL process to surface states,[38] showing that PL arises from exciton coupling with momentum-conserving phonons. This means that the exciton wavefunction is extended over many Si atoms and not strongly localized, as it should be in the case of deep surface states. Furthermore, the values of the exchange splitting energy extracted from temperature dependent lifetime measurements[38] also suggest that carriers are not localized on atomic scale, but in the whole volume of the Si nanocrystals, and that luminescence does not originate from localized states in the gap, but from extended states. Finally, the observed polarization of the PL[38] and the fact that this polarization extrapolates linearly to the E_G of bulk Si, rather than tailing off to energies below it, implies that luminescence does not originate from localized states in the gap, but rather from bulk-like confined states.

F. Quantum confinement model (Figure 2.1f)

As mentioned previously, QC in c-Si was the first model proposed to explain the efficient PL of PS.[14] In this model, electrons in the conduction band and holes in valence band are confined spatially by the potential barrier of the surface, or

ATTENTION: The Singapore Copyright Act applies to the use of this document. Nanyang Technological University Library

trapped by a mono-center of potential well of the quantum box. Because of the confinement of both electrons and holes, the optical transition from the valence to the conduction band increases in energy, which results in an enlargement of the E_G, in a relaxation of the momentum-conversing rule, and in a size dependence of PL energy which naturally explains the efficient luminescence, the up-shift and the tunability of PL band in PS. The E_G up-shift is clearly visible in absorption spectra; and the luminescence blue-shift after further chemical dissolution in HF is easily explained by further reduction of nanocrystals dimensions. The confinement effect on the E_G of a nanosolid of dimension D is expressed as[59,60]

$$E_G(D) = E_G(\infty) + \frac{2h^2\pi^2}{\mu D^2} - \frac{3.576e^2}{\varepsilon_r D} + 0.284E_R \qquad (2.1)$$

Where μ is the effective mass of an electron-hole (e-h) pair which meets $1/\mu = 1/m_h^* + 1/m_e^*$ and E_R is the Rydberg (spatial correlation) energy for the bulk semiconductor:

$$E_R = \frac{\mu e^4}{2\varepsilon_r^2\varepsilon_0^2h^2} = 13.56(\frac{\mu}{\varepsilon_r^2 m_e}) \qquad (2.2)$$

The effective dielectric constant ε_r and the effective mass μ describe the effect of the homogeneous medium in the quantum box.

Later development of the QC theory shows that luminescence blue-shift follows a $\Delta E_G(D)/E_G(\infty) \propto D^{-n}$ law (n=2[61], 1.16[62], 1.3[63], 1.37[64]). However, an effective mass approximation[65] confirmed that the D^{-n} dependence suits only for crystallites larger than several nanometers. Not surprisingly, serious convergence problems arise when the solid is very small.

ATTENTION: The Singapore Copyright Act applies to the use of this document. Nanyang Technological University Library

G. Other Model

Most recently, Glinka *et al.*[66] proposed a free-exciton collision model and suggested that, during the measurement of the PL of a nanosolid, the excitation laser heats the free excitons that then collide with the boundaries of the nanometer-sized fragments. The laser heating the free-excitons up to a temperature in excess of the activation energy required for the self-trapping, gives rise to the extremely hot self-trapping excitons (STE). Because the resulting temperature of the STE is much higher than the lattice temperature, the cooling of STE is dominated by the emission of lattice phonons. However, if the STE temperature comes into equilibrium with the lattice temperature, the absorption of lattice phonons becomes possible. As a result, the blue shift of the STE-PL band is suggested to originate from the activation of hot-phonon-assisted electronic transitions. The blue shift of the STE-PL band depends on the temperature of laser-heated free excitons that in turn is determined by the size of nanometer-sized (silica example considered only) fragments. This happens because the temperature (kinetic energy) of the laser-heated free exciton increases with the number of collisions with the boundary of confined regions, which tends to be higher with decreasing size of silica fragments in nanoscale materials. The energy gained from laser heating of the exiton increase with decreasing nanoparticle diameters in an $\exp(1/D)$ way.

Based on the analysis, Glinka *et al.*[66] suggested that the size-dependent PL peak shift of a nanosolid in general does not need to be always related to the QC effect. As a result, a new approach for the size-induced luminescence blue shit and the E_G expansion of PS at lower end of size limit should be developed. In the

ATTENTION: The Singapore Copyright Act applies to the use of this document. Nanyang Technological University Library

following section, we will present a general yet simple *BOLS* correlation mechanism developed recently,[36] attempting to unify as far as possible the variations caused by changing the shape-and-size of the physical system.

2.3 "Bond-Order-Length-Strength" Correlation

With reduced dimensions of solids or devices, quantum and interface effects become dominant. The striking significance of nanometric materials is that the conventionally detectable quantities are no longer constant but they are adjustable by simply controlling the shape and size of the solid. The continuous change of the properties has been leading to a revolution in materials science and device technology. It is possible to tune the physical performance of a device by adjusting the sizes of particles that compose the medium of the device. However, from a fundamental point of view, the origins and the general trend of the property variations are yet to be understood, although there are often numerous models describing a specific phenomenon. As will be shown in the following sections that the coordination number (*CN*) imperfection induced bond contraction at the surface and the rise in the portion of surface atoms may unify the enormous variations of nanosolid properties.

2.3.1 Surface Bond Contraction

The termination of the lattice periodicity in the surface normal has resulted in. the *CN* imperfection of surface atoms, which cause the remaining bonds of the low-CN atoms to relax.[67,68] As the relaxation (both contraction and expansion) is a spontaneous process, the binding energy of the relaxed bond will be lowered (rise

ATTENTION: The Singapore Copyright Act applies to the use of this document. Nanyang Technological University Library

in the absolute value) to minimize the system energy. Such a consequence leads to a *BOLS* correlation mechanism which indicates that: (i) Atomic radius of a surface atom relaxes spontaneously because of the reduced atomic *CN* at the surface. (ii) The bond energy of the relaxed bond increases because of the spontaneous relaxation. (iii) The bond energy rise increases the energy density in the relaxed region because the number of bonds does not change between any two neighboring circumferential atomic layers with relaxation. (iv) The density rise of binding energy in the relaxed region contributes to the Hamiltonian of the solid that determines the entire band structure of a nanosolid including the E_G, core-level shift, bandwidth and the band tails through modifying the crystal field.[36]

For a spherical dot with diameter D or a thin plate with thickness D, where are $2K$ atoms arranged along D. The ith atomic shell with thickness of d_i can be filled with N_i atoms of diameter d_i (bond length). It is necessary to introduce a contraction coefficient $c_i < 1$, and $d_i = c_i d$, where d are the bond lengths of atoms in the bulk. Correspondingly, the binding energy for a single bond grows to $E_{b,i}(d_i) = c_i^{-m} E_b(d)$ because the process of bond contraction is spontaneous. $E_{b,i}(d_i)$ and $E_b(d)$ are the corresponding bond energy at equilibrium atomic separation. c_i^{-m} describes the energy change with the reduced bond length. The *BOLS* coefficient m is an adjustable parameter describing the nature of the bond. Progress[36,69,70,71] so far reveals that for elemental solid, m = 1; for compounds and alloys, m = 4. As illustrated in Figure 2.2, the *BOLS* correlation can be formulated as:

$$\begin{cases} d_i = c_i d \\ E_{b,i}(d_i) = c_i^{-m} E_b(d) \\ c_i(z_i) = 2/\{1+\exp[(12-z_i)/(8z_i)]\} \end{cases} \quad (2.3)$$

ATTENTION: The Singapore Copyright Act applies to the use of this document. Nanyang Technological University Library

The z_i is the effective *CN* of an atom in the *i*th atomic layer. Normally, for the outermost three atomic layers of a flat platem, $z_1 = 4$, $z_2 = 6$ and $z_3 = 12$. For a spherical dot, $z_1 = 4(1–0.75/K)$[72] and $K = D/2d$. The bond contraction coefficient $c_i(z_i)$ is formulated based on Goldschmidt's premise[68] and Feibelman's finding[73] on the dimer bond contraction of *Ti*, *Zr*, *Mo*, and *V*. According to Goldschmidt, if the *CN* reduces from 12 to 8, 6, or 4, the corresponding ionic radius will shrink by 3%, 4% and 12%, respectively. Except for some II-a (*Be*, *Mg*(0001) surface) and II-b (*Zn*, *Cd*, *Hg* dimer bond) elements that are reported to expand all the elemental dimer bonds contract by even as high as 30%–40% for *Ti*, *Zr*, *V* and *Mo* example. It should be emphasized that the *BOLS* premise involves no assumptions or freely adjustable parameters or even the particular form of the interatomic potential.

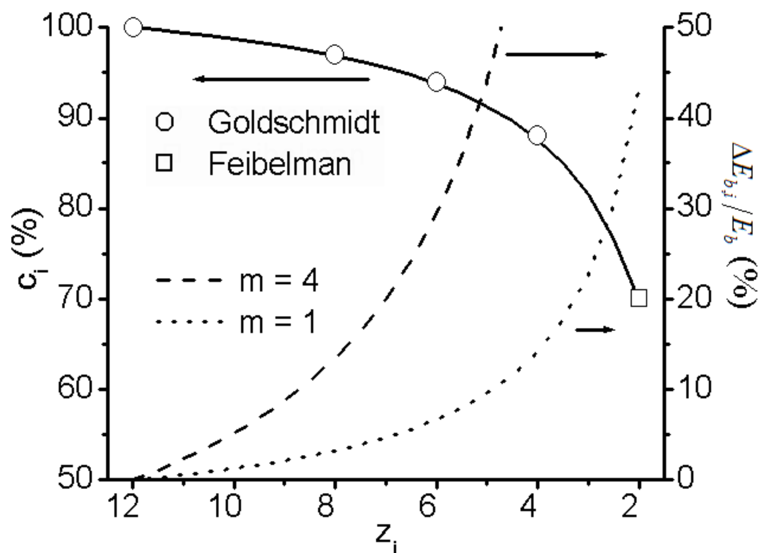

Figure 2.2 Illustration of the *BOLS* correlation mechanism which states that the bond length reduces with the reduction of the atomic $CN(z_i)$; the bond energy of the shortened bond will rise. Large open circles and the squares are data after Goldschmidt[68] and Feibelman[73]. (from Ref. 74)

ATTENTION: The Singapore Copyright Act applies to the use of this document. Nanyang Technological University Library

There is sufficient evidence supporting the *BOLS* mechanism. For instance, the first interlayer spacing of diamond (111) has been reported to contract by 30%.[75] A contraction by 4% – 12% of the *O-Cu* bond has been found to form one of the four essential stages in the *O-Cu* (001) surface bonding kinetics.[76] A 12%–14% contraction of the *N-Ti/Cr* bond has been confirmed to enhance the surface stress by up to 100%.[69] Most encouragingly, a recent density functional theory calculation[77] reveals that for *Au*, *Cu*, *Pt*, *Pd*, *Ni* and *Ag* single atomic chains, the binding energy per bond is (–3 ~ –1 eV) 2 ~ 3 times larger in the chains than the single bond energy (–1~ –0.4 eV) of the bulk fcc structures and the equilibrium atomic separation contracts by 10 %(for *Cu* and *Ag*) or ~15% (for *Pt*). These findings concur with the *BOLS* premise though the extents of relaxation and energy rise differ slightly. Efforts made so far have shown consistently that the bond contraction at a surface dominates the size-and-shape dependency of nanometric materials in many aspects such as the mean lattice contraction,[78] blue-shift in PL,[70,79]and dielectric suppression[71] of semiconductive nanosolids as well as the transition behavior of ferro- and pyro-electrics of *PbZrTi* oxides.[80,81]

2.3.2 Hamiltonian and Band Structure

Figure 2.3 illustrates the evolution of the energy levels of a single atom to the energy bands of a bulk solid containing *N* atoms. Electrons of a single atom confined by the intraatomic trapping potential, $V_{atom} = -\infty$, move around the central ion core in a standing-wave form inside the potential well. The corresponding eigenfunctions and eigenenergies are given as follows:

ATTENTION: The Singapore Copyright Act applies to the use of this document. Nanyang Technological University Library

$$\phi_v(r) \propto \sin^2\left(\frac{2l\pi r}{d}\right) \text{ and } E_v(l) = \frac{2(l\pi\hbar)^2}{m_e d}, l = 1, 2, 3, \ldots \quad (2.4)$$

where $d = 2r$ is the dimension of the potential well and m_e is the mass of an electron. Different l values correspond to the different energy levels and the separation between the closest two levels depends on $(l + 1)^2 - l^2$.

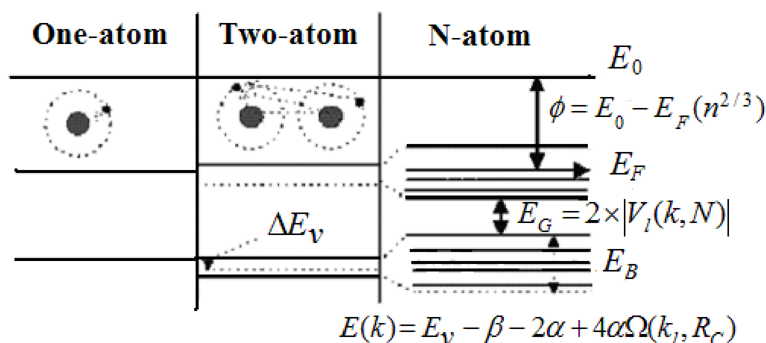

Figure 2.3 Evolution of the energy level of an isolated atom to the band of a solid. The work function ϕ, band gap E_G, core-level shift ΔE_v, and bandwidth E_B are indicated. The number of allowed sublevels in a certain band equals the number of atoms of the solid. (from Ref. 36)

When a system contains two atoms, a single energy level splits into two sublevels and the separation between the two sublevels is determined by the interatomic binding potential. Increasing the number of atoms to N, the single energy level will expand into a band in which there are N sublevels. It is known that the number of atoms (N) of a solid determines the number of sublevels in a particular energy band. What distinguishes a nanosolid from a bulk solid is that for the former N is accountable, while for the latter N is too large. Therefore, classical band theories are valid for a single nanometric solid that contains at least 10^2 atoms. As detected with XPS, the density of states of a core band for a nanosolid exhibits band-like features rather than the discrete energy levels of a single atom. If N is

ATTENTION: The Singapore Copyright Act applies to the use of this document. Nanyang Technological University Library

sufficiently small, the separation between sublevels is resolvable, which may form the foundations of the quantized conductance of nanosolids.

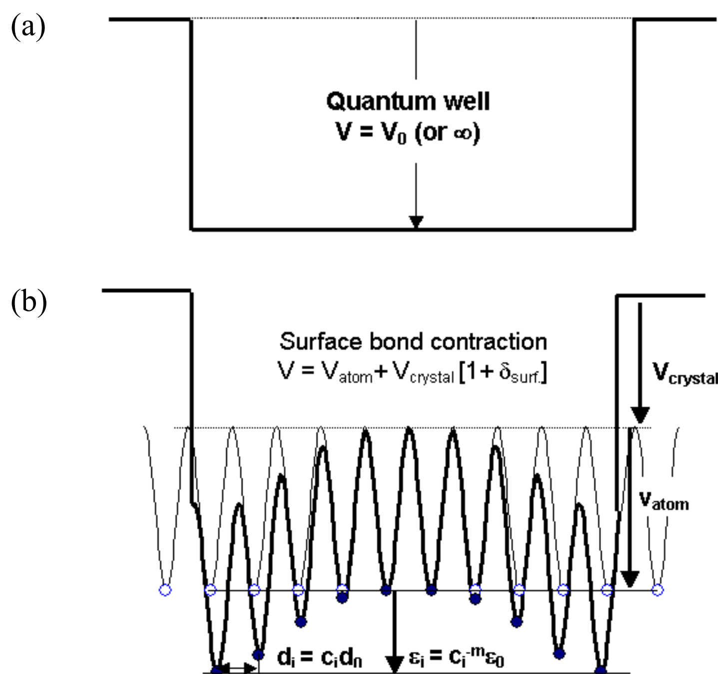

Figure 2.4 Schematic illustration of the models of (a) the quantum well developed from the convention for a single atom and (b) the surface bond contraction. Model (b) adds the effect of surface bond contraction to the crystal field of an extended solid without involving the terms of e-h Coulomb, correlation interaction and any other assumption. The spontaneous bond contraction at the surface lowers the wells of potential energy near the surface while the periodic muffin-tin potential trapping wells remain inside the solid. (from Ref. 36)

The potential well of a single atom and a nanosolid that contains multiple trapping centers is illustrated in Figure 2.4. The trapping centers are lowered near the edge of the solid due to the bond relaxation. Considering the contribution of the outermost atomic layers, the Hamiltonian of a nanosolid is given as:[36]

ATTENTION: The Singapore Copyright Act applies to the use of this document. Nanyang Technological University Library

$$\begin{aligned}
\hat{H}(r) &= \hat{H}_{atom}(r) + \hat{H}_{crystal}(r) \\
\hat{H}_{atom}(r) &= -\frac{\hbar^2\nabla^2}{2\mu} + V_{atom}(r) \\
\hat{H}_{crystal}(r) &= V_{crystal}(r+R_C)[1+\delta_{Surf}]
\end{aligned} \tag{2.5}$$

$V_{atom}(r)$, the potential of intraatomic trapping, is responsible for the discrete energy levels of an isolated atom and confines electrons moving inside the potential in the form of standing wave. $V_{crystal}(r+R_C)$ is the crystal field of an extended solid which sums the interatomic binding potential over the solid. R_C is the lattice constant. According to the nearly-free-electron approximation, the gap E_G between the conduction band and the valence band originates from the crystal field and the width of the gap depends on the integration of the crystal field in combination with the Bloch wave of the nearly free electron, $\phi(k_l, r)$:

$$E_G = 2|V_l(k_l)| \text{ and } V_l(k_l) = \langle \phi(k_l, r)|V(r+R_C)|\phi(k_l, r)\rangle \tag{2.6}$$

where k_l is the wavevector and $k_l = 2l\pi/R_C$. There E_G is simply the first Fourier coefficient of the crystal field.

The energy dispersion in a core band follows the relation

$$\begin{aligned}
E(k) &= E_v - \beta - 2\alpha + 4\alpha\Omega(k_l, R_C) \\
\Omega(k_l, R_C) &= \sum_z \sin^2\left(\frac{k_l R}{2}\right)
\end{aligned} \tag{2.7}$$

where $E_v = \langle \phi_v(r)|\hat{H}_{atom}(r)|\phi_v(r)\rangle$ is the energy of the core electron of an isolated atom, $\beta = -\langle \phi_v(r)|V_{crystal}(r)|\phi_v(r)\rangle$ is the crystal field effect on the core electrons of the specified coordinate r, and $\alpha = -\langle \phi_v(r-R_C)|V_{crystal}(r-R_C)|\phi_v(r-R_C)\rangle$ is the

ATTENTION: The Singapore Copyright Act applies to the use of this document. Nanyang Technological University Library

crystal field effect on the coordinate neighboring electrons. The sum is over all contributing coordinates (z) surrounding a particular atom in the solid.

Equations (2.6) and (2.7) indicate that the band gap E_G, the core-level shift $\Delta E_v = \beta + 2\alpha$, and the bandwidth E_B are all functions of the crystal field. Without the crystal field, neither the band gap nor the core-level shift would be possible. Without the interatomic binding, no solid or even liquid would form.

It is also clear that any variation of the crystal field will cause changes of the corresponding derivatives:

$$\frac{\Delta E_G(D)}{E_G(\infty)} = \frac{\Delta E_v(D) - \Delta E_v(\infty)}{\Delta E_v(\infty)} \propto \frac{\Delta\alpha}{\alpha} = \frac{\Delta\beta}{\beta} \equiv \frac{\Delta V_{crystal}(r)}{V_{crystal}(r)} \tag{2.8}$$

A physically detectable quantity for a nanosolid can be expressed as $P(D)$, and as $P(\infty) = Np_0$ for a bulk solid. The relation between $P(D)$ and $P(\infty)$ and the relative change of P can be expressed in a shell structure:

$$\begin{cases} P(D) = Np_0 + N_S(p_s - p_0) \\ \dfrac{P(D) - P(\infty)}{P(\infty)} = \sum_{i\le 3} \gamma_i \left[\dfrac{p_i}{p_0} - 1\right] \end{cases} \tag{2.9}$$

where p_0 and p_S correspond to the P value per atomic volume inside the bulk and in the surface region, respectively, N and $N_S = \Sigma N_i$ are the number of atoms in the bulk and the surface atomic shells, respectively. γ_i is the volume portion of the ith atomic layer in the entire solid of different dimensionality (τ = 1, 2, and 3 corresponds to a plate, a rod and a spherical dot, respectively), which is given as:

$$\gamma_i = \frac{N_i}{N} = \frac{V_i}{V} = \frac{D^{\tau}_{out,i} - D^{\tau}_{in,i}}{D^{\tau}} \cong \frac{\tau c_i}{K} \qquad (D = 2Kd) \tag{2.10}$$

ATTENTION: The Singapore Copyright Act applies to the use of this document. Nanyang Technological University Library

$D_{out,i}$ and $D_{in,i}$ correspond to the outer and inner diameter of the *i*th atomic layer with d_i (= $D_{out,i} - D_{in,i} = c_i d$) thickness. It is important to note that the $\sum_{i\le 3}\gamma_i$ drops in a D^{-1} fashion from unity to infinitely small when the solid dimension grows from atomic level to macroscopic scale. The index i is counted up to three from the outermost atomic layer to the center of the solid as no atomic CN imperfection is justified at $i > 3$. Letting P be the crystal field and considering the contribution of the outermost three atomic layers, one obtains the size-induced crystal field and E_G expansion of an extended solid: [82, 79, 70]

$$\frac{\Delta E_G(D)}{E_G(\infty)} = \frac{\Delta V(D)}{V(\infty)} = \frac{\Delta V(r, nN)}{V(r, nN)} = \delta_{surf} \tag{2.11}$$

where $V(r, nN)$ is the total binding energy of the solid composed of n particles and, with each particle, there are N atoms. δ_{surf} represents the effect of surface relaxation:

$$\delta_{Surf} = \sum_{i\le 3}\gamma_i\left[\frac{v(d_i)}{v(d)} - 1\right] = \begin{cases} c_i^{-m} - 1, & D \sim 1nm \\ \sum_{i\le 3}\gamma_i(c_i^{-m} - 1), & D >> 1nm \end{cases} \tag{2.12}$$

where $v(d_i)$ is the binding energy density in the relaxed region, and $v(d_i) \propto E_{b,i}(d_i)$. It is interesting to note (Equation 2.12) that at the lower end of size limit, δ_{surf} corresponds directly to the relative increase of a single bond energy as $\gamma_1 \sim 1$, $\gamma_2 = \gamma_3 = 0$ and it is independent of the dimensionality. Equations (2.11) and (2.12) represent the fact that the E_G expansion of a nanometric system results from the surface bond contraction (c_i) and the rise in surface-to-volume ratio that depends on the shape (τ) and size (K) of the particles as well as the form of atomic interaction (m).

ATTENTION: The Singapore Copyright Act applies to the use of this document. Nanyang Technological University Library

2.3.3 Photoluminescence, Photoabsorption and Electron-Phonon Interaction

Size-induced energy shift of PL and PA has attracted tremendous interest. The PL energy E_{PL} is easily to be confused with the band gap of the solid, E_G.[36] It has been suggested that the energy shift of E_{PL} or E_G follows QC that is dictated by the Coulomb interaction ($\propto D^{-1}$) between the excited e-h pair separated by the nanosolid dimension D, and the kinetic energies ($\propto D^{-2}$) of the mobile carriers confined in the quantum well. However, mechanism for the size-induced E_{PA} shift and the separation between E_{PL} and E_{PA}, known as Stokes shift, [83] is yet ambiguous. The Stokes shift was ever attributed to the "surface" states,[84] or to the self-trapped excitons localized in the surface region due to the dangling bonds.[85] Actually, the Stokes shift is dominated merely by electron-phonon (e-p) interaction,[51] and therefore, one needs to find out the factors dominating e-p coupling and the quantitative correlation between the particle size, the Stokes shift and the E_G.

Figure 2.5 illustrates the effect of e-p coupling and crystal binding on the E_{PL} and E_{PA}. The energies of the ground (denoted 1) and the excited states are expressed as: [51]

$$\begin{cases} E_1(q) = A(q-q_0)^2 \\ E_2(q) = Aq^2 + E_G \end{cases} \tag{2.13}$$

Constant A determines the shape of the potential curve. The q is in the wave-vector dimension. The vertical distance between the two minima is the band gap E_G that depends functionally on the crystal field. Lateral displacement between E_1 (q) and E_2 (q) originates from the e–p coupling (lattice vibration) that can be strengthened by raising the temperature or weakening the interatomic bonding.

ATTENTION: The Singapore Copyright Act applies to the use of this document. Nanyang Technological University Library

Therefore, the blue-shift in the E_{PL} and E_{PA} is the joint contribution from the crystal binding and from the e-p coupling.

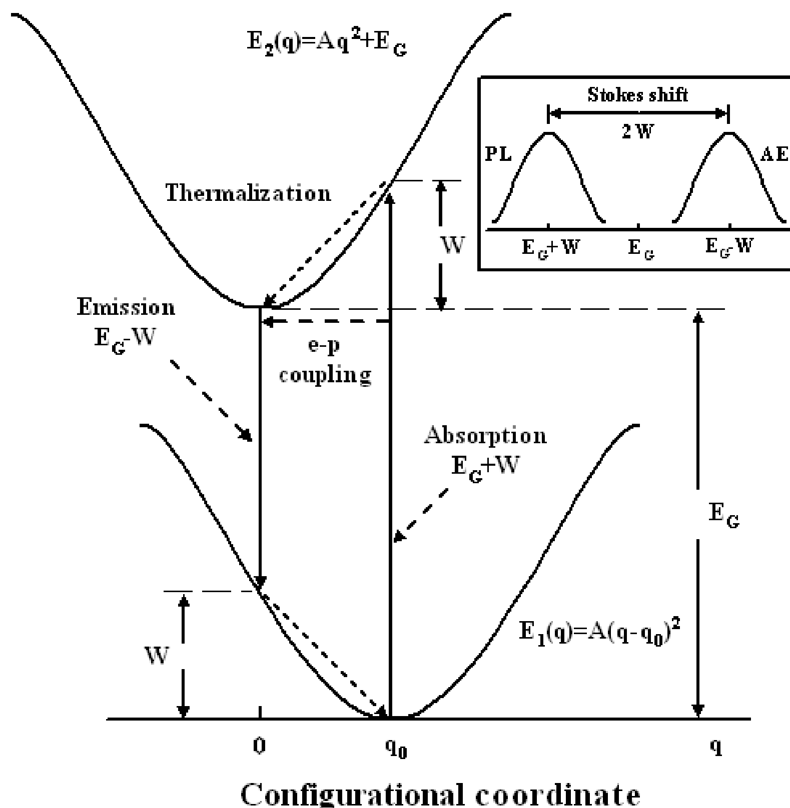

Figure 2.5 Mechanisms for E_{PA} and E_{PL} of a nano-semiconductor, involving crystal binding (E_G) and e-p coupling (W). Insert shows the Stokes shift from E_{PA} to E_{PL}. Electron is excited by absorbing a photon with energy E_G+W from the ground minimum to the excited state and then undergoes a thermalization to the excited minimum, and then transmits to the ground emitting a photon with energy E_G-W. (from Ref. 51)

At a surface, the *CN*-imperfection-enhanced bond strength affects both the frequency[86] and magnitude[87,88] of lattice vibration. Hence, at the surface, the e-p coupling and hence the Stokes shift will be enhanced. In the process of carrier formation and recombination, an electron is excited by absorbing photons with E_G+W energy from the ground minimum to the excited state with creation of an e-h pair. The excited electron then undergoes a thermalization and moves to the

ATTENTION: The Singapore Copyright Act applies to the use of this document. Nanyang Technological University Library

minimum of the excited state, and eventually transmits to the ground combining with the hole. The carrier recombination is associated with photon emission with energy $E_{PL} = E_G - W$. The transition follows the rule of momentum conservation. The insert illustrates the Stokes shift, $2W = 2Aq_0^2$, from E_{PL} to E_{PA}. The q_0 is inversely proportional to atomic distance d_i, and hence, $W = A/(c_i d)^2$, in the surface region. Based on this premise, the blue-shift of the E_{PL}, the E_{PA} and the Stokes shift can be correlated to the CN-imperfection-induced bond contraction:

$$\left.\begin{array}{l}\dfrac{\Delta E_{PL}(D)}{E_{PL}(\infty)}\\[2ex]\dfrac{\Delta E_{PA}(D)}{E_{PA}(\infty)}\end{array}\right\} = \frac{\Delta E_G(D) \mp \Delta W(D)}{E_G(\infty) \mp W(\infty)} \cong \sum_{i\le 3} \gamma_i \left[(c_i^{-m} - 1) \mp B(c_i^{-2} - 1)\right]$$

$$= \delta_{surf} \mp B\delta_{e-p} \tag{2.14}$$

$$\left(\delta_{e-p} = \sum_{i\le 3} \gamma_i (c_i^{-2} - 1);\ B = \frac{A}{E_G(\infty) d^2};\quad \frac{W(\infty)}{E_G(\infty)} \approx \frac{0.007}{1.12} \approx 0\right)$$

In the case of nano-silicon, compared with the bulk $E_G(\infty) = 1.12$ eV, the $W(\infty) \sim 0.007$ eV obtained using empirical tight-binding calculations[89,90] is negligible. The size dependent E_{PL}, E_{PA}, and $E_G = (E_{PL} + E_{PA})/2$ can be calculated with Equation (2.14). Fitting the E_{PA} and E_{PL} data obtained by others (Figures 2.6 and 2.7) gives the values of m and B. This approach discriminates the effect of e-p coupling ($B = 0.91$) from the effect of crystal binding ($m = 4.88$) on the blue-shift of both the E_{PL} and the E_{PA}.

ATTENTION: The Singapore Copyright Act applies to the use of this document. Nanyang Technological University Library

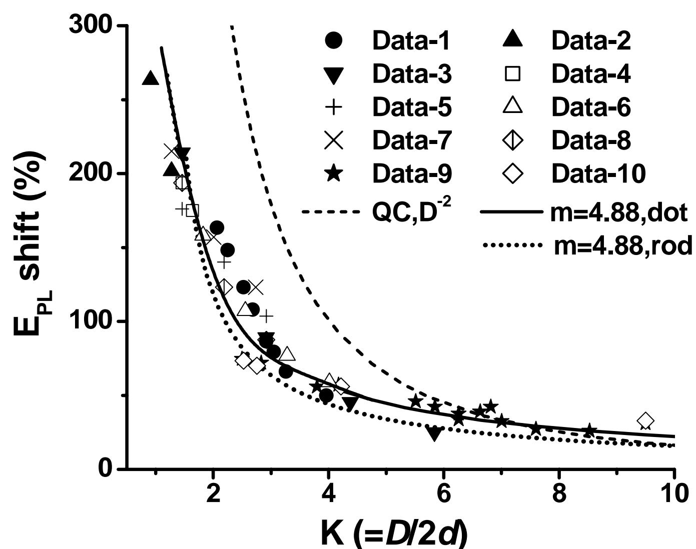

Figure 2.6 Comparison of predictions with observations on the D dependence of the E_{PL} of PS. Theoretical results: Data-1,[91] Data-2,[92] Data-3,[90] Data-4,[93] Data-5,[94] Data-6,[95] Data-7,[96] and Data-8[97]. Measurements: Data-9[98] and Data-10[72]. (from Ref. 74)

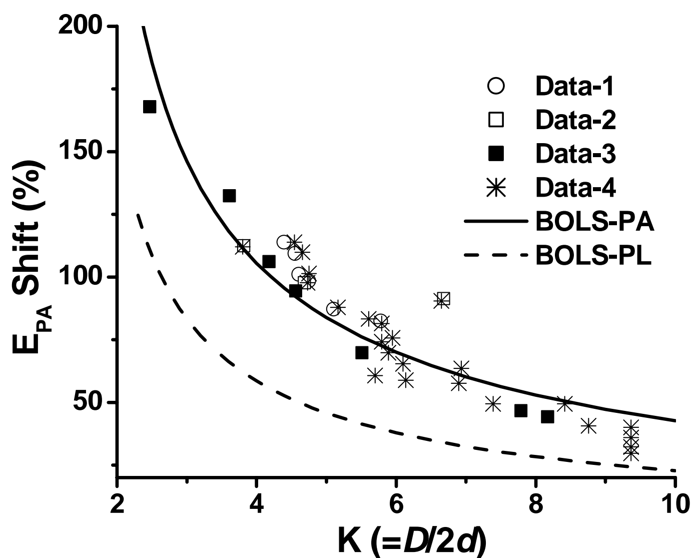

Figure 2.7 Comparison between predictions (solid line) and observations on D dependence of the E_{PA} of PS with Data-1,[99] Data-2,[65] Data-3,[100] and Data-4[98]. (from Ref. 101)

ATTENTION: The Singapore Copyright Act applies to the use of this document. Nanyang Technological University Library

Figures 2.6 and 2.7 show the matching of PL and PA shifts between observations and predictions for spherical dot and rod like structures. Apparently, simulation based on the D^{-2} QC convention in Figure 2.6 diverges from observations near the lower end of size limit. As expected, prediction based on the *BOLS* premise not only converge theory to observations but also provide interpretation that goes beyond existing D^{-n} conventions.

2.3.4 Core Level Shift

As introduced in section 2.3.2, the energy peak of a core level and the chemical satellites measured using XPS will shift up in magnitude simultaneously as E_G expands. The extent of core-level shift depends on both the original core-level position of the isolated atom and the reduced particle size. There have been a number of reports on the size dependence of the core-level shift of nanosolid materials such as *Cu*(*O*)-2*p*,[102] *Cu*-2*p*,[103] *Au*-4*f*,[104] *Sn*-3*d*, *Sn*-4*d* and *Ta*-4*f*.[105] Experimental results show that the size-induced shift follows a D^{-1}-dependent fashion. However, the underlying mechanism for the size-induced core-level shift is under debate. For instances, the size-induced core-level shift of the *Cu-O* nanosolid[102] was attributed to the enhancement of *ionicity* due to the reduction of the particle size. This means that an oxygen atom bonds more strongly to the *Cu* atoms in a nanosolid than does the oxygen atom to the *Cu* atoms inside the bulk. The enhanced core-level shift of the *O-Sn* and *O-Ta* covered metallic clusters was attributed to the contribution from *interfacial dipoles* of the nanoparticles.[105] The number or the momentum of the dipoles increases with reducing particle size. The thermochemical or the 'initial-final state' model[103,106,107] defines the shift as the

ATTENTION: The Singapore Copyright Act applies to the use of this document. Nanyang Technological University Library

difference in energy that is needed to remove a core electron either from a surface atom or from a bulk atom. The final states, or cohesive energy, of atoms at the curved surface of a nanosolid was expected to increase when the particle size is reduced. The surface atom is assumed as a 'Z+1 impurity' on the Z metal substrate. Recently, Ohgi and Fujita[104] found that the trend of Au-4f core-level shift coincides with the change of the inverse capacitance of the Au particles measured using scanning tunneling spectroscopy. However, mechanism behind the size-induced core-level shift of nanosolid Si is desirable.

Differing from the $E_G(D)$ of a nanosolid Si that can be measured approximately using the PL spectroscopy due to the involvement of e-p coupling, the atomic trapping determined core-level energy, $E_\nu(1)$, of an isolated atom, and the bulk crystal binding caused shift, $\Delta E_\nu(\infty) = E_\nu(\infty) - E_\nu(1)$, can be hardly detectable with currently available techniques. With the laser cooling technology, one can measure the energy separation between different levels of gaseous atoms trapped by the laser beams.[108] What one can measure using an XPS are the broad peaks of the core-levels resulting from contributions of atomic trapping, bulk crystal binding and the effects of surface relaxation or nanosolid formation. Therefore, separating the atomic trapping from the crystal binding in a bulk solid is a big challenge.

From Equation (2.5), the electron energy potential of a nanosolid with dimension D is given as:[74]

$$V(D) = V_{atom}(r) + V_{crystal}(r + R_C)[1 + \delta_{surf}] \tag{2.15}$$

The intraatomic trapping potential, $V_{atom}(r)$, defines the core-level position of an isolated atom, $E_\nu(1)$. The crystal potential of an extended solid, $V_{crystal}(r + R_C)$,

ATTENTION: The Singapore Copyright Act applies to the use of this document. Nanyang Technological University Library

defines not only the E_G, but also the shift of the core-level energy away from the original position, $E_\nu(\infty)$-$E_\nu(1)$. Combined Equation (2.8) with Equation (2.11), the size dependence of both E_G-expansion and E_ν-shift follow the relations:

$$\frac{E_G(D)-E_G(\infty)}{E_G(\infty)}=\frac{E_\nu(D)-E_\nu(\infty)}{E_\nu(\infty)-E_\nu(1)}=\delta_{surf} \qquad (2.16)$$

2.3.5 Dielectric Suppression

Similar to the E_G expansion and the core–level shift, the dielectric constant ε_r of the semiconductor is no longer constant but decreases with the size reduction of the solid.[109,110,71] The reduced ε_r has enormous impact on the electrical and optical performance of the solid and the related devices. For instance, the ε_r reduction enhances the Coulomb interaction between charged particles such as electrons, holes, and ionized shallow impurities in nanometric devices, leading to abnormal responses of the devices. The increase in the energies for exciton (e-h pair) activation in nanometric semiconductors due to ε_r reduction would significantly influence optical absorption and transport properties of these devices.

There have been several models to describe the size dependence of the real part of the dielectric constant, $\varepsilon_r(D)$ of a nanosolid. The relative change of the dielectric susceptibility, $\chi=\varepsilon_r-1$, can be modeled as:

$$\Delta\chi(D)/\chi(\infty)=\begin{cases}-\left[1+(D/\alpha)^{\lambda}\right]^{-1} & (Penn)\\ -2\,\Delta E_G(D)/E_G(\infty) & (Tsu)\\ -\dfrac{2}{1-(E/E_G(\infty))^2}\left(\dfrac{\Delta E_G(D)}{E_G(\infty)}\right) & (Chen)\end{cases} \qquad (2.17)$$

ATTENTION: The Singapore Copyright Act applies to the use of this document. Nanyang Technological University Library

where α and λ are freely adjustable parameters used for fitting the measured data in the Penn's empirical model.[111] Tsu *et al.*[112] related the susceptibility change directly to the $E_G(D)$. Considering the photon energy, Chen *et al.*[113] modified the Tsu's model and studied the dielectric properties of nanosolid Si embedded in SiO_2 matrix. They confirmed that the dielectric suppression is dominated by the E_G expansion. However, recent calculations by Delerue *et al.*[114] suggested that the decrease of the average dielectric response with decreasing size is due to the breaking of polarizable bonds at the surface and is not due to the E_G expansion. Actually, contribution from surface atoms and contribution from core atoms to the dielectrics are very much different. As indicated by Chen that the modified model of Tsu and Chen[112,113] is valid only at $\Delta E_G(D)/E_G(\infty) << 0.5$, otherwise χ (0) becomes negative. It is quite often that the E_G expands beyond this critical value. For instance, the E_G of Si nanorods increases from 1.1 eV to 3.5 eV with decreasing the rod diameter from 7.0 to 1.3 nm and that the surface Si–Si bond contracts by ~12% from the bulk value (0.263 nm) to ~0.23 nm.[183] Therefore, deeper insight into the origin and a clearer numerical expression with e-p coupling involvement for the dielectric suppression of a nanosolid semiconductor is highly desirable.

It is known that the static dielectric constant originates from electronic polarization, or electron transition from the lower valence band to the upper conduction band. This process is subject to the selection rule of energy and momentum conservation, which determines the optical response of semiconductors and reflects how strongly the valence electrons are coupling with the excited

ATTENTION: The Singapore Copyright Act applies to the use of this document. Nanyang Technological University Library

conduction electrons.[115] Therefore, the ε_r of a semiconductor is directly related to its E_G at RT. The involvement of e-p coupling modifies the band structure for electron excitation, as illustrated in Figure 2.5. The energy difference between the conduction band $E_C(q)$ and valence band $E_V(q)$ at q is given as:

$$\begin{aligned} E_C(q) - E_V(q) &= \hbar\omega = E_2(q) - E_1(q) \\ &= E_G - Aq_0^2 + 2Aqq_0 \\ &= E_{PL} + 2Aqq_0. \end{aligned} \tag{2.18}$$

The imaginary part of the complex dielectric constant describes the electromagnetic wave absorption and is responsible for the energy loss of incident irradiation by electron excitation from the valence band to the conduction band, and can be obtained by inserting Equation 2.18 into the relation,[116,117]

$$\begin{aligned} \varepsilon_r'(\omega) &= \frac{F}{\omega^2}\int ds \frac{f_{CV}}{|\nabla_q[E_C(q) - E_V(q)]|} = \frac{\pi F f_{CV}}{A\omega^2} q \\ &= \frac{\pi F f_{CV}}{2A^2}\frac{\hbar\omega - E_{PL}}{q_0\omega^2}, \qquad (ds = 2\pi q_0 dq) \end{aligned} \tag{2.19}$$

where s is the area difference of the two curved surfaces in q space of the upper and the lower bands. F is a constant. ∇_q is the gradient in q space. f_{CV}, the probability of inter–subband transition, should vary with the particle size. However, the size–induced change of transition probability is negligibly small because it originates from the Kubo sublevel expansion in the valence and the conduction band. For particles containing hundreds of atoms or more, the Kubo expansion is

ATTENTION: The Singapore Copyright Act applies to the use of this document. Nanyang Technological University Library

negligible. The Kramers–Kronig relation correlates the real part to the imaginary part of the dielectric constant $\varepsilon_r'(\omega)$,[118]

$$\begin{aligned}
\varepsilon_r(0)-1=\chi &= \frac{2}{\pi}\int_{\omega_0}^{\infty}\frac{\varepsilon_r'(\omega)}{\omega}d\omega \qquad (\omega_0 = E_{PL}/\hbar) \\
&= \frac{Ff_{CV}}{A^2 q_0}\int_{\omega_0}^{\infty}\frac{\hbar\omega - E_{PL}}{\omega^3}d\omega \\
&= \frac{G}{q_0 E_{PL}}, \qquad (G=\hbar^2 Ff_{CV}/2A^2)
\end{aligned} \tag{2.20}$$

Hence, the size–depressed dielectric susceptibility depends functionally on the characteristics of e-p interaction q_0 and the PL energy E_{PL}, which is in contrast with the relations given in Equation 2.17. The relative change of the susceptibility follows[36]

$$\begin{aligned}
\frac{\Delta\chi(D)}{\chi(\infty)} &= -\frac{\Delta E_{PL}(D)}{E_{PL}(\infty)} - \frac{\Delta q_0}{q} \\
&= -\frac{\Delta E_{PL}(D)}{E_{PL}(\infty)} + \frac{\Delta d_i}{d} \\
&= -(\delta_{surf} - B\delta_{e-p}) + \sum_{i\le 3}\gamma_i(c_i - 1),
\end{aligned} \tag{2.21}$$

where the last term is the bond length change due to *CN* imperfection.

2.3.6 Raman shift

Vibration of atoms at a Si surface is of increasing interest because the behavior of phonons has direct influence on the electrical and optical properties in semiconductor nanosolids, such as e–p coupling, PA, and PL.[119] The frequency of transverse optical (TO) phonon undergoes a red-shift[120] whereas the low-frequency Raman (LFR) modes are generated with a blue-shift[121] upon the size *D* of Si

ATTENTION: The Singapore Copyright Act applies to the use of this document. Nanyang Technological University Library

nanosolid being decreased. The TO red-shift has been explained in terms of surface stress[122,123] and phonon quantum confinement,[124,125] as well as surface chemical passivation.[126] However, the effect of stress is usually ignorable for hydrogenated silicon,[127,91,128] in which hydrogen atoms terminate the surface bond network, which reduce bonding strains and hence the residual stress. Phonon confinement model[124] attributes the red-shift of the asymmetric Raman line to relaxation of the *q*-vector selection rule for the excitation of the Raman active optical phonons due to their localization. When the size is decreased, the momentum conservation will be relaxed and the Raman active modes will not be limited to be at the center of the Brillouin zone.[122] A Gaussian-type phonon confinement model[125] that has been used to fit the experimental data indicates that strong phonon damping exists in the nanosolid. Calculations[129] using the correlation functions of the local dielectric constant disregarding the role of phonon damping in the nanosolid refer the TO Raman red-shift to the relaxation of the momentum conservation rules due to the finite crystalline size and the diameter distribution of nanosolid in the films. In contrast to the TO red-shift, LFR features are created upon nanosolid formation. The LFR peaks are squeezed to the blue side.[121,130] The size-dependent blue-shift is also attributed to acoustic phonons confined in the nanosolid silicon. The size dependent Raman shift is expressed as,[120,130]

$$\Delta\omega(D) = \omega(D) - \omega(\infty) = A(a/D)^{\kappa} \quad , \tag{2.22}$$

where A and κ are adjustable parameters used to fit the measured data. For the TO red-shift, $A < 0$ and $\omega(\infty) = 520$ cm^{-1} (corresponding to wavelength of 2×10^4 nm). The κ varies from 1.08 to 1.44, and 2.0.[131] The a is the lattice parameter that

ATTENTION: The Singapore Copyright Act applies to the use of this document. Nanyang Technological University Library

contracts with the solid dimension.[132] For LFR blue-shift, $A > 0$, $\kappa = 1$, and $\omega(\infty) = 0$. Therefore, the LFR results from nanosolid formation. The currently available models for the TO red-shift are based on assumptions that the materials are homogeneous and isotropic, which is valid only in the long-wavelength limit. When the size of the nanosolid is in the range of a few nanometers, the continuum dielectric models are intrinsically limited. Therefore, the existing models could not reproduce satisfactorily the Raman frequency shifts near the lower end of the size limit though they contribute to the understanding from various perspectives. Therefore, deeper insight into the physical origin of the blue-shift and red-shift is desirable.

Raman scattering is known to arise from the radiating dipole moment induced in a system by the electric field of incident electromagnetic radiation. The laws of momentum and energy conservation govern the interaction between a phonon and a photon. The total energy E due to the lattice vibration consists of the component of short-range interactions E_S and the component of long-range Coulomb interaction E_C,[130]

$$E = E_S + E_C \qquad (2.23)$$

The short-range interaction corresponds to the TO mode, which describes the covalent bonding and thus is correlated to bond energy E_b, bond length d, and the coordination number (CN, or z). The long-range part corresponds to the LFR mode and represents the weak interaction between nanosolids.

Figure 2.8 shows the least-squares fitting of the size dependent LFR frequency for the nanosolid silicon. The LFR frequency depends linearly on the inverse D. The zero intercept at the vertical axis indicates that when D increases toward

ATTENTION: The Singapore Copyright Act applies to the use of this document. Nanyang Technological University Library

infinity, the LFR peaks disappear, which implies that not only the blue-shift in the LFR peaks but also the origin for the LFR peaks are purely intergrain vibrations that produce acoustic phonons. The slope values are 195.54, 91.14, and 67.56 for the A_1, T_2, and E modes, corresponding to the stretching (LA) and bending (TA), respectively.

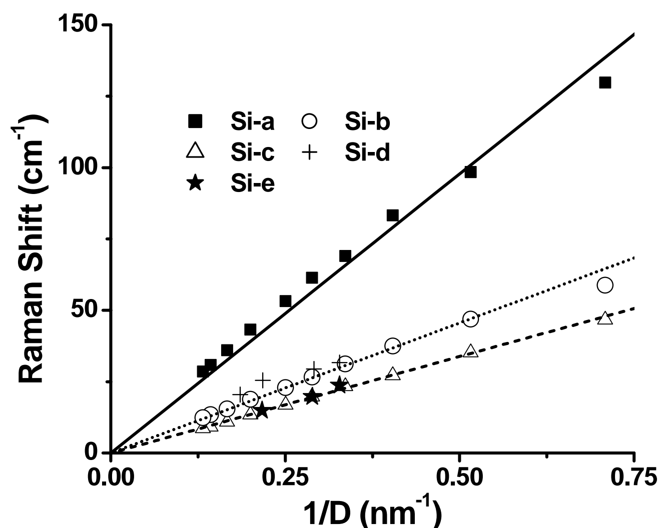

Figure 2.8 Generation and blue-shift of the LFR spectra where the solid, dotted and dashed lines are the corresponding results of the least-squares fitting. The Si-a (A_1 mode), Si-b (T_2 mode), and Si-c (E mode) are calculated from the lattice-dynamic matrix by using a microscopic valence force field model;[130] The Si-d and Si-e are the experimental results.[121] (from Ref. 133)

For the Raman TO mode, the energy due to short-range interaction of a single pairwise bond can be expressed in a Taylor's series,

$$\begin{aligned} E_S &= \sum_{n=0} \left(\frac{d^n u(r)}{n! dr^n} \right)_{r=d} (r-d)^n \\ &= u(d) + 0 + \left. \frac{d^2 u(r)}{2! dr^2} \right|_d (r-d)^2 + \dots \end{aligned} \tag{2.24}$$

ATTENTION: The Singapore Copyright Act applies to the use of this document. Nanyang Technological University Library

When the atom is in the equilibrium position, the bond energy is $u(d) = E_b$. The third term is the vibration energy due to the short-range interaction, in which, the force constant $k = d^2u(r)/dr^2\big|_d \propto E_b / d^2$ and the vibration amplitude $x = r - d$. For a single bond, the k is strengthened but for a single lower-coordinated atom, the resultant k could be lower. Because the short-range interaction on each atom results from its neighboring coordination atoms, the atomic vibrating dislocation is the contribution from all the surrounding coordinates, z. Considering the vibration amplitude $x \ll d$, it is reasonable to take the mean contribution from each coordinate as a first order approximation, i. e., $k_1 = k_2 = \ldots = k_z = \mu_{Si}(c\omega)^2$, and $x_1 = x_2 = \ldots = x_z = (r-d)/z$. Therefore, the energy due to short-range interaction of a certain atom with z coordinates follows:

$$\begin{aligned} E_S &= \sum_z \left[-E_b + \frac{1}{2}\mu_{Si}c^2\omega^2\left(\frac{r-d}{z}\right)^2 + \ldots. \right] \\ &= -zE_b + \frac{1}{2z}\mu_{Si}c^2\omega^2(r-d)^2 + \ldots \end{aligned} \tag{2.25}$$

where $\mu_{Si} = m_{Si}/2 = 2.34\times10^{-26}$ kg is the reduced mass of a Si–Si dimer and c is the speed of light. Equilibrating Equation (2.25) to (2.24) times z, we have the phonon frequency (wavenumber, ω) as follows:

$$\omega = \frac{1}{c}\left(\frac{z}{\mu_{Si}}\right)^{\frac{1}{2}}\left[\frac{zd^2u(r)}{dr^2}\bigg|_d\right]^{\frac{1}{2}} \propto \frac{z(E_b)^{1/2}}{d} \tag{2.26}$$

Combining Equations (2.9) and (2.26) give the size-dependent TO red-shift:

$$\frac{\omega(D)-\omega(\infty)}{\omega(\infty)-\omega(1)} = \sum_{i\le3}\gamma_i\left[\frac{\omega_i}{\omega_b}-1\right] = \sum_{i\le3}\gamma_i\left[\frac{z_i}{z_b}c_i^{-\left(\frac{m}{2}+1\right)}-1\right] = \delta_p < 0 \tag{2.27}$$

ATTENTION: The Singapore Copyright Act applies to the use of this document. Nanyang Technological University Library

$\omega(1)$ is the vibrational frequency of an isolated Si–Si dimer bond, which is the reference point for the TO red-shift upon nanosolid and bulk formation ($P(\infty) = \omega(\infty) - \omega(1)$ is the bulk shift).

2.4 Summary

We have thus presented a new approach based on the *BOLS* correlation premise that is not only able to converge the ΔE_{PL} and ΔE_{PA} ($D \rightarrow 0$) of the smallest nanosolid to the data and but also able to deepen our insight into the physical origin of E_G expansion, core level shift, dielectric suppression, Raman shift, PL and PA blue-shifts, and e-p interaction upon nanosolid formation. Differing from the currently available theories, the present model, without any assumption or freely adjustable parameters, emphasizes that E_G expansion, Si-2*p* core level shift, and Raman shift relate to the Hamiltonian that is subject to the modification by surface *CN*-imperfection and its effect on the binding energy density in the relaxed region. And the PL and PA blue-shifts and dielectric suppression relate directly to the crystal binding density and the e-p coupling. This approach provides us deeper insight into the unusual behavior of photons, electrons, and phonons in a nano-semiconductor. As indicated by Glinka *et al*,[66] the QC theory may not be always necessary.

ATTENTION: The Singapore Copyright Act applies to the use of this document. Nanyang Technological University Library

Chapter 3 Experimental Approaches

3.1 Sample Preparation: Porous Silicon

3.1.1 Electrochemical formation

PS is formed by an electrochemical etching of Si in an HF solution. Following an electrochemical reaction occurring at the Si surface a partial dissolution of Si settles in. There are several factors which rule this process.

(i) Electrolyte. Due to the hydrophobic character of the clean Si surface, absolute ethanol is usually added to the aqueous HF solution to increase the wettability of the PS surface and reduce the surface tension at the silicon-solution interface. In fact, ethanoic solutions infiltrate the pores, while purely aqueous HF solutions do not. This is very important for the lateral homogeneity and the uniformity of the PS layer in depth. In addition, during the reaction there is hydrogen evolution. Bubbles form and stick on the Si surface in pure aqueous solutions, whereas they are promptly removed if ethanol (or some other surfactant) is present.

(ii) Potential. The dissolution is obtained by controlling either the anodic current or the potential. Generally, it is preferable to work with constant current, because it allows a better control of porosity, thickness and reproducibility of the PS layer.

(iii) Cells. The electrochemical cell is a Teflon beaker (Figure 3.1). The Si wafer acts as the anode and the cathode is generally made of platinum. The cell body

ATTENTION: The Singapore Copyright Act applies to the use of this document. Nanyang Technological University Library

is usually made of a highly acid resistant polymer such as Teflon. The advantages of this cell geometry are the simplicity of equipment and the ability to anodize silicon-on-insulator structures.

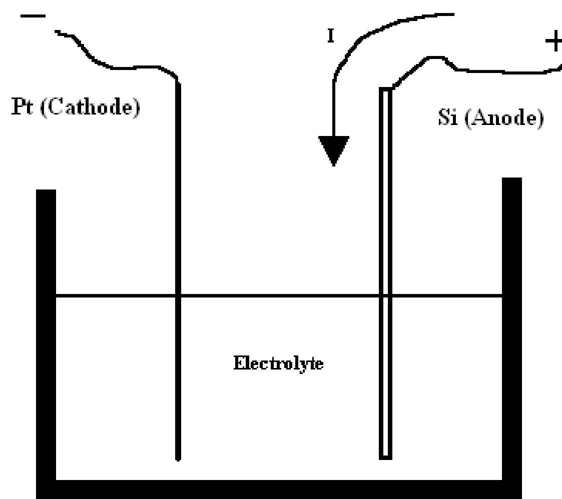

Figure 3.1 Cross-sectional view of a lateral anodization cell.

3.1.2 Dissolution Chemistry

A silicon surface is known to be virtually inert against attack of hydrofluoric acid at low pH values, which corresponds to low OH^- concentrations. When a potential is applied to Si in aqueous solution, a measurable external current flows through the system. However, for any current to pass the Si/electrolyte interface, it must first change from electronic to ionic current. This means that a specific chemical redox reaction must occur at the Si interface. Application of a potential then induces a precisely chemical reaction, the nature of which is fundamental to the formation of PS.

ATTENTION: The Singapore Copyright Act applies to the use of this document. Nanyang Technological University Library

The exact dissolution chemistries of Si are still in question, and different mechanisms have been proposed. However, it is generally accepted that holes are required for pores formation. During pore formation two hydrogen atoms evolve for every Si atom dissolved.[134,135] The global anodic semi-reactions can be written during pore formation as

$$Si+6HF \rightarrow H_2SiF_6+H_2+2H^++2e^-$$

The final and stable product for Si in HF is in any case H_2SiF_6 or some of its ionized forms. This means that during pore formation only two of the four available Si electrons participate in an interfacial charge transfer, while the remaining two undergo corrosive hydrogen liberation.

Lehmann and Gösele[15] have proposed a dissolution mechanism which is so far the most accepted (Figure 3.2). It is based on a surface bound oxidization scheme, with hole capture, and subsequent electron injection, which leads to the divalent Si oxidization state.

According to Figure 3.2, the Si hydride bonds passivate the Si surface unless a hole is available. To understand how H-termination is achieved, one must understand why the surface is H terminated in the first place. Indeed, some authors have argued that fluorine terminates HF-treated surfaces[136] because of the relative strength of the SiF versus the SiH bonds (~6 eV vs ~3.5 eV). Furthermore, F termination of the silicon interface is expected to be final step of oxide removal, given the accepted mechanism of oxide etching. Therefore, the observation of atomic H on the surfaces[137,138] clearly indicates that the termination is largely determined by reaction kinetics rather than thermodynamics alone.

ATTENTION: The Singapore Copyright Act applies to the use of this document. Nanyang Technological University Library

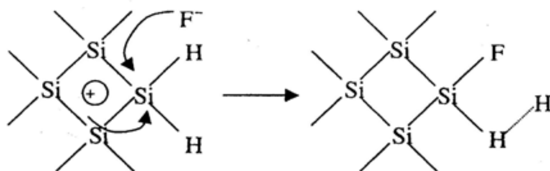

(i) Hole injection and attack on a Si-H bond by a fluoride ion

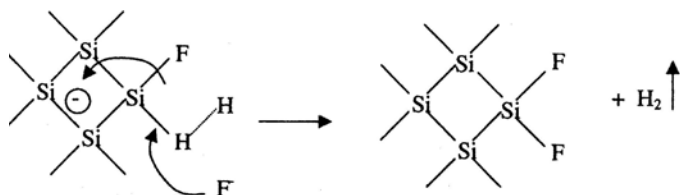

(ii) Second attack by a fluoride ion with hydrogen evolution and electron injection into the substrate

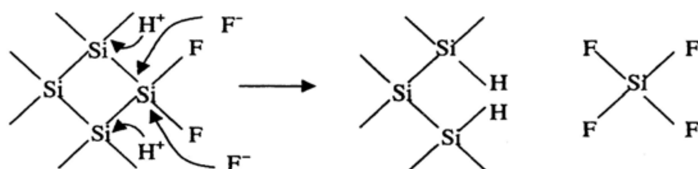

(iii) HF attack to the Si-Si backbonds. The remaining Si surface atoms are bonded to the H atoms and a silicon tetrafluoride molecule is produced

(iv) The silicon tetrafluoride reacts with two HF molecules to give H_2SiF_6 and then ionizes

Figure 3.2 Silicon dissolution scheme proposed by Lehmann and Gösele. (from Ref. 15)

A simple explanation for the observed H termination was first proposed by Ubara *et al.*[137] on the basis of infrared measurements of HF-treated microcrystalline silicon samples. They postulated that F-terminated silicon

ATTENTION: The Singapore Copyright Act applies to the use of this document. Nanyang Technological University Library

complexes are unstable in HF solutions due to strong polarization of the Si-Si back bonds (e.g., $\equiv Si^{-} - Si^{+}F_3$) facilitating their attack by HF molecules. This results in reactions such as $\equiv Si - SiF_3 + HF \rightarrow \equiv SiH + SiF_4$ which release silicon fluorides into solution leaving a H-terminated surface behind. This hypothesis is also supported by the experimental observation that hydrogen gas continues to evolve from the porous layer and the presence of Si-H_x group by FTIR (section 4.2) and SIMS[139] measurements.

3.1.3 Pore Formation

While it is generally accepted that pore initiation occurs at surface defects or irregularities, different models have been proposed to explain pore formation in PS.[140,141] Some basic requirements have to be fulfilled for electrochemical pore formation to occur.[142]

1. Holes must be supplied by bulk Si, and be available at the surface.
2. The interface of *p*-type silicon and aqueous HF acid behaves like a Schottky diode. The Fermi-level of the HF is higher than that of silicon. There is a Schottky potential barrier height generated at the silicon/electrolyte interface which induces a surface depletion region on the Si surface. The depletion region width is proportional to the built-in potential in Si. When a current density is applied to the silicon wafer located at the anode, a positive voltage drops across the depletion region. The built-in potential and the depletion width are reduced. At a local area of

ATTENTION: The Singapore Copyright Act applies to the use of this document. Nanyang Technological University Library

the Si surface with higher surface energy, which could be a kink site or a step, holes are enforced from bulk Si to the Si/electrolyte. The electrochemical etching and some pores are formed because the participation of holes. As the reaction continues, these pores are etched deeply and widely. When the depletion regions of adjacent pores meet, the Si wire size is determined because there is no hole available there.

3. While the pore walls have to be passivated, the pore tips have to be active in the dissolution reaction. Consequently, a surface which is depleted of holes is passivated to electrochemical attach, which means that (i) the electrochemical etching is self-limiting and (ii) hole depletion occurs only when every hole that reaches the surface reacts immediately.

3.1.4 Drying of the samples

The drying of PS layers, especially those of high porosities, is a crucial step. After the formation of a highly porous PS layer, when the electrolyte evaporates out of the pores, cracking of the layer is systematically observed. The origin of the cracking is the large capillary stress associated with the evaporation from the pores. During the evaporation a gas/liquid interface forms inside the pores and a pressure drop Δp ($\Delta p \propto \gamma$, γ is the liquid surface tension) occurs. Pentane is generally used as drying liquid in that it has a very low surface tension and is able to reduce strongly the capillary tension.[143] Using this drying technique PS layers with porosity values up to 90% exhibit no cracking pattern after drying.

ATTENTION: The Singapore Copyright Act applies to the use of this document. Nanyang Technological University Library

3.2 Size Control

All the properties of PS, such as porosity, thickness, pore diameter and microstructure, depend on anodization conditions. These conditions include HF concentration, current density, wafer type, resistivity, anodization duration, temperature, and drying conditions.

3.2.1 Porosity

The porosity is defined as the fraction of void within the PS layer and can be easily determined by weight measurement. The wafer is weighted before anodization (*m*1), just after anodization (*m*2), and after a rapid dissolution of the whole porous layer in a 3% KOH solution (*m*3). The porosity is given by the following equation:

$$p(\%)=(m1-m2)/(m1-m3) \qquad (3.1)$$

3.2.2 Fabrication Method

The PS samples were prepared on *p*-type (100) Si wafers of 1–25 Ωcm resistivity at RT. Electrolyses were performed in a HF:C_2H_5OH:H_2O solution with 1:5:4 weight ratio by a galvanostat, while the electrolyte was stirred during the process. The Si substrates were used as anodes and *n*-type Si of 0.005–0.02 Ωcm resistivity was used as a cathode to obtain a more homogeneous electric field in the electrolyte leading to samples with very uniform surfaces.[144] A current density of 30 ~ 90 mA/cm^2 was applied for 10 min. After anodization, all the PS samples

ATTENTION: The Singapore Copyright Act applies to the use of this document. Nanyang Technological University Library

were dried by pentane to prevent them from cracking[143] (when the pentane is applied after the anodic reaction, it also reduces the number of Si–O bonds allowing an increase of the Si–H bonds[145]). The porosity and the size of nanocrystals were controlled by varying the current density. An increase in current density will give rise to an increase in the porosity with a consequent reduction in the size of the nanocrystals.[146,147] This can be explained by higher current density resulting in smaller built-in potential, thinner depletion region width and thus thinner Si dot.

3.2.3 Surface Morphology

Conventionally, the particle (crystallite) size D of PS can be estimated from the full width at half maximum (FWHM) H of the 0.5º grazing angle x-ray diffraction (XRD) peak[148] by Scherrer's equation:[149] $D = C\lambda/H\cos\theta$. Where λ is the x-ray wavelength (Cu $K_{\alpha 1}$ 1.54 Å), θ is Bragg angle. C is a factor (typically 1.0) depending on crystallite shape. Figure 3.3 is a XRD pattern for PS, prepared at an anodic current density of 50 mA/cm^2, which shows a prominent peak at $2\theta \approx 55.9^{\circ}$ representing the (311) plane in silicon. The signal from c-Si is significantly stronger than the one from PS (~100 times) while PS XRD shows a broader contour (FWHM ~1.6º) as compared with c-Si (FWHM ~0.5º) The average particle size of PS deduced from the measurement is found to be about 6 nm.

However, the XRD measurement as well as conventional Raman diagnostics are not reliable ways to measure the crystallite size in PS because they cannot

ATTENTION: The Singapore Copyright Act applies to the use of this document. Nanyang Technological University Library

detect nanocrystallites with a grain size lower than 5 nm.[150] High resolution transmission electron microscopy allows direct detection of very small nanocrystals, but it is destructive and not applicable as a routine analysis. Here we suggest a simple method to deduce the average particle size of PS. Based on the theory in section 2.3.3, the particle size can be obtained by matching the measured PL shift to the predicted PL Profile in Figure 2.6 that has matched numerous sets of PL data of PS, CdS and CdSe nanosolids.[74,151] Such a method has been used by Wolkin *et al*.[152]

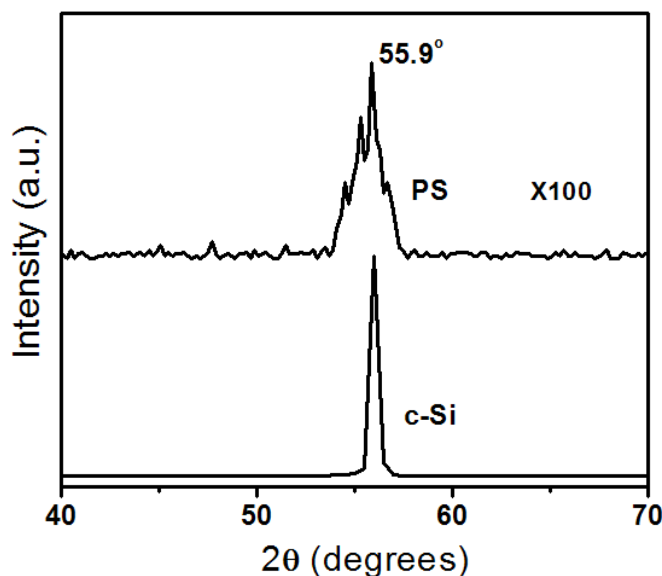

Figure 3.3 XRD spectra of PS and c-Si recorded at a glancing angle of 0.5º which exhibit a peak at $2\theta \approx 55.9^{\circ}$ correlating to (311) planes.

Figure 3.4 shows atomic force microscopy (AFM) image of PS surface which is a three-dimensional pattern formed by an interconnecting skeleton of particles. A fractal skeleton structure of wires, hillocks and holes in various scales can be observed in Figure 3.4.

ATTENTION: The Singapore Copyright Act applies to the use of this document. Nanyang Technological University Library

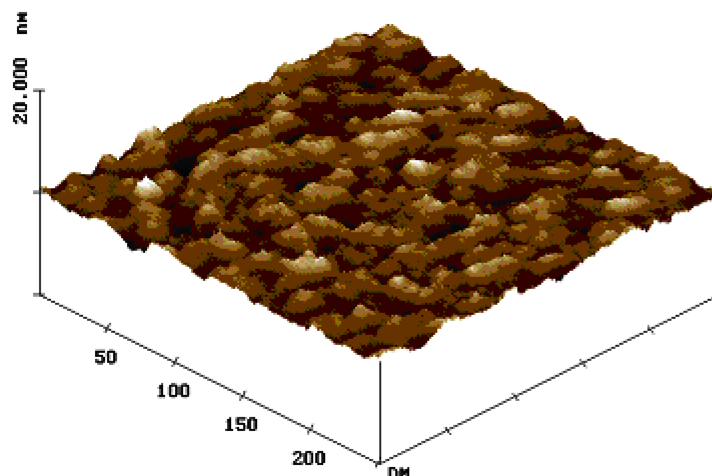

Figure 3.4 Three-dimensional AFM image of PS surface (R_{rms}=1.5 nm)

3.3 Surface Passivation

The role of the surface in the optical and dielectric properties of PS remains a key issue.[153,154] Although the burden of evidence points towards some intrinsic radiative mechanism in small silicon particles, the influence of the surface and ways of controlling surface interactions will always be important.[155,156,157] The basic idea of passivation is to replace the easily broken Si–H surface bond by other species such as Si–F bond. Plasma treatment is a major step in ultralarge scale integrated circuits as one of the effective methods to passivate semiconductor surfaces or to form ultra-thin oxide or nitride on surfaces such as N_2O-plasma oxidation of *a*-Si:H,[158,159] NH_3-plasma nitridation of GaAs,[160] and N_2-plasma nitridation of PS.[161]

ATTENTION: The Singapore Copyright Act applies to the use of this document. Nanyang Technological University Library

Plasma-Enhanced Chemical Vapor Deposition (PECVD)

PECVD is a technique for the deposition and passivation of a wide variety of films by breaking down gaseous precursors into radicals which deposit onto a substrate. The advantages of radio frequency (rf) PECVD include: the composition of passivated films can be accurately controlled; the system is simple and the operation is reasonably well understood; asymmetric discharges yield inherently uniform plasmas that can be scaled over large areas; asymmetric discharges where the chamber wall is a large grounded electrode offering large processing volumes; rf diodes yield ion-bombarding energies that are sufficient for most processes.

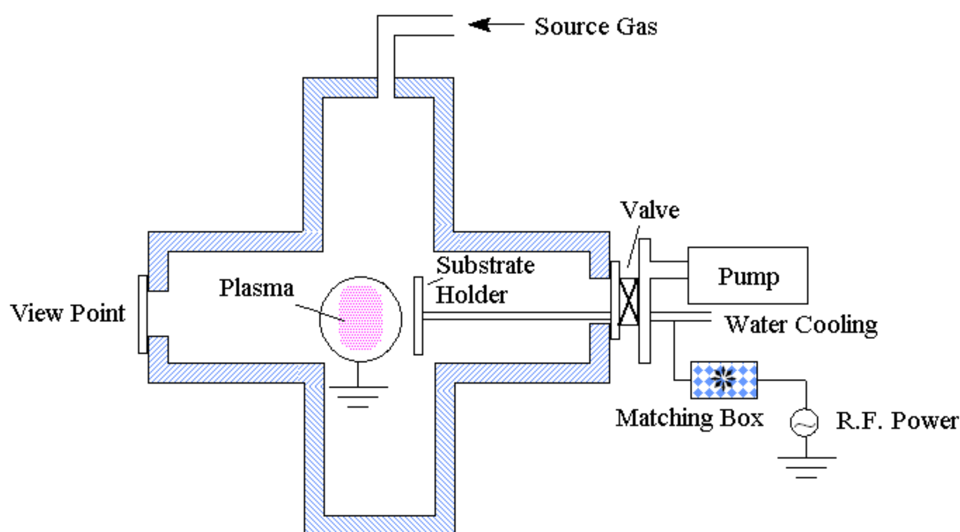

Figure 3.5 A schematic diagram of the PECVD system

Surface fluorination was performed on PS with CF_4 plasma at RT by a PECVD system in an asymmetric configuration. This configuration uses a grounded electrode larger than the cathode, and thus ensures the generation of self-bias. The chamber base pressure is less than 5×10^{-5} Torr, which is maintained by a turbo-molecular pump. The deposition chamber consists of a cross shaped stainless-steel

ATTENTION: The Singapore Copyright Act applies to the use of this document. Nanyang Technological University Library

cylinder (20 cm in diameter and 40 cm in length). The substrate electrode (14 cm in diameter) is water cooled, and coupled to an rf generator (rf excited frequency is 13.56 MHz) by an impedance-matching network and a blocking capacitor. The rf power is applied between the ground and substrate electrode which is placed at the center of the chamber. The schematic diagram of the PECVD system is shown in Figure 3.5. The substrate electrode is subject to a negative DC self-bias voltage, which is controlled by the rf input power. The bias voltage increases almost linearly with the rf power, due to the increasing ionization in the plasma with the rf power.

3.4 Surface Metalization

Over the last a few years, PS has been regarded as a promising material for applications in the microelectronics such as waveguides,[162] photodiodes[163] and various types of sensors.[164] These applications usually require some kind of metal layers or metallic patterns on the top of the PS substrate (electrodes, contact masks, mechanical support, etc.). Furthermore, PS layers have also been proposed for potential application as the host matrix for polymers or metals, which have interesting optical properties.[143] For example, Pt-coated *n*-type PS electrodes have shown good solar energy conversion.[165] Consequently, a thorough study of the metal-PS structure is necessary for PS-related devices. Currently, there are many methods for the metal deposition such as electrodeposition and vacuum deposition, etc. Generally, wet chemical methods like electrodeposition introduce additional damage to the unstable PS surface with more surface contamination, although pore

ATTENTION: The Singapore Copyright Act applies to the use of this document. Nanyang Technological University Library

filling is very effective. Thus, vacuum deposition process is a better choice for keeping the PS characteristics as far as unchanged.[166]

Filtered Cathodic Vacuum Arc (FCVA) Deposition

FCVA deposition technique belongs to the family of ion beam deposition, and is proved to be an efficient method for the metal deposition.[167,168] The system incorporates the off-plane double-bend (OPDB) with a filter inside to effectively remove macro-particles. The advantages of FCVA technique include: the working pressure is very low (around 4×10^{-5} Torr); the OPDB filter enables high quality and macroparticle-free film deposition; and the deposition rate is relatively high.

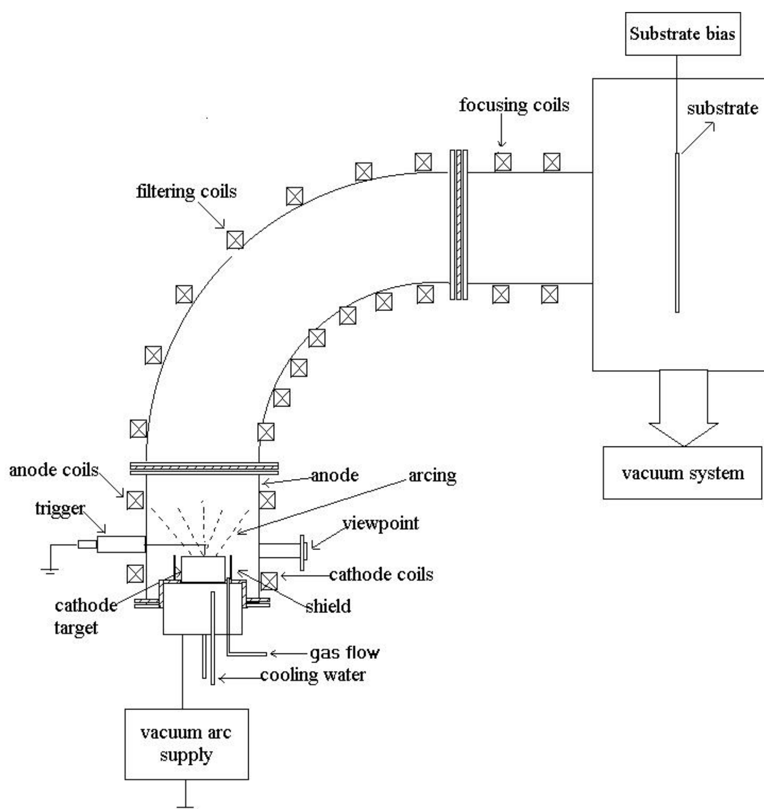

Figure 3.6 Schematic diagram of the FCVA deposition system

ATTENTION: The Singapore Copyright Act applies to the use of this document. Nanyang Technological University Library

Cu, Al, and Ti were deposited on the surface of PS by a FCVA system, as shown in Figure 3.6. The whole system consists of a cathodic arc source, a plasma filtering duct, and a deposition chamber. The chamber base pressure is less than 10^{-5} Torr which is maintained by a rotary-cryogenic pump. The cathodic vacuum arc source is comprised of five main parts: anode wall, power supply, arc trigger, target, and the target-cooling system. The power supply is an electrical welding machine with a maximum current of 250 A. The anode is grounded and the cathode is connected to the target. A shield is placed around the target to stabilize the plasma with a fixed direction between the cathode and the anode. The toroidal solenoid is a steel OPDB torus with a copper wound outside, which avoids a straight-line path between the cathodic arc source and the substrate, and thus prevents neutral particles from reaching the deposition chamber. A set of baffles as a mechanical macroparticle filter is installed inside the torus to enhance the macroparticle filtering efficiency.

3.5 Characterization Equipment

1. Photoluminescence

The PL spectra were measured with a SPEX FLUOROLOG-3 spectrofluorometer equipped with a xenon lamp. A strong excitation peak was observed at 458 nm. Samples were therefore excited with the 458 nm light at RT. The E_{PL} value was the PL peak energy.

2. Reflection & Absorption

ATTENTION: The Singapore Copyright Act applies to the use of this document. Nanyang Technological University Library

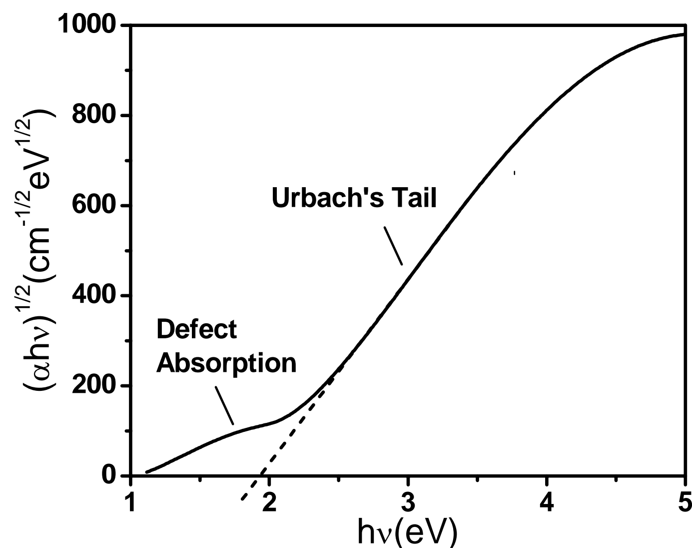

Figure 3.7 $(\alpha h\nu)^{1/2}$ vs. $h\nu$ plot for PS sample. α is the absorption coefficient and $h\nu$ is the photon energy. The square root of $\alpha\hbar\nu$ is a linear function of photon energy, as expected for an indirect band gap semiconductor.[169] The figure shows the resolution of the absorption spectrum into separate contributions (Urbach's tail and defect aborption).[170] The E_{PA} value is obtained by linear extrapolation to zero absorption.

The reflection spectra were measured using a Perkin Elmer Lamda 16 UV/VIS spectrometer; and the absorption coefficient was obtained by fitting the reflection spectra using the Scout commercial software.[171, 172] Lehmann *et al.*[173] and Butturi *et al.*[174] have also derived their absorption data by fitting reflection spectra. The E_{PA} value was extracted from the absorption spectra using the Tauc plot method,[99, 175,176,177,178] as shown in Figure 3.7.

3. Si-2*p* level

XPS Si-2*p* profiles were measured using a Kratos AXIS spectrometer with monochromatic Al k_α ($h\nu$ = 1486.71 eV) radiation at ambient temperature. The

ATTENTION: The Singapore Copyright Act applies to the use of this document. Nanyang Technological University Library

shift of the binding energy due to charging was corrected using C1s binding energy (284.8 eV) from the surface C contamination.

4. Dielectric Constant

The dielectric measurements were performed in the frequency range of 50 Hz–1.0 MHz under an applied potential of 100 mV, using a FLUKE PM–6303 resistance–capacitance–inductance meter with a four–wire probe. All the measurements were carried out in atmospheric ambient. Figure 3.8 shows a schematic diagram of this dielectric measurement. Because PS has low conductivity, which is lower by several orders of magnitude compared with a Si substrate,[179, 140,180] i.e. the resistivity of the Si substrate is much lower than that of PS, the effects of conducting current through the Si substrates on the resistance measured were estimated to be less than 0.1%, and thus the effect of the Si substrates could be ignored.[181,182] Silver paste was used as an ohmic contact. The samples were then dried at 353 K for 1 h to make the experimental data reproducible.

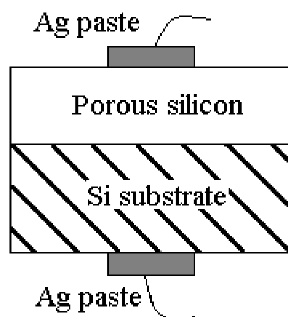

Figure 3.8 Schematic diagram of the dielectric measurement.

ATTENTION: The Singapore Copyright Act applies to the use of this document. Nanyang Technological University Library

Chapter 4 Optical and Dielectric Properties

4.1 Introduction

In Chapter 2, we have introduced *BOLS* correlation in details. This premise indicates that *CN*-imperfection induced surface bond contraction is responsible for the unusual behavior of photons, phonons, and electrons in PS. In this chapter consistency between predictions and experimental data on size-dependent E_G expansion, Si-2*p* core level shift, dielectric suppression, and Raman shift further evidence the essentiality and validity of this premise.

4.2 Experimental Details

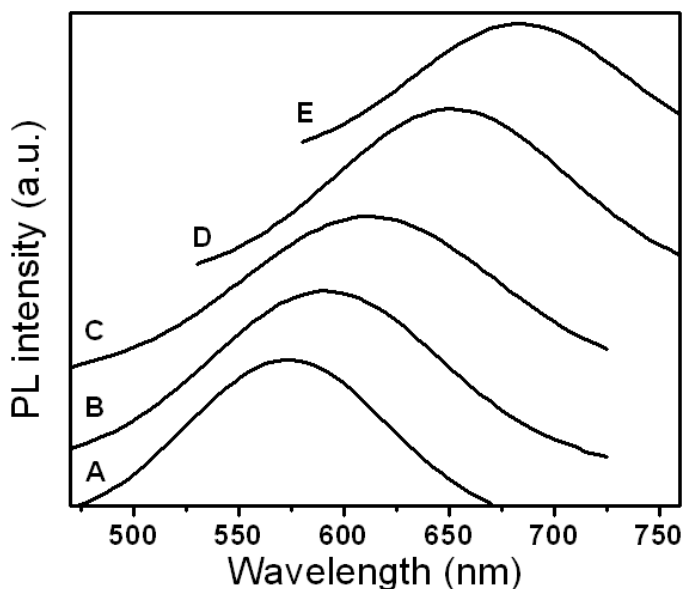

Figure 4.1 RT PL spectra of PS samples. (from Ref. 101)

ATTENTION: The Singapore Copyright Act applies to the use of this document. Nanyang Technological University Library

Table 4.1 Measured E_{PL} and derived information on particle size D of PS.

Sample	λ-PL (nm)	E_{PL} (eV)	D (nm)
A	575.3	2.16	1.4±0.02
B	591.9	2.07	1.6±0.01
C	611.8	2.03	1.7±0.01
D	650.4	1.91	1.9±0.02
E	683.4	1.81	2.1±0.03

The PS samples were prepared according to the fabrication procedures introduced in section 3.2.2 with different current densities. Their PL spectra were measured to determine their particle sizes according to the method introduced in section 3.2.3. Figure 4.1 shows the PL spectra of as-etched PS samples. Corresponding PL peak energy E_{PL} determined by the Gaussian curve fitting of PL spectra in Figure 4.1 and derived sizes obtained by matching the measured PL shift in Figure 4.1 to the predicted PL Profile in Figure 2.6 are shown in Table 4.1.

Figure 4.2 shows the FTIR analysis results of PS samples. There are mainly four absorption bands: 667 cm^{-1}, 820–890 cm^{-1}, 995–1110 cm^{-1} and 1110–1200 cm^{-1}. The absorption peak at 667 cm^{-1} is due to Si–H deformation mode. In spectral range from 820–890 cm^{-1} the following peaks are identified: 827 cm^{-1} related to Si–O bending mode in Si–O–Si; 840 cm^{-1} related to Si–H bending mode in $SiH(SiO_2)$; and 856 cm^{-1} related to H–Si–H wagging mode and 874 cm^{-1} related to Si–H bending in $SiH(O_3)$. The absorption located at 1062 and 1145 cm^{-1} are attributed to Si–O–Si stretching mode. The absorption peaks located at 977 and

ATTENTION: The Singapore Copyright Act applies to the use of this document. Nanyang Technological University Library

940 cm^{-1} are due to the trace existence of fluorine, which is consistent with the XPS measurement results in Figure 5.1. From Figure 4.2, it is noticed that the decrease in particle sizes leads to an enhancement of the spectral lines intensities in the absorption peak at 667 cm^{-1}, i.e. denser concentration of H contained in PS surface. An explanation is that the PS specific surface enlarges as a result of the increase in porosity with the size reduction.

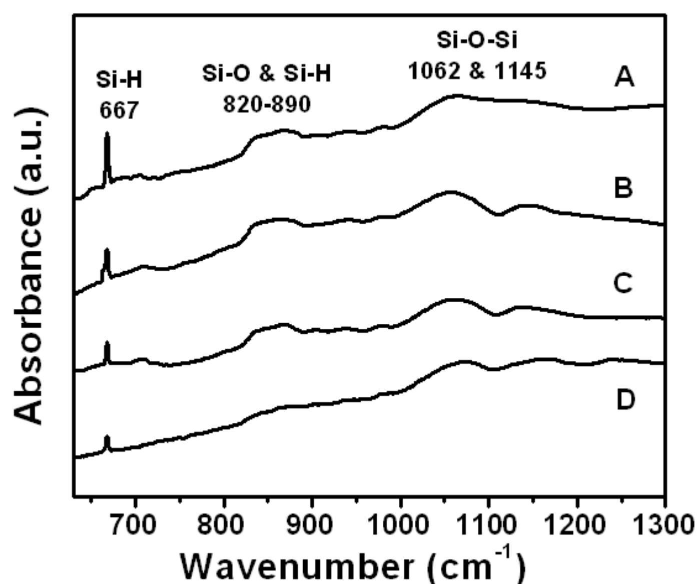

Figure 4.2 The FTIR spectra of PS samples with different particle sizes.

4.3 Size Dependent Property Variations

4.3.1 Band Gap Expansion

Figure 4.3 (a) shows the RT reflection spectra of the fresh PS. The reflectivity varies with the size reduction in the range of 200–900 nm, which is related to the change of dimension and geometry of columns and voids on the PS surface. Figure 4.3 (b) sketches the absorption coefficient of PS samples. The calculated E_{PA}

ATTENTION: The Singapore Copyright Act applies to the use of this document. Nanyang Technological University Library

values are shown in Table 4.2 and the corresponding E_G of PS samples are derived from the equation $E_G = (E_{PL} + E_{PA})/2$.

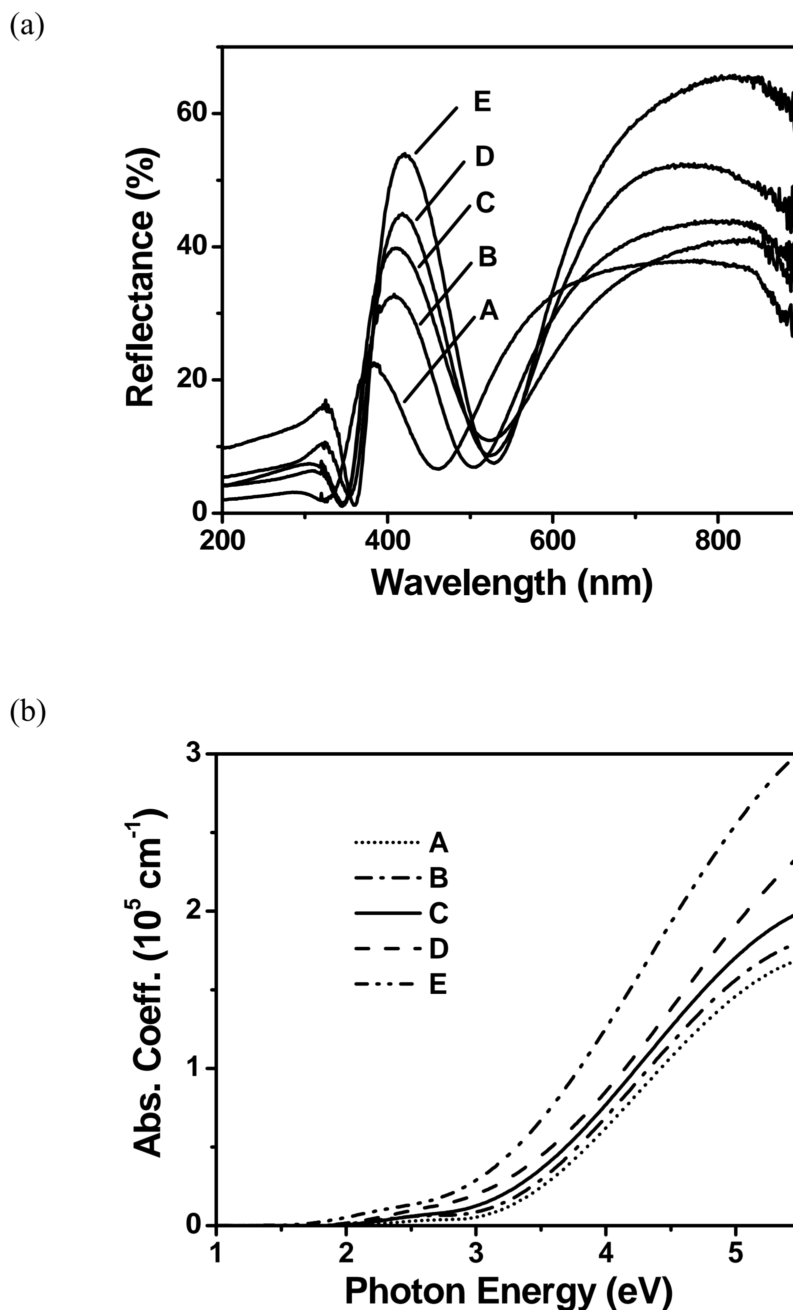

Figure 4.3 Room temperature (a) reflection spectra, and (b) absorption spectra of PS samples with different particle sizes, from which the E_{PA} is obtained with the Tauc plot fitting. (from Ref. 101)

ATTENTION: The Singapore Copyright Act applies to the use of this document. Nanyang Technological University Library

Table 4.2 E_{PA} and derived information on E_G of PS.

Sample	D (nm)	E_{PA} (eV)	E_G (eV)
A	1.4	2.72	2.44
B	1.6	2.62	2.35
C	1.7	2.60	2.32
D	1.9	2.45	2.18
E	2.1	2.16	1.99

It is noticed that the E_G expands with the size reduction, which has been explained based on the *BOLS* model (Chapter 2). Most strikingly, without igniting e-p interaction or e-h production, scanning tunneling spectroscopy (STS) revealed that[183] the E_G of Si nanorods increases from 1.1 eV to 3.5 eV with decreasing D from 7.0 to 1.3 nm; and that the surface Si–Si bond contracts by ~12% from the bulk value (0.263 nm) to ~0.23 nm. This finding concurs excitingly with our *BOLS* premise: *CN*-imperfection induces the remaining bonds of the lower-coordinated atoms to contract spontaneously associated with E_G expansion. An STS collects *localized* E_G information without needing any energetic stimulus. The tip-surface bias (2 eV) is not sufficient to break the bond. What happens upon being biased is that the tip introduces holes or electrons into the solid rather than creates e-h pairs inside. As such, neither electron excitation nor e-h pair production or carrier recombination occurs during STS measurement. What contribute to the STS-E_G are states occupied by the covalent bonding electrons and empty states that are strongly localized at the probed site. Events such as e-h interaction or kinetic

ATTENTION: The Singapore Copyright Act applies to the use of this document. Nanyang Technological University Library

energies of the mobile carriers do not come into play. Without triggering the dictating QC factors,[36] STS-E_G continues expanding upon the size being reduced. Figure 4.4 shows that the size-enlarged E_G of both Si nanorods[183] and Si nanodots follows closely the *BOLS* prediction in Equation 2.11 using the parameters in Table 4.3 without involving e-h interaction, e-p coupling, or QC. Consistency between the *BOLS* prediction and measurements evidences not only the essentiality of the *BOLS* premise but also the significance of atomic coordination imperfection to the performance of a surface and a nanosolid.

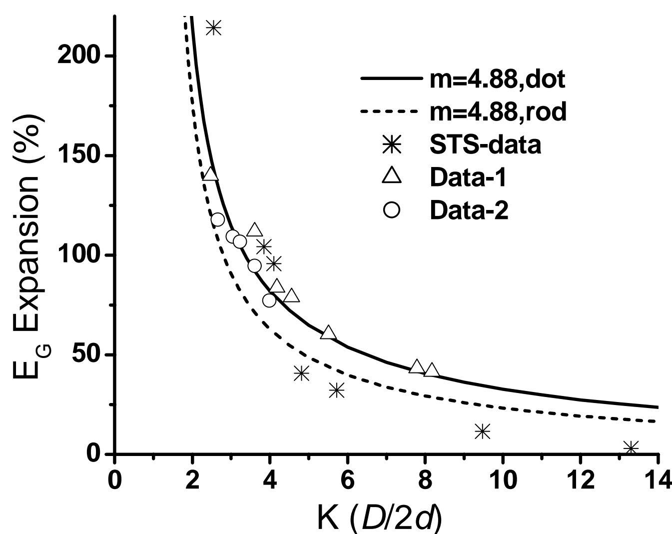

Figure 4.4 Comparison between predictions (solid line, Equation 2.11) and measurements on the size dependence of the E_G measured using STS[183] and optical method, Data –1[100] ($E_G = E_{PA} - W$), Data –2 (current work, $E_G = (E_{PL} + E_{PA})/2$). (from Ref. 101)

Table 4.3 Parameters for the E_G expansion of PS

	E_G (bulk) (eV)	d (nm)	z_1[72]	z_2 ($K > 2$)	Z_3 ($K > 3$)	m
PS	1.12	0.263	2~4	6	12	4.88

ATTENTION: The Singapore Copyright Act applies to the use of this document. Nanyang Technological University Library

4.3.2 Core Level Shift

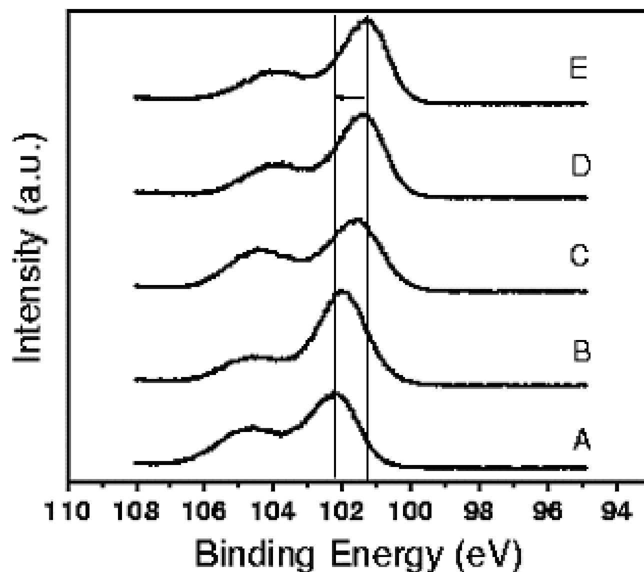

Figure 4.5 XPS profiles showing the size dependence of the 2*p* level shift of nanosolid Si. (from Ref. 184)

Figure 4.5 shows the XPS Si-2*p* profiles of the fresh PS samples. The size-dependent peak energy was then linearized with the least-root-mean-square optimization method to find the slope and intercept at the vertical axis ($1/D \rightarrow 0$ in Figure 4.6 (a)). Thus, the following line can represent the experimental results (ν = 2*p*):

$$E_{2p}(D) = E_{2p}(\infty) + b/D = 99.06 + 4.52/D \quad (4.1)$$

This D^{-1} trend agrees with those reported by others[102-105] obtained from other materials despite the slope that changes from situation to situation. The intercept $E_{2p}(\infty)$ corresponds to the bulk $E_{2p}(\infty)$ position –99.2 eV and therefore a 0.14 eV (= 99.2 – 99.06) shift is necessary for the $E_{2p}(1)$ and $E_{2p}(\infty)$. The slight shift is due to the surface electrostatic charge effect during the measurement. However, the shift has no effect on the crystal binding intensity, $\Delta E_{2p}(\infty) = E_{2p}(\infty) - E_{2p}(1)$.

ATTENTION: The Singapore Copyright Act applies to the use of this document. Nanyang Technological University Library

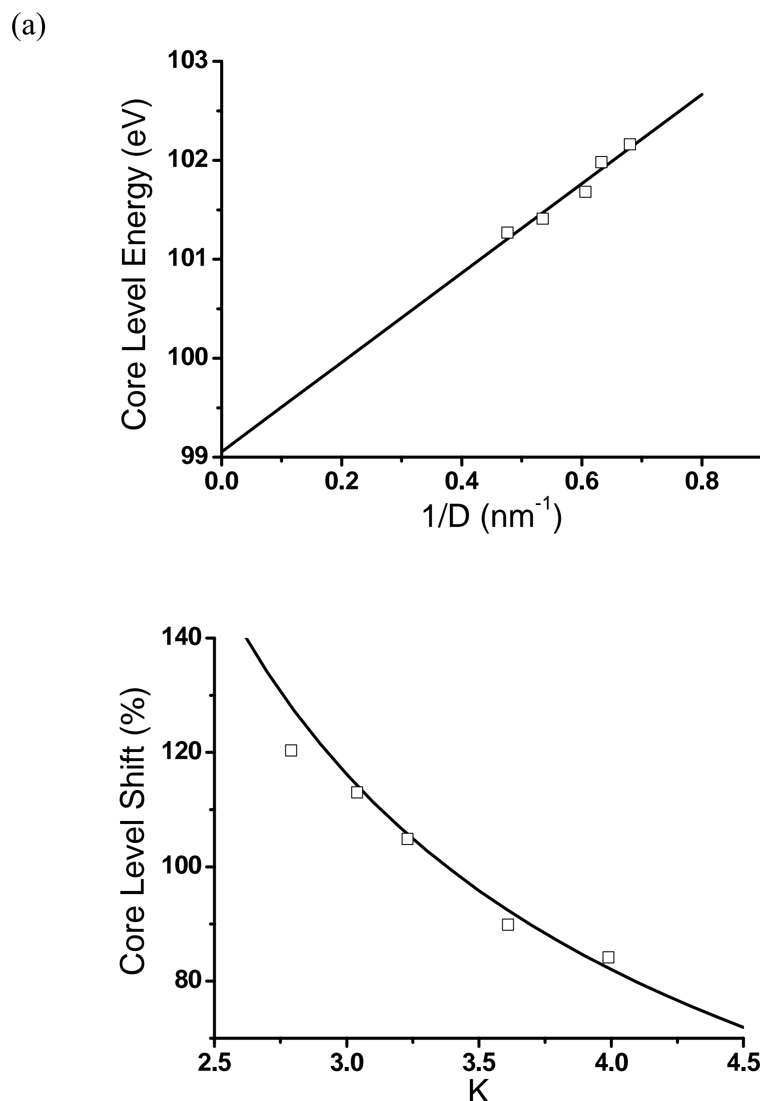

Figure 4.6 (a) Least-root-mean-square linearization of the energy shift gives $E_{2p}(D)$ = 99.06 + 4.52/D ± 0.04. The slope is used to derive the atomic trapping and crystal binding of the bulk solid; the intercept is used to calibrate the equipment due to the surface electrostatic charge effect. Panel (b) shows the agreement between prediction (solid line) and the measured size dependence of the Si-2p core level shift, where $K = D/2d$. The calculation is based on Equation 2.16 using the parameters given in Table 4.4. (from Ref. 184)

Matching the prediction in Equation 2.16 with the experimental results represented by Equation 4.1, one can find that the crystal binding intensity:

$$E_{2p}(\infty) - E_{2p}(1) = \frac{4.52}{D\delta_{surf}} \qquad (4.2)$$

ATTENTION: The Singapore Copyright Act applies to the use of this document. Nanyang Technological University Library

is readily available now because $\delta_{surf} \propto D^{-1}$ and $D\delta_{surf}$ is a constant provided with the known m = 4.88 for the effect of crystal binding on the E_G. As listed in Table 4.4, the atomic trapping energy of the 2p electron of an isolated Si atom $E_{2p}(1)$ is found to be –96.74 eV and the bulk crystal binding intensity $\Delta E_{2p}(\infty)$ to be –2.46 eV. Consistency between the predicted and the measured core-level shift is given in Figure 4.6 (b), which ensures the reliability of the data obtained and evidence that the *BOLS* correlation describes adequately the true situation. Accuracy of the determination is subject strictly to the precision of XPS measurement.

Table 4.4 Measured E_{2p} with different particle size D and the derived information on atomic $E_{2p}(1)$ and bulk shift $\Delta E_{2p}(\infty)$ of nanosolid Si.

Sample	D (nm)	$E_{2p}(D)$ (eV)	$\Delta E_{2p}(\infty)$ (eV)	$E_{2p}(1)$ (eV)
A	1.4	-102.16		
B	1.6	-101.98		
C	1.7	-101.68		
D	1.9	-101.41		
E	2.1	-101.27		
Bulk	∞	-99.2	-2.46	-96.74

4.3.3 Dielectric suppression

Conventionally, the dielectric response of PS is described by the effective medium approximations[134,185] that simply average the dielectric contribution from the air pores and the backbones of the silicon (nano-Si). The dielectrics $\varepsilon_{nano\text{-}Si}$ of a

ATTENTION: The Singapore Copyright Act applies to the use of this document. Nanyang Technological University Library

nano-Si is often presumed to take the bulk constant in the simple effective medium function such as Looygenga formula:[186]

$$\varepsilon_{eff}^{1/3} = (1-p)\varepsilon_{nano-Si}^{1/3} + p\varepsilon_{air}^{1/3}, \tag{4.3}$$

where ε_{air} (≈ 1) is the dielectric constant of air and p is the porosity PS. However, this approach ignores the fact that the dielectric constant of a nano-Si is not only lower than the bulk value but also size dependent.[71] The contribution from the lower–coordinated surface atoms cannot be neglected in accounting for the dielectric performance of PS.[187] Therefore, the effective medium methods need to be modified by taking account of the size dependent dielectric performance of the nano-Si backbones, $\varepsilon_{nano-Si}$.

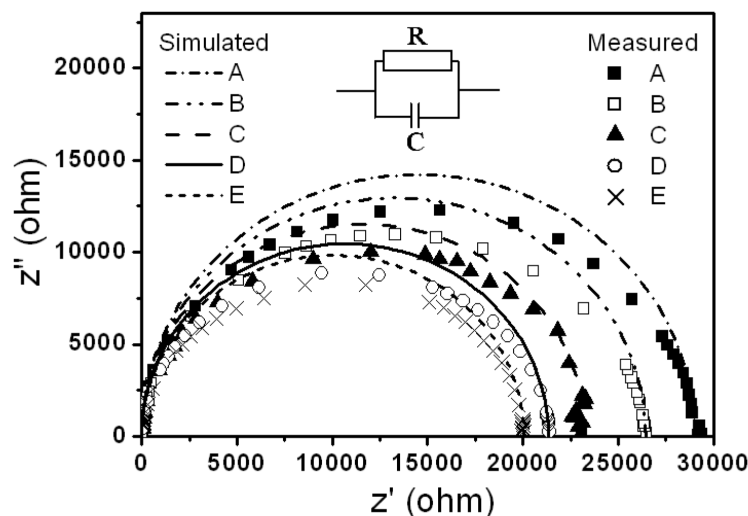

Figure 4.7 Size dependent Cole–Cole plots of PS. The dots represent the data measured by the *RCL* meter at RT and the lines correspond to simulation using the *RC* parallel circuit model (inset) for typical dielectric materials.

ATTENTION: The Singapore Copyright Act applies to the use of this document. Nanyang Technological University Library

We discriminate the dielectric contribution of the nanosoild Si backbone from the measured effective ε_{eff} of PS by matching the prediction with the measured impedance. The impedance behavior of PS samples can be described by Debye's expression of parallel *RC* circuit[188] with elements that correspond to the dielectric behavior of the bulk grain, as shown in the inset of Figure 4.7.

Table 4.5 Summary of the *D*-dependent $\varepsilon_{nano\text{-}Si}$ derived from the measured E_{PL}, porosity and ε_{eff} of PS.

Sample	E_{PL} (eV)	D (nm)	Porosity (%)	ε_{eff}	$\varepsilon_{nano\text{-}Si}$
A	2.08	1.7	85	1.43	6.27
B	1.82	2.0	76	1.84	7.29
C	1.81	2.1	71	2.11	7.7
D	1.79	2.2	68	2.28	7.86
E	1.76	2.4	66	2.45	8.29

The complex impedance *Z** measured by the *RCL* meter can be expressed as

$$\begin{cases} Z^* = Z' - jZ'', \\ Z' = \dfrac{R}{1+\omega^2 R^2 C^2}, \\ Z'' = \dfrac{\omega R^2 C}{1+\omega^2 R^2 C^2}, \end{cases} \tag{4.4}$$

where ω is the angular frequency. Here the bulk–grain resistance *R* represents ionic or electronic conduction mechanisms, while the capacitance *C* represents the polarizability of PS. The complex impedance response commonly exhibits a semicircular form in the measured Cole–Cole plot[189] as shown in Figure 4.7 A–E

ATTENTION: The Singapore Copyright Act applies to the use of this document. Nanyang Technological University Library

denote the responses of different samples (Table 4.5) measured at RT. The complex impedance plots show only one depressed single semicircular arc, indicating that only one primary mechanism, corresponding to the bulk grain behavior, dominates at RT for polarization within the PS film. The second intercept on the real axis made by the semicircle corresponds to the resistance in the bulk grain. As can be seen, the intercept of the semicircles shifts towards the origin as the nanosolid size increases, indicating a reduction of the bulk grain resistance.

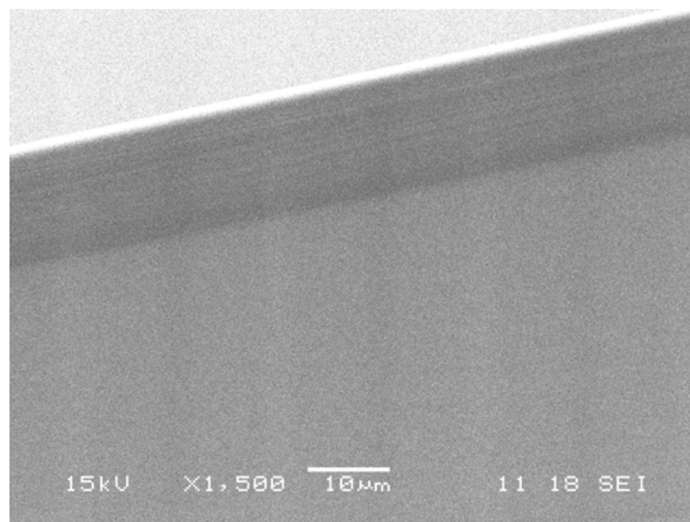

Figure 4.8 Cross section view of PS sample.

The way[190] by which to extract the capacitance and dielectric constant is using the equation: $Z''=1/(\omega C)$ in high-frequency range (10^5–10^6 Hz). The bulk grain capacitance C of the sample is given by the slope of the straight line determined by the variation of Z'' as a function of $1/\omega$. Then, the effective dielectric constant ε_{eff} of the porous structure is calculated based on the equation: $\varepsilon_{eff} = Cl/(\varepsilon_0 S)$. ε_0 is the dielectric constant of a vacuum, l is the thickness of the sample (10–15 μm) that

ATTENTION: The Singapore Copyright Act applies to the use of this document. Nanyang Technological University Library

was measured upon cross section of the sample by a scanning electron microscope, as shown in Figure 4.8; S is the area of silver electrode (250 mm^2).

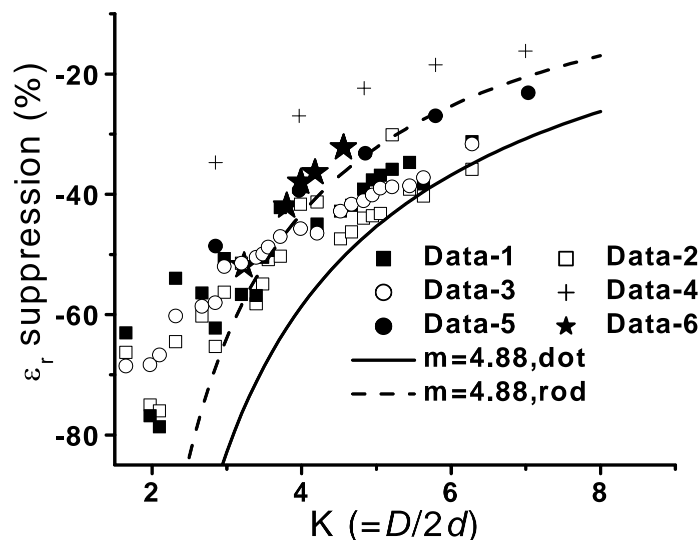

Figure 4.9 Comparison of the predictions on the size–dependent dielectric constants of silicon nanosolids with the sophisticated calculation and measurement results. Calculated Data–1, 2, 3 are after Ref. 191. Calculated Data–4 and 5 are after Ref. 109. Data–6 is the current experimental results. d is the bond length of bulk silicon. K is the number of atoms arranged along the radius of a spherical dot or a rod.

With the measured ε_{eff}, we can calculate the $\varepsilon_{nano\text{-}Si}$ based on the Looygenga formula (Equation 4.3). The measured ε_{eff}, and derived $\varepsilon_{nano\text{-}Si}$ for different sizes are listed in Table 4.5. It is not surprising that $\varepsilon_{nano\text{-}Si}$ is much higher than the ε_{eff} due to the voids ($\varepsilon_{air} \approx 1$) involvement. The $\varepsilon_{nano\text{-}Si}$ decreases with solid size due to the atomic *CN*–imperfection and hence it is not appropriate to simply take bulk value as $\varepsilon_{nano\text{-}Si}$ in conventional calculations. Figure 4.9 compares the $\varepsilon_{nano\text{-}Si}$ derived herewith using aforementioned approach with the *BOLS* predicted size–dependence and other sophisticated calculations of nanosolid Si. Consistency between *BOLS* predictions and the measured results evidences that the *BOLS*

ATTENTION: The Singapore Copyright Act applies to the use of this document. Nanyang Technological University Library

correlation describes adequately the true situation in which the $\varepsilon_{nano\text{-}Si}$ suppression is dictated by atomic *CN* imperfection that provides impact on the interatomic interaction and e-p coupling.

4.3.4 Raman shift

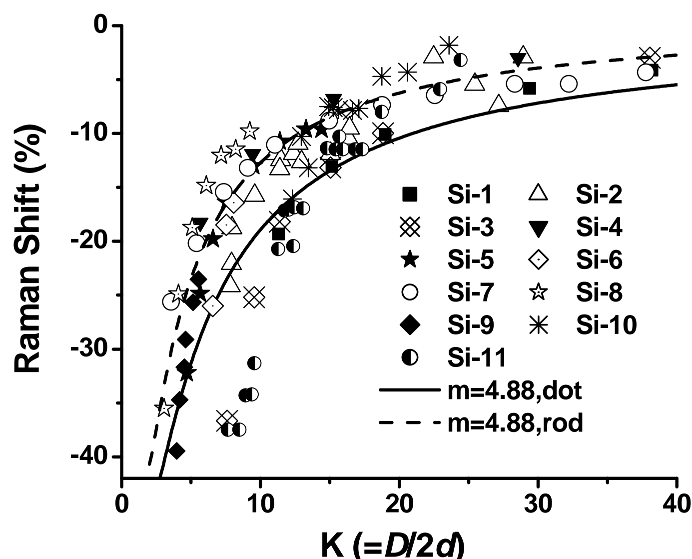

Figure 4.10 Comparison of the predictions with observations on the size-dependent TO shift of the nanosolid silicon. Theoretical results: Si-1 calculated using correlation length model;[192] Si-3 (dot) and Si-4 (rod) calculated using the bulk dispersion relation of phonons;[193] Si-5 calculated from the lattice-dynamic matrix;[130] Si-7 calculated using phonon confinement model [194] and Si-8 (rod), Si-9 (dot), calculated using bond polarizability model.[120] Measurements: Si-2;[195] Si-6;[196] Si-10 and Si-11.[122] *d* is the bond length of bulk silicon. *K* is the number of atoms arranged along the radius of spherical dot or a rod. (from Ref. 133)

Similar to Si-2*p* core level shift, the Raman TO frequency also depends linearly on the inverse *D*. Incorporating the *BOLS* prediction with the linearization of measurement, we have the following relations

ATTENTION: The Singapore Copyright Act applies to the use of this document. Nanyang Technological University Library

$$\Delta\omega(D) = \begin{cases} \dfrac{-10.63}{D} & (Measurement), \\ \delta_p\left(\omega(\infty) - \omega(1)\right) & (Theory). \end{cases} \quad (4.5)$$

Hence, the frequency shift from the dimer bond vibration to the bulk value, $\omega(\infty) - \omega(1) \equiv -10.63/(\delta_p D)$, is a constant as $\delta_p \propto D^{-1}$. Excitingly, this allows us to determine the vibrational frequency of a Si–Si dimer bond $\omega(1)$ = 502.3 cm^{-1} and the bulk shift of 17.7 cm^{-1}, which is beyond the scope of currently available approaches. Figure 4.10 shows the match between the *BOLS* predictions with the theoretically calculated and the experimentally measured TO red-shift of nanosolid silicon.

According to Einstein's relation: $z\mu_{Si}(c\omega)^2(x/z)^2/2 = k_B T$ (k_B is the Boltzmann constant and T is the absolute temperature), the vibrational amplitude of an atom is $x \propto z^{1/2}\omega^{-1}$. The reduced magnitude and frequency of an atom in the surface at RT are:

$$\begin{aligned} \frac{x_1}{x_b} &= (z_1/z_b)^{1/2}\,\omega_b/\omega_1 = (z_b/z_1)^{1/2} c_1^{\left(\frac{m}{2}+1\right)} \\ &= \begin{cases} \sqrt{3}\times 0.88^{3.44} = 1.09 & (Si, m = 4.88) \\ \sqrt{3}\times 0.88^{1.5} = 1.43 & (metal, m = 1) \end{cases} \end{aligned} \quad (4.6)$$

As the z_1 change slightly with the curvature of the surface, z_1=4(1-0.75/K).[72] The vibrational amplitude of an atom at the surface stays almost constant at $K > 3$. This confirms for the first time the assumption made by Shi[88] and Jiang *et al.*[87] that the vibrational amplitude of a surface atom is higher than the bulk value and keeps constant at all particle sizes. It can also be estimated that the frequency of the

ATTENTION: The Singapore Copyright Act applies to the use of this document. Nanyang Technological University Library

surface atom (with $z = 4$) is around 511 cm^{-1}, which is between that of the dimer (502.3 cm^{-1}) and the bulk (520.0 cm^{-1}).

4.4 Summary

BOLS correlation premise has been further evidenced by the consistency between predictions and experimental data on size dependent E_G expansion, E_{2p} shift, $\varepsilon_{nano\text{-}Si}$ suppression, and ω red-shift. This premise has enabled E_G expansion, E_{2p} shift, $\varepsilon_{nano\text{-}Si}$ suppression, and ω red-shift upon nanosolid Si formation to be consistently decoded and understood in terms of surface *CN* imperfection and its effect on the crystal binding density and the e-p coupling. Decoding the E_{2p} and ω shifts leads to quantitative information about the atomic trapping energy of the 2*p* electrons (–96.74 eV) of an isolated Si atom and the vibration frequency of a Si–Si dimer bond (502.3 cm^{-1}) at RT.

ATTENTION: The Singapore Copyright Act applies to the use of this document. Nanyang Technological University Library

Chapter 5 Surface Passivation

5.1 Surface Fluorination

5.1.1 Introduction

PS consists of a nanocrystalline skeleton immersed in a network of pores and characterized by a very large internal surface area (of the order of 500 m^2/cm^3). This internal surface is passivated by hydrogen but remains highly chemically reactive, which is one of the essential features of this complex material. However, the role of the surface played in the optical and dielectric properties has been remained a key issue that is yet poorly known.[153] In previous chapter, size dependent PL and PA blue-shift, E_G expansion, core level shift, and dielectric suppression has been well explained based on *BOLS* correlation model. However, it has been found that surface passivition by electronegative additives can also shift the PL wavelength[197] and suppress the dielectric constant of PS.[198,199] For example, hydride passivation could tune the PL wavelength towards blue side, while thermal oxidation results in PL emission which is invariably in the deep red spectral range. The latter phenomenon is not satisfactorily understood at present, but consideration of various factors may provide an explanation. It has been proposed that the effect of particle size and the effect of surface passivation enhance each other on the properties of nanometric semiconductors.[200,201,151 ,79]

ATTENTION: The Singapore Copyright Act applies to the use of this document. Nanyang Technological University Library

5.1.2 Experimental Details

The PS samples were prepared according to the fabrication procedures introduced in section 3.2.2 with a applied current density of 50 mA/cm^2 for 15 min. AFM measurements have showed that the average particle sizes of all the samples are in the same range; and hence the size variation effect is neglected in the experiments. Surface fluorination was performed with CF_4 plasma at RT for 2 min. by PECVD. PS samples were placed on the cathode electrode. CF_4 gas was introduced with a flow rate of 10 standard cubic centimeter per minute (sccm), and the chamber pressure was kept at 25 mTorr during the process. By varying the radio frequency (rf) power the samples were obtained with different fluorination content. No obvious particle-size reduction upon fluorination can be resolved using AFM. Usually, F-plasma etching of Si or SiO_2 surface is carried out by bombarding the surface with 350 W plasma for several hours.

5.1.3 Results and Discussion

Table 5.1. Summary of the fluorination process parameters and corresponding results

Sample	rf Power (W)	F/Si *
F	0	~ 0
G	80	0.21
H	100	0.27
I	120	0.29
J	140	0.42

* Area ratio from XPS spectra

ATTENTION: The Singapore Copyright Act applies to the use of this document. Nanyang Technological University Library

The process parameters of fluorination and the corresponding results are listed in Table 5.1, where the F/Si ratios are calculated from the area ratio of the corresponding peaks in the XPS spectra (Figure 5.1). From Table 5.1, it can be seen that with the increase of the rf power, the fluorination degree increases accordingly due to the higher energy and density of the plasma arriving at the PS surface.

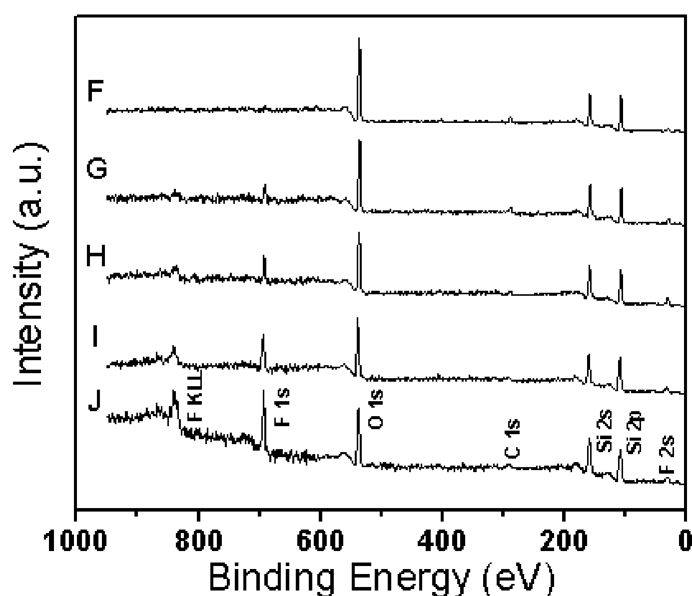

Figure 5.1 XPS spectra of the fluorinated and as-grown PS samples showing the existence of fluorine in fluorinated samples. Processing conditions are given in Table 5.1. The existence of a little fluorine in the as-grown sample results from HF acid remnants inside voids after preparation. (from Ref. 202)

Figure 5.1 compares the XPS spectra of fluorinated and as-grown PS samples. It can be seen that besides Si and F, O and C also exist on the surface. The existence of a little fluorine in the as-grown sample is due to HF acid remnants inside voids after preparation because only HF and SiF_6^{2-} were found using ^{19}F nuclear magnetic resonance.[203,204] Upon fluorination, surface fluorides exist in the

ATTENTION: The Singapore Copyright Act applies to the use of this document. Nanyang Technological University Library

form of SiF_2 species,[205,206] which modify the chemical structure of the PS surface through bond reforming from the Si–H bond. The source of carbon is not ethanol because the carbon amount is similar to that in samples anodized in water–HF solutions.[207] The carbon should come from hydrocarbon molecules in the ambient and often in the residual gas in analysis chambers used for XPS.[139] Oxygen exists in the form of Si–O–Si and O_x–Si–H groups on the PS surface, which is confirmed by FTIR results in Figure 5.2, and is normally adsorbed in a few minutes after drying in ambient. Nevertheless, coexistence of these elements may contribute to the F surface passivation. As noted in Ref. 126 that reaction with C, N, O, and F has the similar effect on the binding energy enhancement due to the charge transportation. The extent of contribution may be different due to the difference of atomic valence and the richness of the corresponding element. From this perspective, we may treat the F-plasma passivation as a resultant effect of these elements as it is not realistic to distinguish the contribution from the individual element.

Figure 5.2 displays the FTIR spectra in fluorinated and as-grown PS samples. Compared with the as-grown sample, there are two obvious changes for fluorinated ones: with increasing rf power, the spectral line intensities in the absorption peak at 667 cm^{-1} (Si–H deformation mode) decays while the absorption peaks at 977 and 940 cm^{-1} (Si–F stretching modes) become stronger. This not only proves that the fluorine exists in the form of an Si–F bond on the surface but also means that more Si–H bonds (667 cm^{-1}) are substituted by the Si–F bonds (977 and 940 cm^{-1}) upon increasing the extent of fluorination.

ATTENTION: The Singapore Copyright Act applies to the use of this document. Nanyang Technological University Library

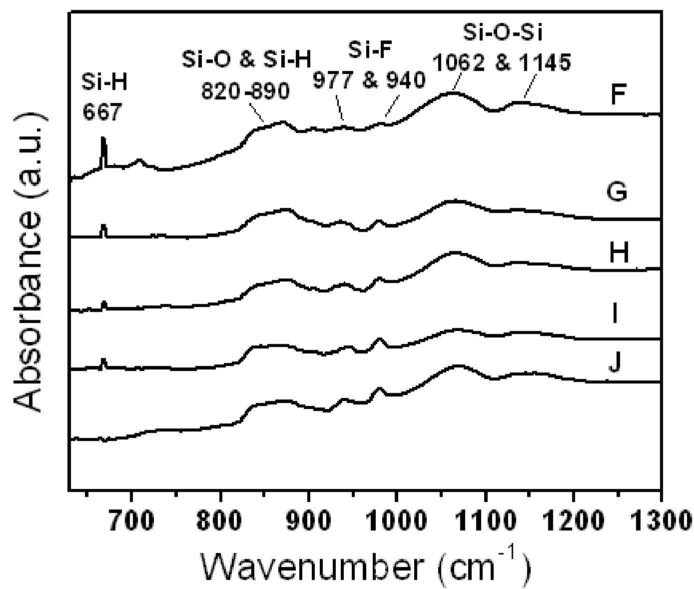

Figure 5.2 Fluorination effect on the FTIR spectra of PS. The absorption peaks at 667 cm^{-1} and 977/940 cm^{-1}correspond to the Si–H deformation mode and the Si–F stretching mode, respectively. With the increase of rf power upon the fluorination of PS, the absorption peak at 667 cm^{-1} decays while the absorption peaks at 977 and 940 cm^{-1} become stronger. (from Ref. 202)

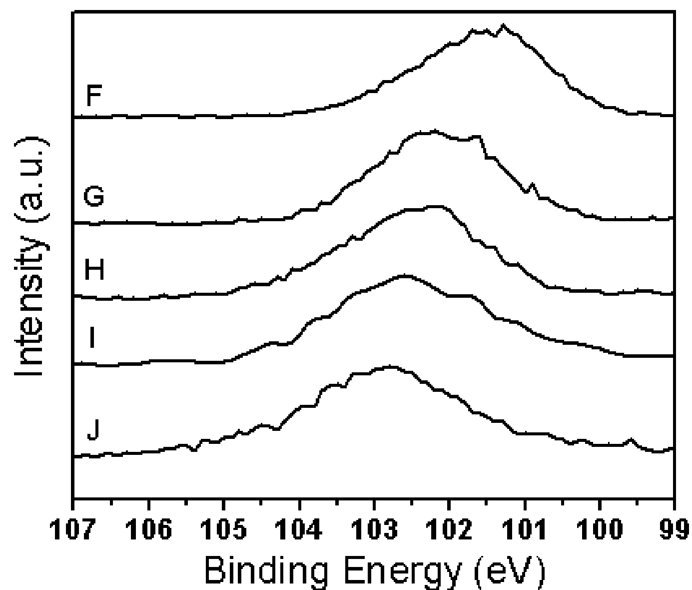

Figure 5.3 Fluorination effect on Si 2*p* XPS spectra of the PS. There is obvious shift from 101.7 eV for sample F as grown to 102.8 eV for sample J highly fluorinated. (from Ref. 202)

ATTENTION: The Singapore Copyright Act applies to the use of this document. Nanyang Technological University Library

The Si 2*p* XPS spectra in Figure 5.3 show obvious shift from 101.7 eV for sample F to 102.8 eV for sample J and such a shift is proportional to the fluorination extent. Clearly, the crystal field enhancement due to bond nature alteration upon fluorination contributes to the core level shift and E_G expansion as well.[82,126] A chemical reaction such as fluorination modifies the crystal field and redistributes the valence charge. Fluorination substitutes the stronger Si–F bonds (bond energy: 565.2 KJ/mol) for the weaker Si–H bonds (318.2 KJ/mol). Electron repopulation from Si to F lowers the energy of the occupied valence band and also weakens the screening of the crystal field to electrons in the inner shells.

Compared with the as-grown sample, the passivation lowers the PL intensity and shifts the PL peak to blue side as can be seen in Figure 5.4 (a). The PL intensity relates to the irradiative recombination centers such as dangling bonds upon fluorination that lowers the quantum efficiency of radiative carrier combination. The PL blue-shift results from both the e-p coupling and E_G expansion that changes with the crystal field enhancement due to bond nature alteration and valence charge repopulation that leaves holes behind the top of the valence band.[208] The reflection spectra in Figure 5.4(b) show that the reflectivity varies with the extent of fluorination in the range of 200–900 nm, which is related to the change of dimension and geometry of columns and voids on the PS surface. Figure 5.4(c) shows the spectral dependence of the absorption coefficient of PS samples. As observed, the values of absorption coefficient are strongly dependent on the fluorination, especially in the range of higher photon energy. The correlation

ATTENTION: The Singapore Copyright Act applies to the use of this document. Nanyang Technological University Library

between the E_G and the rf power shown in Figure 5.5 indicates that the E_G widens with the increase of rf power.

(a)

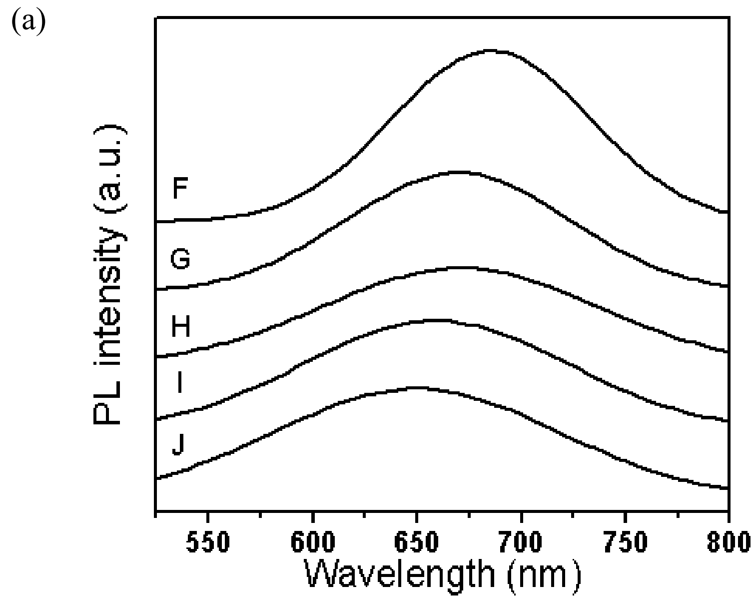

(b)

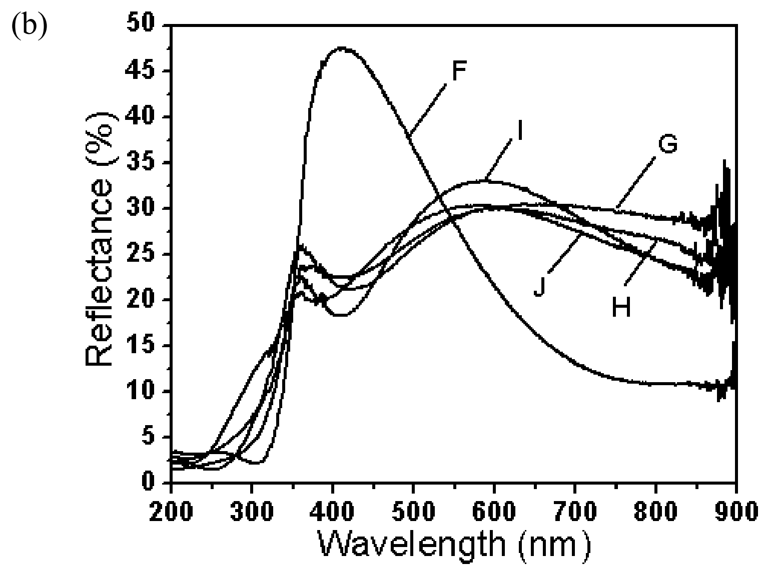

ATTENTION: The Singapore Copyright Act applies to the use of this document. Nanyang Technological University Library

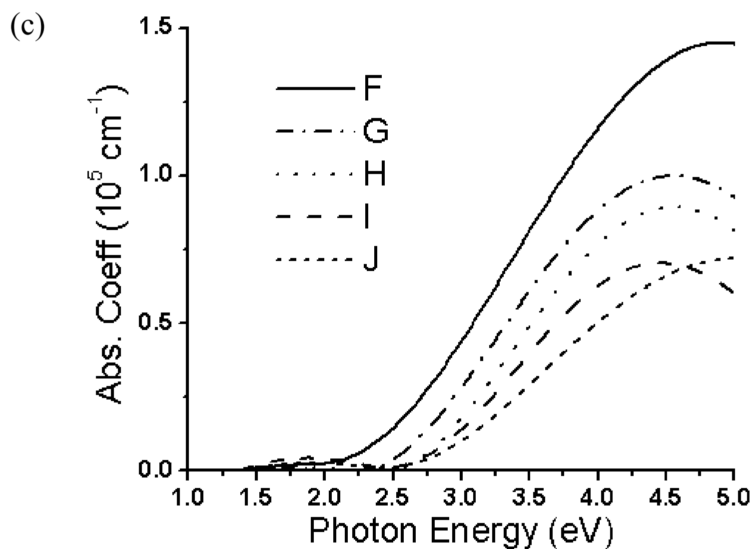

Figure 5.4 (a) RT PL spectra, (b) Reflection spectra, and (c) Absorption spectra of the fluorinated and as-grown PS. (from Ref. 202)

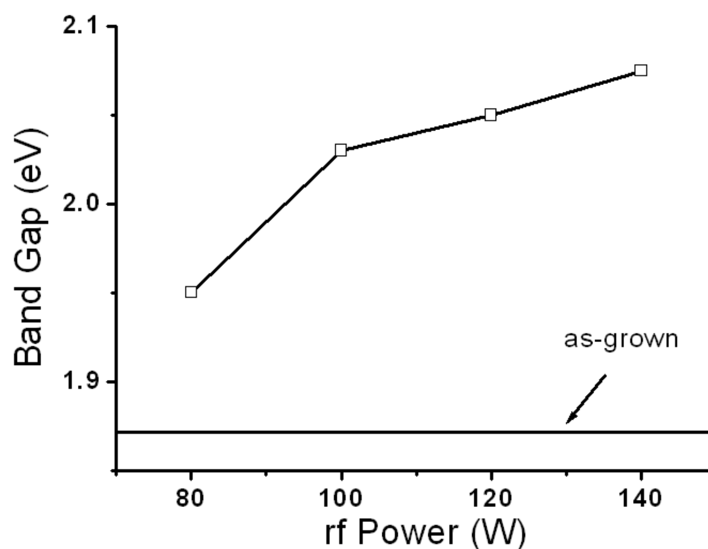

Figure 5.5 Comparison of the E_G of the fluorinated PS with the as-grown PS. The rf power is used to control the fluorine contents in the fluorinated samples. (from Ref. 202)

ATTENTION: The Singapore Copyright Act applies to the use of this document. Nanyang Technological University Library

5.1.4 Summary

It has been found that the surface fluorination has an effect similar to the particle size reduction on the electronic and optical properties of PS. The E_G expands from 1.87 eV (the as-grown value) to 2.08 eV and the Si 2*p* core level shifts from 101.7 eV (the as-grown value) to 102.8 eV upon fluorination. These changes are suggested to arise from the crystal field enhancement due to the bond nature alteration at the surface and the valence charge transportation. Importantly, surface fluorination could provide a practical and compatible means to tune the optical and electronic behavior of the nanostructured silicon.

5.2 Surface Fluorination Enhanced Size Dependency

5.2.1 Introduction

As discussed previously, structural miniaturization of solid silicon results in the blue-shift in PL,[209,74] PA,[65] and Stokes shift.[101] The size reduction also shifts the core level energy up[184,106] and lowers the dielectric constant[71,111] of the solid silicon. Further observations have found that chemical passivation by surface fluorination that alternates the nature of the surface bond enhance the size effect. The measured quantities such as E_G expansion, Stokes shift, and Si-2*p* core level shift will change further, as charge transport and bond nature alteration are involved in the reaction.[126] Practice[200,201,151] revealed that the effect of crystallite size (*D*) reduction and the effect of surface passivation enhance each other on the properties of nanometric semiconductors by perturbing the overall potential in the

ATTENTION: The Singapore Copyright Act applies to the use of this document. Nanyang Technological University Library

Hamiltonian of an extended solid. As a result, an effective way to discriminate the contribution of surface-bond relaxation from the contribution of surface-bond nature alteration to the crystal binding and e-p coupling in PS is necessary.

5.2.2 Experimental Details

We prepared the PS samples and measured the size dependence of the PL, PA, and E_{2p} peak energies before and after fluorination. Surface fluorination was performed on the PS samples with CF_4 plasma at RT by rf-PECVD. CF_4 gas was introduced with a flow rate of 10 sccm and the chamber pressure was kept at 25 mTorr. A rf power of 100 W was applied for 2 min. The F/Si ratio is about 0.3 for all the fluorinated samples. No apparent particle-size reduction upon fluorination can be resolved using AFM.

5.2.3 Results and discussion

Figure 5.6 shows RT PL spectra of as-grown (refer to Figure 4.1) and fluorinated PS samples. Compared with the as-grown samples, the passivated ones exhibit a blue-shift in the PL, evidencing an enhancement of crystal field due to bond nature alternation and screen weakening as well as valence charge repopulation that leaves holes behind the top of the valence band.[208] Figures 5.7 (a) and (b) show RT reflection and absorption spectra of PS samples as-grown (inset, refer to Figure 4.3) and fluorinated, respectively. As observed, the values of absorption coefficient are strongly dependent on the size and surface fluorination, especially in the range of higher photon energy.

ATTENTION: The Singapore Copyright Act applies to the use of this document. Nanyang Technological University Library

Table 5.2 Measured E_{PL}, E_{PA} and E_{2p} of F-passivated PS with particle size D

Sample	D (nm)	E_{PL} (eV)	E_{PA} (eV)	E_G (eV)	$E_{2p}(D)$ (eV)
A	1.4	2.28	3.15	2.72	-103.31
B	1.6	2.18	3.01	2.60	-103.06
C	1.7	2.14	2.92	2.53	-102.73
D	1.9	2.01	2.74	2.38	-102.31
E	2.1	1.89	2.43	2.16	-101.17
Bulk	∞	1.12	1.12	1.12	-99.37

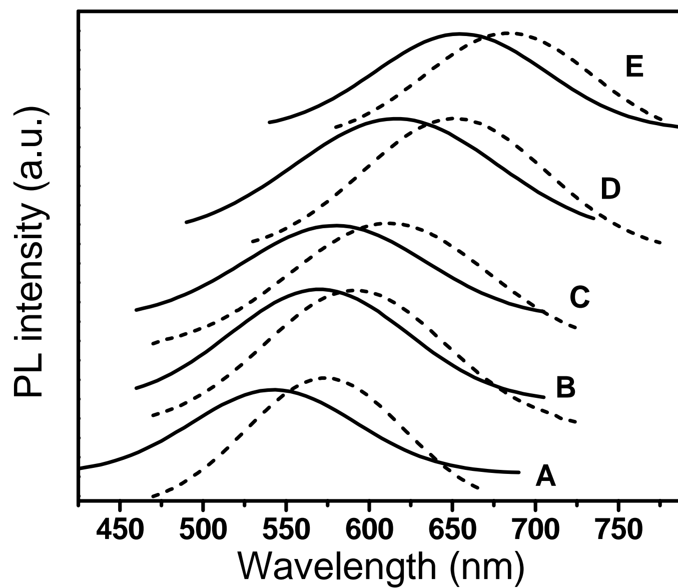

Figure 5.6 Size-dependent PL spectra of as-grown (dash line, refer to Figure 4.1) and fluorinated (solid line) p-Si samples. The data of sizes are given in Table 5.2. (from Ref. 210)

ATTENTION: The Singapore Copyright Act applies to the use of this document. Nanyang Technological University Library

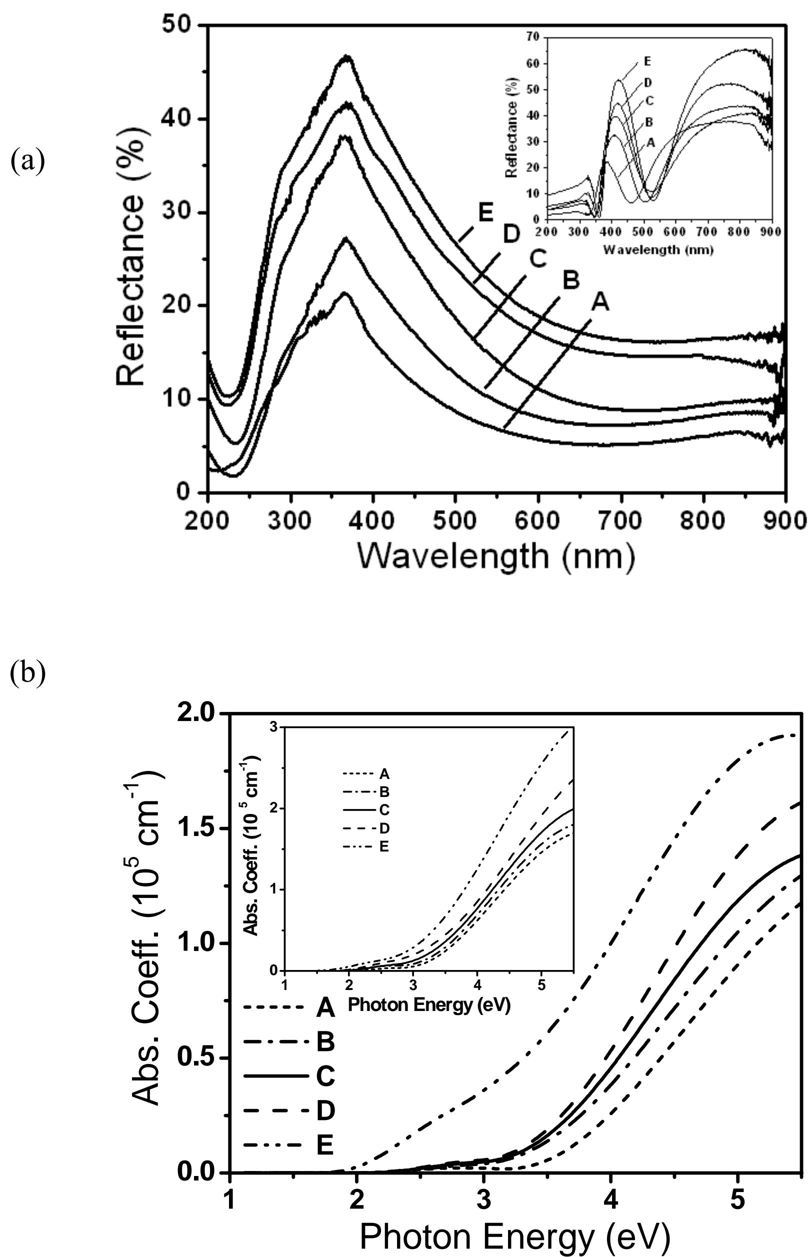

Figure 5.7 (a) RT reflection spectra of PS samples as-grown (inset, refer to Figure 4.3) and fluorinated; and, (b) RT absorption spectra of PS samples as-grown (inset, refer to Figure 4.3) and fluorinated, from which the PA energies are derived with the Tauc plot method. (from Ref. 210)

ATTENTION: The Singapore Copyright Act applies to the use of this document. Nanyang Technological University Library

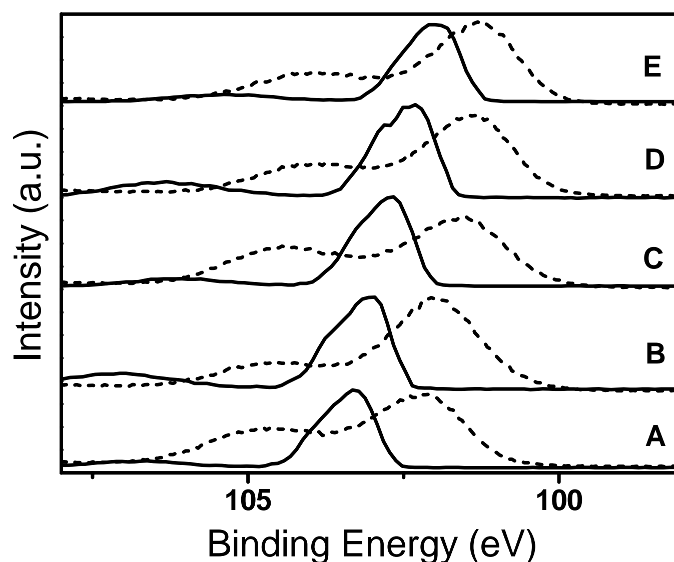

Figure 5.8 Size-dependent XPS Si-2p profiles of as-grown (dash line, refer to Figure 4.5) and fluorinated (solid line) p-Si samples. (from Ref. 210)

Figure 5.8 compares XPS Si-2*p* profiles of as-grown (refer to Figure 4.5) and fluorinated PS samples. There is an obvious Si-2*p* core level shift for PS samples before and after fluorination. The mechanism responsible for this core level shift is the same as the one for PL blue-shift upon fluorination.

Matching the prediction in Equation 2.14 with the experimental data on PA and PL peak energies, we can get the coefficient B = 1.04 and m = 5.32. The B and m values here are larger than the corresponding values (B = 0.91 and m = 4.88) for clean PS,[101] showing apparent enhancements of e-p interaction and crystal binding by surface fluorination. As discussed earlier, surface chemical reaction can contribute to the crystal binding intensity, transfer electrons from one specimen to another that causes the valence charge transportation from Si to F and thus enhance the crystal field. On the other hand, surface bond nature alteration also results in

ATTENTION: The Singapore Copyright Act applies to the use of this document. Nanyang Technological University Library

the higher vibration frequency[132,133] and larger vibration amplitude of surface atoms.[87,88] The e-p coupling will therefore be enhanced. Based on the *BOLS* coefficient m = 5.32 and the atomic trapping energy of the 2p electron of an isolated Si atom $E_{2p}(1)$= –96.74 eV,[184] the bulk crystal binding intensity $\Delta E_{2p,F}(\infty) = E_{2p,F}(\infty) - E_{2p}(1)$ is shifted from –2.46 to –2.63 eV. Consistency between the predicted and the experimental PA and PL blue-shift and the core-level shift (E_G expansion as well) after fluorination is given in Figure 5.9.

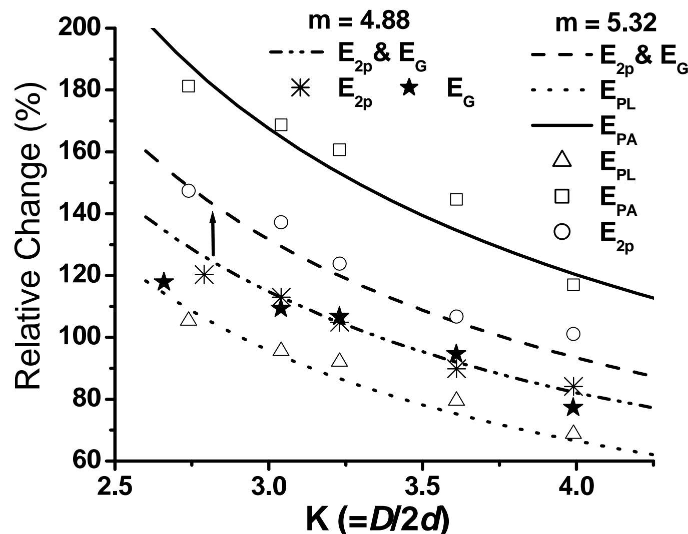

Figure 5.9 Comparison of the predicted with the measured PA and PL peak energies and the E_G and E_{2p} shift of clean (m = 4.88) and fluorinated (m = 5.32) PS. The E_{2p} and E_G data for the clean PS are from ref. 184 and 101, respectively. The arrow indicates the fluorination effect which displace the E_G and E_{2p} line up. (from Ref. 210)

Agreement of the predicted with the observed PA, PL, and E_{2p} shifts ensures the reliability of the data obtained and evidences the validity of the *BOLS* correlation for nanosolid. The theoretically predicted and the measured E_{2p} and E_G

ATTENTION: The Singapore Copyright Act applies to the use of this document. Nanyang Technological University Library

for clean (m = 4.88) PS are also compared in this figure. The effect of fluorination on the binding energy is thus easily distinguished as indicated by the vertical arrow.

5.2.4 Summary

Surface passivation by plasma fluorination with C and O contribution is found to further enhance both crystal binding intensity by surface bond nature alteration (from m = 4.88 to 5.32) that determines the E_G and core level shift and e-p coupling (from B = 0.91 to 1.04) that contributes to the energies of PL and PA of PS. The *BOLS* correlation has enables us to unify the observed blue-shift in the PL and PA, the energy shift of the Si-2*p* core level, as well as the dielectric suppression[71] to the effect of atomic *CN* imperfection of atoms near the edge of surface. The *BOLS* has also enabled us to discriminate the contribution from bond relaxation and bond nature alteration to both the crystal binding and e-p coupling that determine the unusual behavior of photons, phonons and electrons in PS. Practice should provide a helpful means for distinguishing the effect of surface passivation from the effect of size reduction on other size-dependent properties of other nanostructured materials.

5.3 Surface Oxidation Correlated Dielectrics

5.3.1 Introduction

PS is a special composite materials consisting of pores and silicon backbone networks, and has a broad range of applications due to its high surface area that

ATTENTION: The Singapore Copyright Act applies to the use of this document. Nanyang Technological University Library

determines the high tunability of the PS in many properties such as dielectric constant,[71] band gap,[74] and chemical reactivity.[211] Traditionally, Maxwell-Garnett[212] and Bruggeman[213] methods are often used to describe the dielectric performance of a two–phase composite semiconductor from known dielectric functions of the constituents for a particular topological structure. However, the Maxwell–Garnett formula is only a good approximation for high porosities with large separation between spherical silicon, which is however not suitable for a percolated system like PS. When the porosity is above 2/3, the Bruggeman formula switches off the percolation and describes a system of isolated particles. In reality, PS must be a self–supporting percolated network no matter how large the porosity is. Campos *et al*.[214] simulated the effective dielectric function using a mixture of the above two models based on the assumption that all the silicon inclusions are identically immersed in a homogeneous air matrix without interconnection between the crystallites. A real PS structure should include air pores and silicon networks and the passivated surfaces.[215,38] Modeling approaches often ignore the effect of surface/interface where chemisorption[126] and bond contraction[132] occur. The PS surface is often oxidized upon exposing to air and even in the electrolyte.[216] Investigations[217,218,134] suggested that natural oxide on the PS surface largely affects the refractive index of PS. Therefore, PS should be regarded as a system of three-component consisting of silicon, pores and silicon oxide interface.[219,220] Lugo *et al*.[220] described the effective dielectric properties of PS using volume averaging method and suggested the important role of surface coverage of SiO_2 in the effective dielectric response of PS. Astrova and Tolmachev[221] also studied the

ATTENTION: The Singapore Copyright Act applies to the use of this document. Nanyang Technological University Library

relationship between the refractive index, porosity and oxidation content in the framework of the three-component system. Both models are based on the Maxwell-Garnet and Bruggeman approximations that might be too ideal to be suitable for the dielectric properties of PS with complex three-component structure. Here we developed a method characterizing the dielectric properties of PS as a function of its porosity and the surface oxidation that are adjustable in experiment.

5.3.2 Model

The effective dielectric constant, ε_{eff} , describes the polarization response of matters to an externally applied electric field (e.g. that of an illuminating light beam in an optical experiment), and therefore, can be derived by the capacitance C_{eff} of parallel or serial capacitors: $\varepsilon_{eff} = C_{eff} l / A$. A and l are the area of the plate and distance between two plates of capacitor, respectively. The simplified parallel and serial models,[222,223] as illustrated in Figure 5.10 (a) can only predict two extreme values of ε_{eff} with very special geometrical structures of pore distribution. An ideal PS structure should be composed of identical air inclusions in a homogeneous silicon matrix (Figure 5.10 (b)), which is a mixture of serial and parallel capacitors.

ATTENTION: The Singapore Copyright Act applies to the use of this document. Nanyang Technological University Library

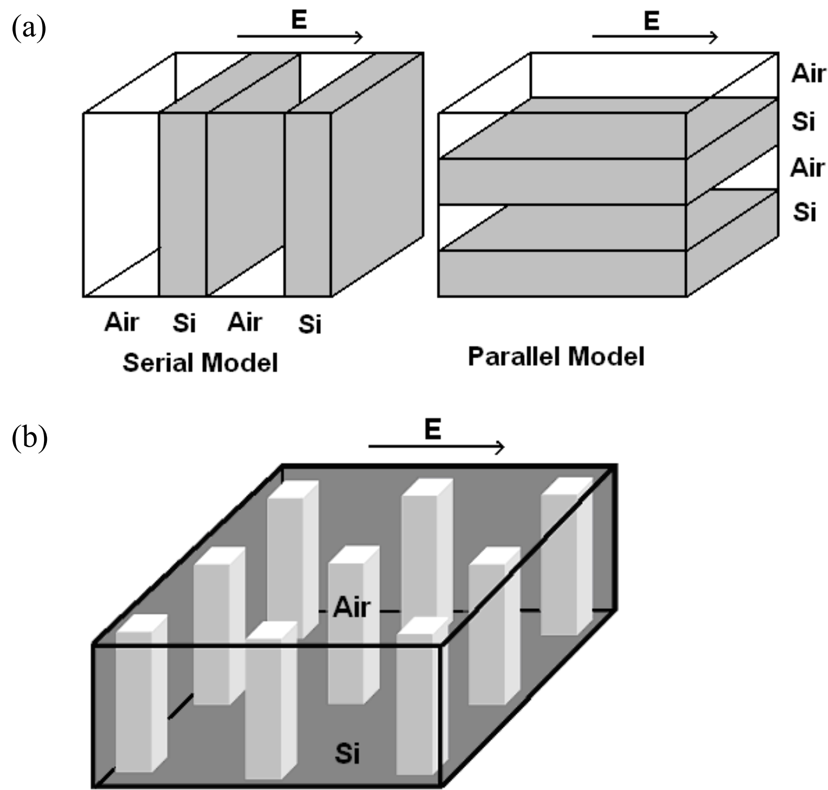

Figure 5.10 (a) Serial and parallel models[222,223] of PS consisting of void and silicon and (b) Serial-Parallel model assuming PS as a two-phase granulated compound medium with identical air inclusions placed uniformly inside a homogeneous silicon matrix.

Figure 5.11 (a) shows the top view of cuboids cell structure of PS based on the currently proposed Serial-Parallel model. This cell consists of five parallel plate capacitors: one C_1 for void; two C_2 and two C_3 for silicon. Hence the cell capacitance is given as:

$$\begin{cases} C_{eff} = \dfrac{1}{\dfrac{1}{2C_2 + C_1} + \dfrac{2}{C_3}}, \quad C_1 = \varepsilon_{air} \dfrac{N_1 d}{N_1} = \varepsilon_{air} d, \\ C_2 = \varepsilon_{Si} \dfrac{(N - N_1)d}{2N_1}, \qquad C_3 = \varepsilon_{Si} \dfrac{2Nd}{(N - N_1)} \end{cases} \tag{5.1}$$

d is the thickness of the PS sample. $\varepsilon_{air} \approx 1$, and $\varepsilon_{Si} = 11.3$ are used.[218,220]

ATTENTION: The Singapore Copyright Act applies to the use of this document. Nanyang Technological University Library

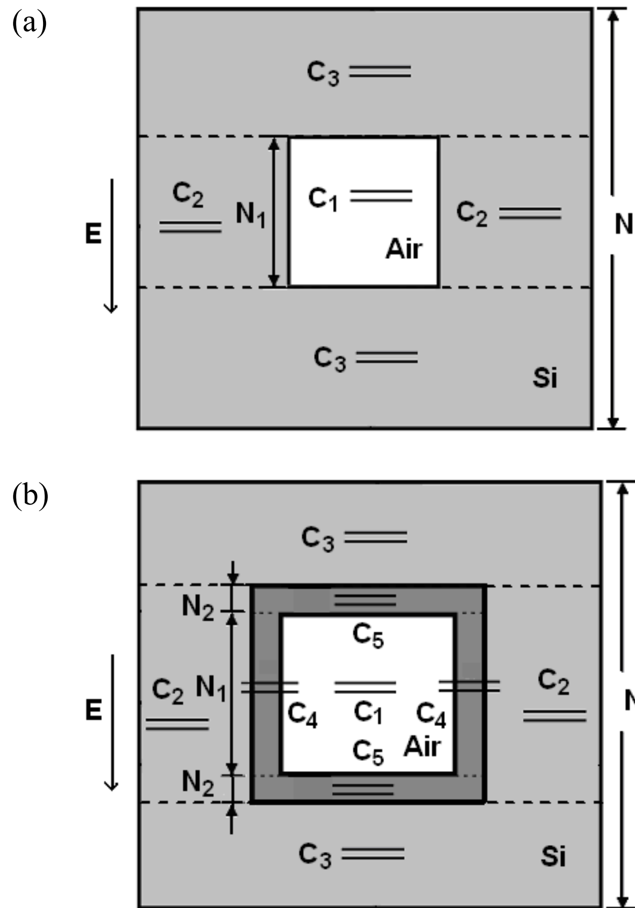

Figure 5.11 Top view of Serial-Parallel cell structure of (a) unpassivated and (b) surface oxidized PS.

Therefore, the effective dielectric constant ε_{eff} is calculated as,

$$\begin{aligned}\varepsilon_{eff} &= C_{eff}\frac{N}{Nd} = \frac{C_{eff}}{d} \\ &= \frac{\varepsilon_{Si}(\frac{N}{N_1}\varepsilon_{Si} + \frac{N}{N-N_1}\varepsilon_{air})}{(\frac{N}{N-N_1} + \frac{N-N_1}{N_1})\varepsilon_{Si} + \varepsilon_{air}} \\ &= \frac{\varepsilon_{Si}[(1-\sqrt{P})\varepsilon_{Si} + \sqrt{P}\varepsilon_{air}]}{(1-\sqrt{P}+P)\varepsilon_{Si} + (\sqrt{P}-P)\varepsilon_{air}}\end{aligned} \quad (5.2)$$

ATTENTION: The Singapore Copyright Act applies to the use of this document. Nanyang Technological University Library

The porosity $P = N_1^2 / N^2$ is defined as the volume ratio of void to the entire PS. From Equation 5.2, it can be seen that the effective dielectric constant of PS depends merely on its porosity if the surface effect such as oxidation is omitted. Similarly, the effective dielectric constant ε_{eff}^0 of porous silica ($\varepsilon_{SiO_2} = 3.9$) is:

$$\varepsilon_{eff}^0 = \frac{\varepsilon_{SiO_2}[(1-\sqrt{P})\varepsilon_{SiO_2} + \sqrt{P}\varepsilon_{air}]}{(1-\sqrt{P}+P)\varepsilon_{SiO_2} + (\sqrt{P}-P)\varepsilon_{air}} \tag{5.3}$$

In reality, a layer of silicon oxide is often formed at the surface. Taking account of the contribution from surface oxidation, as shown in Figure 5.11 (b), the cell contains nine parallel plate capacitors: one C_1 for void; two C_2 and two C_3 for silicon; two C_4 and two C_5 for silicon dioxide. Hence the capacitance becomes

$$\begin{cases} C_{eff} = \dfrac{1}{\dfrac{1}{\dfrac{1}{\dfrac{1}{2C_4 + C_1} + \dfrac{2}{C_5}} + 2C_2} + \dfrac{2}{C_3}}, & C_1 = \varepsilon_{air}\dfrac{N_1 d}{N_1} = \varepsilon_{air} d, \\ C_2 = \varepsilon_{Si}\dfrac{(N - N_1 - 2N_2)d}{2(N_1 + 2N_2)}, & C_3 = \varepsilon_{Si}\dfrac{2Nd}{(N - N_1 - 2N_2)}, \\ C_4 = \varepsilon_{SiO_2}\dfrac{N_2 d}{N_1} & C_5 = \varepsilon_{SiO_2}\dfrac{(N_1 + 2N_2)d}{N_2} \end{cases} \tag{5.4}$$

The effective dielectric constant ε_{eff}^1 is thus expressed as

ATTENTION: The Singapore Copyright Act applies to the use of this document. Nanyang Technological University Library

$$\begin{cases} \varepsilon_{eff}^{1} = C_{eff}\dfrac{N}{Nd} = \dfrac{C_{eff}}{d} = \dfrac{\varepsilon_{Si}[A_1\varepsilon_{SiO_2}^2 + A_2\varepsilon_{SiO_2}\varepsilon_{air} + A_3\varepsilon_{SiO_2}\varepsilon_{Si} + A_4\varepsilon_{Si}\varepsilon_{air}]}{B_1\varepsilon_{SiO_2}^2 + B_2\varepsilon_{SiO_2}\varepsilon_{air} + B_3\varepsilon_{SiO_2}\varepsilon_{Si} + B_4\varepsilon_{Si}\varepsilon_{air}} \\ A_1 = 2(1+2x)^2 x\sqrt{P} \\ A_2 = (1+2x)^2\sqrt{P} \\ A_3 = (1-\sqrt{P}-2x\sqrt{P})(1+2x+4x^2) \\ A_4 = (1-\sqrt{P}-2x\sqrt{P})x/2 \\ B_1 = 2(1+2x)^2 x\sqrt{P}(1-\sqrt{P}-2x\sqrt{P}) \\ B_2 = (1+2x)^2\sqrt{P}(1-\sqrt{P}-2x\sqrt{P}) \\ B_3 = (1+2x+4x^2)[(1+2x)\sqrt{P}+(1-\sqrt{P}-2x\sqrt{P})^2] \\ B_4 = 2x[(1+2x)\sqrt{P}+(1-\sqrt{P}-2x\sqrt{P})^2] \end{cases} \tag{5.5}$$

where $x = N_2/N_1$ is the thickness ratio of the oxidized layer to the void. We define the degree of oxidation, F, which is the volume ratio of SiO_2, V_{SiO_2}, to the sum of Si, V_{Si} and V_{SiO_2}:

$$F = \frac{V_{SiO_2}}{V_{Si}+V_{SiO_2}} = \frac{4N_1N_2+4N_2^2}{N^2-N_1^2} = 4P\frac{x+x^2}{1-P}\ (0 \le F \le 1) \tag{5.6}$$

Therefore,

$$x = \frac{1}{2}\left[\sqrt{1+\frac{F}{P}(1-P)}-1\right] \tag{5.7}$$

From Equations 5.5 and 5.7, it can be seen that if considering the partial oxidation of the PS surface, its effective dielectric constant depends on its porosity and oxidation degree. If $F = 0$, and 1, Equation 5.5 degrades into Equations 5.2 and 5.3, respectively. This means: (1) when $F = 0$, the PS consists of two components: silicon and voids; (2) if the surface is partial oxidized ($0 < F < 1$), the system contains three components: silicon oxide, silicon, and voids; (3) when $F = 1$, i. e. PS layer is completely oxidized, the silicon phase disappears and another two-component system (SiO_2 + pores) is produced.

ATTENTION: The Singapore Copyright Act applies to the use of this document. Nanyang Technological University Library

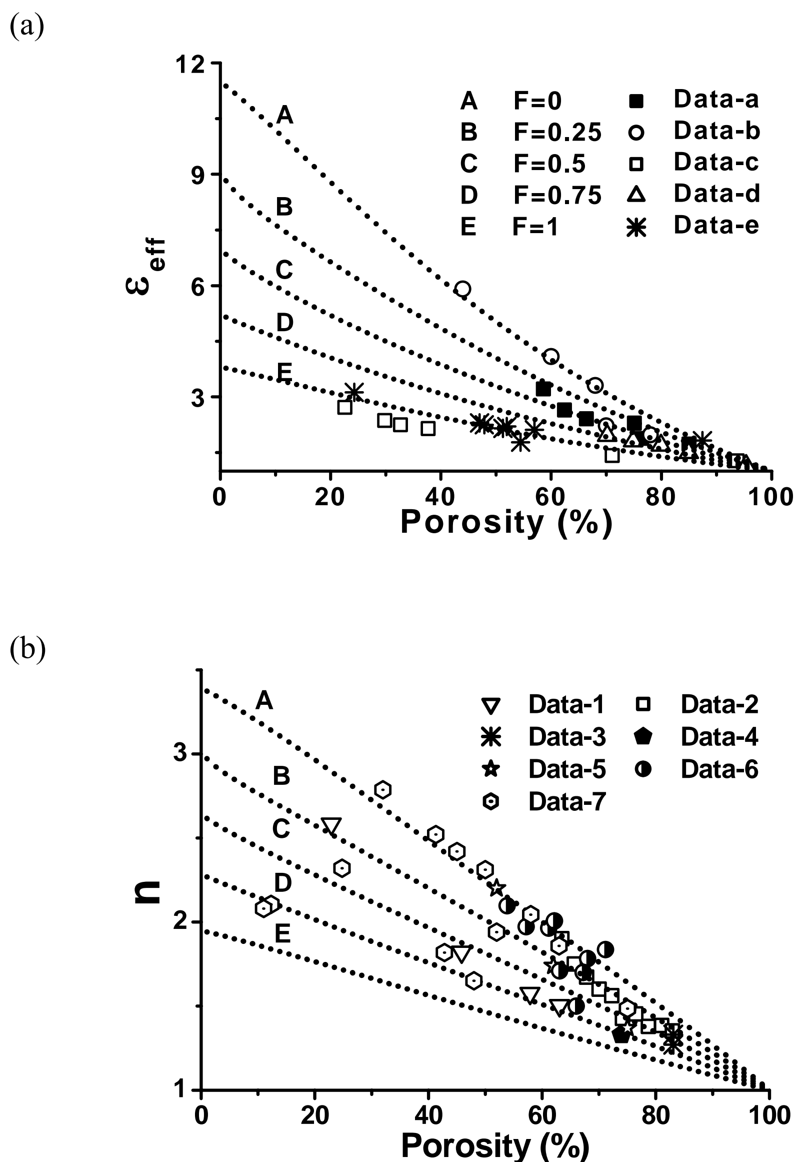

Figure 5.12 (a) Relation between the porosity, dielectric constant and oxidation degree of PS. Experimental data: Data-a[224] and Data-b[225] for PS; Data-c,[226] Data-d[227] and Data-e[228] for porous silica. (b) Relation between the porosity, refractive index and oxidation degree of PS. Experimental data: Data-1,[217] Data-2,[229] Data-3,[230] Data-4,[231] Data-5,[232] Data-6,[218] and Data-7[233] for PS. $F = 0$ and $F = 1$ corresponds to pure PS and pure porous silica.

Figure 5.12 compares theoretical results with measured values of porosity and oxidation extent dependence of (a) dielectric constant and (b) refractive index n ($n = \sqrt{\varepsilon_{eff}}$). $F = 0$, $F = 1$ and $0 < F < 1$ corresponds to pure PS, pure porous silica

ATTENTION: The Singapore Copyright Act applies to the use of this document. Nanyang Technological University Library

and oxidized PS, respectively, and the larger F value corresponds to the more heavily oxidized PS. As observed, the experimental data for PS and porous silica match well with the current Serial-Parallel model. Therefore, a mixture of partially oxidized silicon network with inclusion of columnar voids could be described with the model in terms of effective dielectric constant. The trend suggests that ε_{eff} and n can be reduced by increasing the porosity and oxidation layer thickness.

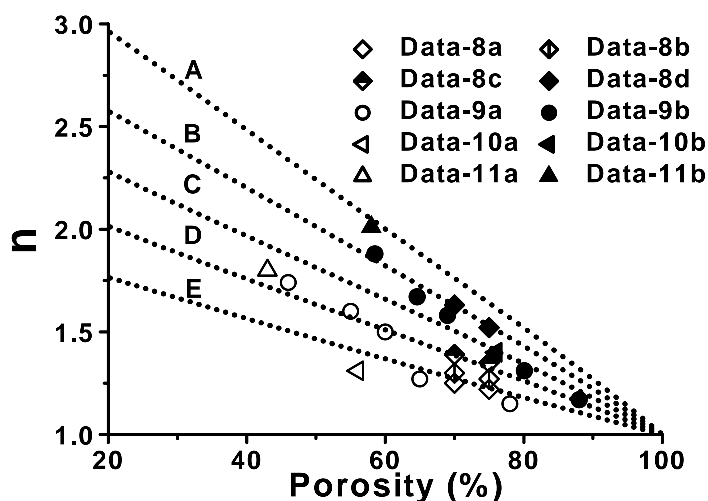

Figure 5.13 Evolution of the refractive index of PS layers with different oxidation degree. Experimental data: Data-8a, Data-8b, Data-8c and Data-8d,[234] Data-9a and Data-9b,[134] Data-10a and Data-10b,[235] Data-11a and Data-11b[221] for PS. The filled and the unfilled symbols denote the measured refractive index of PS before and after oxidation, respectively. $F = 0$ and $F = 1$ corresponds to pure PS and pure porous silica.

Figure 5.13 shows the evolution of the refractive index of PS layers with different oxidation degree. The filled and the unfilled symbols denote the measured refractive index of PS before and after oxidation, respectively. From the comparison, we are able to find the oxidation degree. Comparing the Data-8d, c,

ATTENTION: The Singapore Copyright Act applies to the use of this document. Nanyang Technological University Library

and a, with the calculated values in Figure 5.13, it is found that these data correspond to the oxidation degree of $F \approx 0.25$ (lightly oxidized), 0.75 (heavily oxidized), and 1.0 (complete oxidized).

5.3.3 Summary

Functional dependence of the effective dielectric constant of passivated PS on the porosity and oxidation degree has been derived by considering the contribution from the components of silicon oxide surface, silicon backbone and voids using a Serial-Parallel capacitance structural model. Agreement between modeling predictions and the measured experimental data has been reached, which turns out an effective method that enables us to determine the extent of surface oxidation by measuring the dielectric response of the chemically passivated porous structure.

ATTENTION: The Singapore Copyright Act applies to the use of this document. Nanyang Technological University Library

Chapter 6 Surface Metalization

6.1 Introduction

Over the last few years, PS has been regarded as a promising material for applications in the microelectronics such as waveguides,[162] photodiodes,[163] and various types of sensors.[164] These applications usually require some kinds of metal layers or metallic patterns on the top of the PS substrate (e.g. electrodes, contact masks, and mechanical support). Furthermore, PS layers have also been proposed for a potential application as the host matrix for polymers or metals, which have interesting optical properties.[143] For example, Pt-coated *n*-type PS electrodes have shown good solar energy conversion, which is one of the highest for *n*-Si photoelectrochemical solar cells.[165] Various metals such as Al,[236] Ti,[236] and Cu[237, 238] have been deposited on PS surface by various methods such as electrodeposition,[239] plating,[237] rf-sputtering,[238] and evaporation.[236] However, the progress, till today, is not satisfactory. Several papers focusing on the surface metallization of PS have conflicted conclusions to each other. Ghosh *et al*.[166] observed a blue-shift (~0.05 eV) in PL and a small reduction in its intensity upon Cu deposition in the thickness range of 10–40 nm on the surface of PS and ascribed the blue-shift to the small variation of localized states in PS. Huang[240] also reported a blue-shift (~0.044 eV) in PL for PS immersed in CuF_2. Ansari *et al*.,[238] on the other hand, reported a red-shift in PL peaks from 620 nm to 750 nm for the Cu-deposited PS with the deposition thickness 4.5–17 nm and larger reduction in PL intensity. The reduction in PL intensity was attributed to the absorption of the

ATTENTION: The Singapore Copyright Act applies to the use of this document. Nanyang Technological University Library

incident light energy into the Cu films. Similarly, Andsager *et al*.[241,242] found that the Cu deposition by wet chemistry or by evaporation quenched the luminescence of PS and shifted it towards lower energy. They attributed the quenching to a direct disruption of the surface radiative centers and the red-shift to luminescence evolution from the surface towards the sublayer near bulk. These different variations reported on the PL shift and intensity possibly result from different deposition methods.

Another drawback for the PS application in the microelectronics is its thermal structural instability.[243] This thermal property of the as-prepared PS is undesirable in the VLSI process, so that the PS region must be completely converted to a silicide to obtain a sufficient stability. Although the reaction between metal atoms and Si atoms of the substrate was found,[244,245] no strongly enhanced atomic diffusion through the pores was observed at RT for as-prepared PS substrates. As a result, annealing of PS is necessary for the preparation of thin-film silicide layer.[246] Many metals can react with the Si nanosolids at high temperature, which will obviously affect the properties of PS or metal-PS structure. Martín-Palma *et al*.[236] observed that Ti contacts to PS become clustered, while Al tends to diffuse into the PS layer, and after annealing there is a gradual transition between Ti and the PS layer. Pérez-Rigueiro *et al*.[247] showed that rapid thermal processing of Ti at 700ºC, in contrast to Al and Au, leads to better electrical performance of the contacts, probably as a consequence of the formation of $TiSi_2$ compounds. However, these researches just focused on the electrical or structural properties of metal-PS structures after annealing; and little attention has been given to the corresponding

ATTENTION: The Singapore Copyright Act applies to the use of this document. Nanyang Technological University Library

optical behavior. Consequently, a further exploration of the physical phenomena in the metal-PS structure is necessary.

6.2 Experimental Details

The PS samples were prepared with an applied current density of 90 mA/cm^2 for 10 min. Cu, Al, and Ti metal layers were deposited on the surface of PS samples using the FCVA technique. After the effective control on the arc current and deposition time, Cu, Al, and Ti metal layers of ~10 nm thickness were deposited on the surface of PS substrates at RT. Rapid thermal annealing was performed on as-grown PS and metalized PS samples, respectively, at 800 ^{o}C for 10 min in a vacuum chamber with a residual pressure of 10^{-6} Torr.

6.3 Results and Discussion

6.3.1 Before Annealing

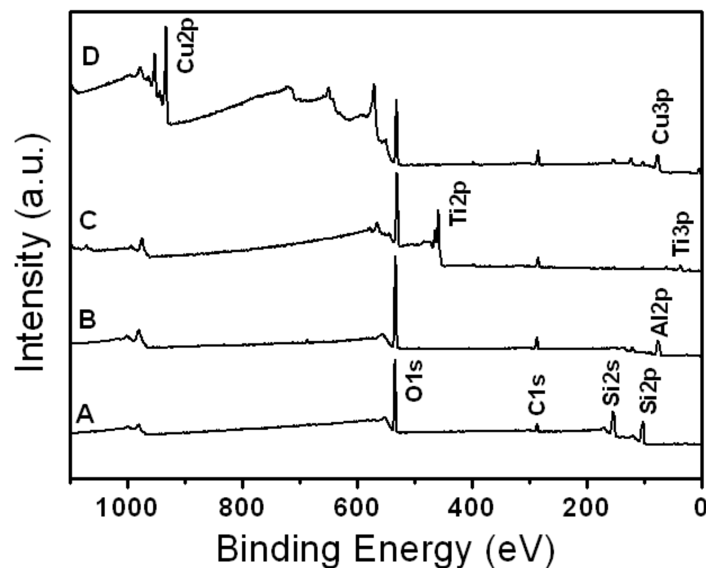

Figure 6.1 XPS spectra of the as-grown and metal-deposited PS samples showing the existence of different metals (Table 6.1) in metal-deposited samples.

ATTENTION: The Singapore Copyright Act applies to the use of this document. Nanyang Technological University Library

Figure 6.1 shows the XPS spectra of the PS samples before annealing. Curve A represents the result for the as-prepared sample, and curves B–E for the samples deposited with different metals as listed in Table 6.1. The Cu-2*p*, Ti-2*p* and Al-2*p* peaks in the spectra show that Cu, Al, and Ti have been deposited on the surface of PS samples.

Table 6.1 Summary of the results for PS samples deposited with different metals before annealing

Sample	Deposition	E_{PL} (eV)	E_{PA} (eV)	$2W$ (eV)	E_G (eV)	E_{2p} (eV)
A	/	2.07	2.62	0.55	2.35	101.98
B	Al	2.07	2.51	0.44	2.29	102.01
C	Ti	2.07	2.77	0.70	2.42	102.02
D	Cu	2.11	2.21	0.10	2.16	101.76

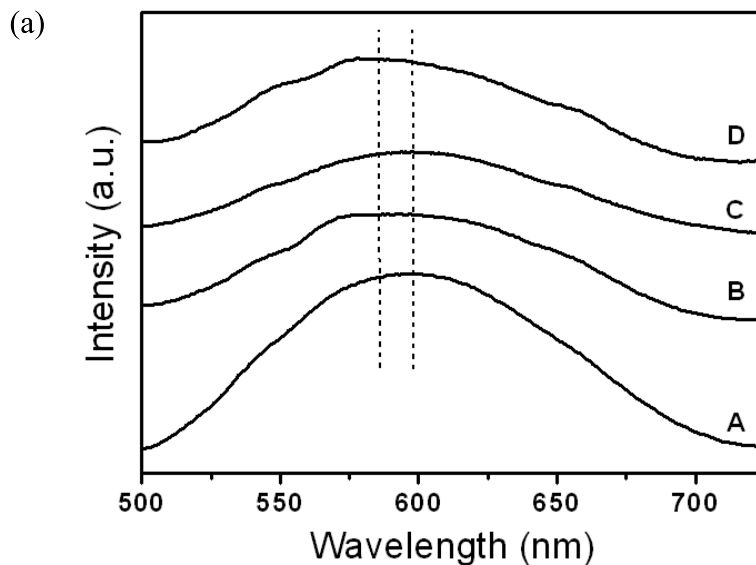

ATTENTION: The Singapore Copyright Act applies to the use of this document. Nanyang Technological University Library

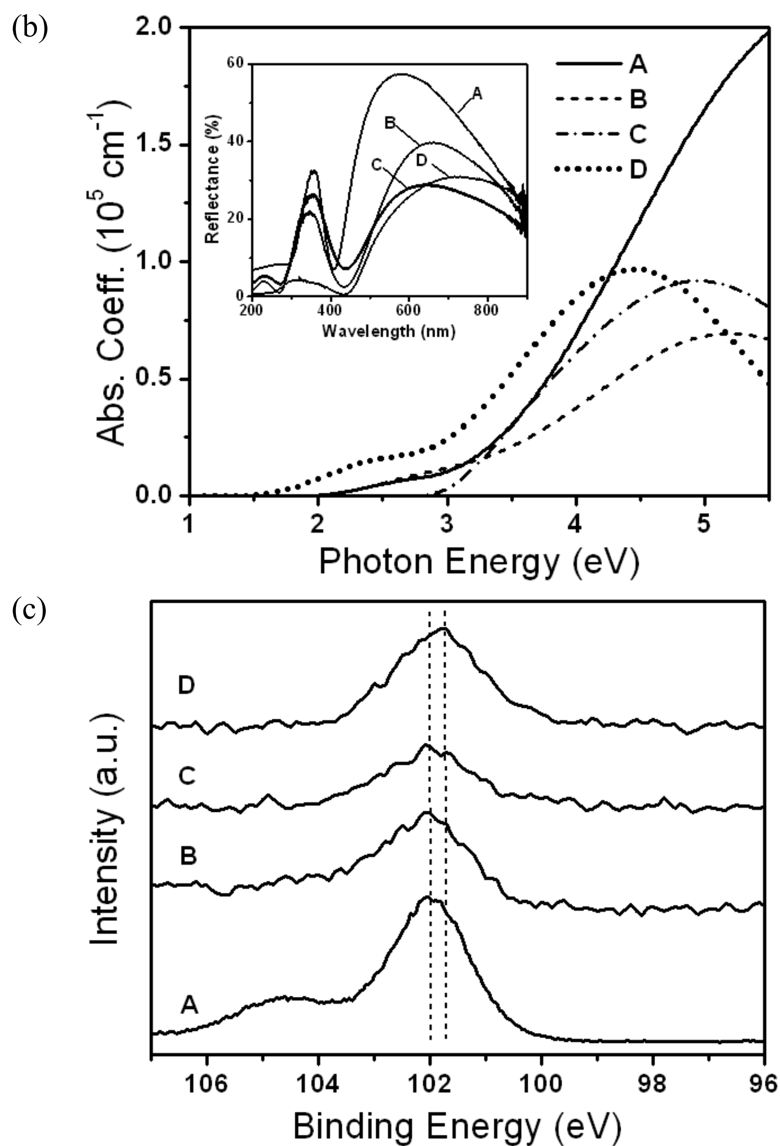

Figure 6.2 Effects of surface metal deposition on (a) the RT PL spectra, (b) the absorption and reflection spectra (inset), and (c) XPS Si-2*p* profiles of PS samples.

Figure 6.2 (a) shows the PL results of as-grown and metal-deposited PS samples. Compared with the as-grown sample, the PL intensities of metal-deposited ones decrease because the resulting surface modification introduces nonradiative defects.[248,249] Cu-deposited sample exhibits a blue-shift in the PL (~0.04 eV) while the PL peak energies of Al- and Ti-deposited ones almost remain

ATTENTION: The Singapore Copyright Act applies to the use of this document. Nanyang Technological University Library

constant. Figure 6.2 (b) displays the spectral dependence of the absorption coefficient of PS samples A–E obtained by fitting reflection spectra (inset). As observed, there is obvious red-shift in the absorption peak for Cu-deposited sample as compared with the as-grown one while the absorption variations for Ti- and Al-deposited ones are thought to be insignificant. The XPS Si-2*p* profiles, as shown in Figure 6.2 (c) exhibits an obvious Si-2*p* core level shift towards lower binding energy for Cu-deposited sample compared with the as-grown one. The E_{PL}, E_{PA}, E_{2p}, and derived information on Stokes shift $2W$ and E_G for metal-deposited PS samples before annealing have been shown in Table 6.1. As observed, the effects of Al and Ti deposition on the optical and electronic properties of PS are insignificant while Cu-deposited sample exhibits obvious PL blue-shift and interesting E_G and Stokes Shift decreases. It was reported by Hall and Racette [250,251] that the Cu interstitial is the rapid diffusing species in Si. Diffusion of Cu in PS differs significantly from diffusion of Cu in bulk Si for several reasons including: higher concentrations of impurities, possible amorphous structure,[39] geometrical and boundary effects at the nanometer scale that decrease the mobility of atoms, the presence of dangling bonds on the PS surface,[252,253] and the presence of a large surface area long which to diffuse. The diffusion of Cu in PS proceeds predominantly along the surface, rather than the bulk.[254] Therefore, Cu deposition will largely changes the surface properties of PS, which further modifies the crystal field and thus affects the PL, PA, E_G, and Si-2*p* level variations.

ATTENTION: The Singapore Copyright Act applies to the use of this document. Nanyang Technological University Library

6.3.2 After Annealing

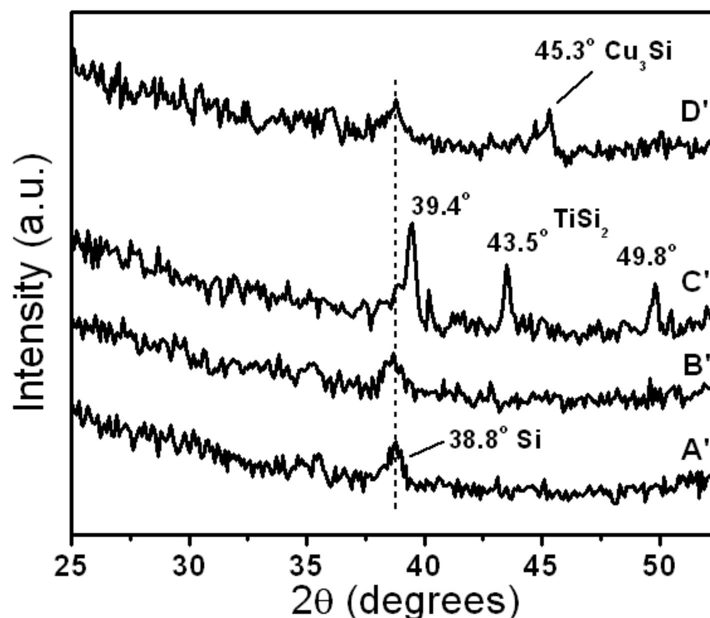

Figure 6.3 XRD spectra of the as-grown and metal-deposited PS samples (Table 6.2) after annealing at 800 ºC.

A XRD scan at 1° grazing angle incidence with Cu K_{α} radiation (1.54Å) was conducted to ascertain metal silicide formation. Before annealing, only 38.8^{o}, which corresponds to Si (220), was observed for all measured samples, which shows that metal films caused no major changes in the nature of chemical bonding present on the PS layer before annealing. However, there are a new peak at 45.3^{o} and three new peaks at 39.4^{o}, 43.5^{o} and 49.8^{o} in the XRD spectra (Figure 6.3) of Cu- and Ti-deposited samples after thermal annealing at 800 ^{o}C for 10 min, respectively. The former represents the formation of copper silicide in the form of Cu_3Si[255,256] and the latter is associated to the $TiSi_2$ phase[257,258].

The PL spectra in Figure 6.4 (a) shows complete PL quenching for all the samples after annealing. The PL vanishing results from joint effects of sintering

ATTENTION: The Singapore Copyright Act applies to the use of this document. Nanyang Technological University Library

phenomenon and hydrogen desorption. During thermal treatment at temperatures above 450 ^{o}C, surface diffusion of Si atoms along the pore walls occurs, causing the microstructures to begin to sinter. The thermal disruption will lead to structural changes, e.g., the size distribution and the connections among crystallites in PS. If these changes increase the Bohr radius of the electron and/or hole, the PL lifetime must decrease, and hence, PL is apparently quenched.[259,260,261] On the other hand, annealing at temperatures above 350 ^{o}C causes hydrogen to release from the films[262] which generates nonradiative recombination – dangling bonds, and thus decreases the PL intensity.[260,263] The absorption in Figure 6.4 (b) for the metal-deposited samples after annealing shifts obviously towards lower photon energy compared with the ones before annealing while the absorption for as-grown sample almost remains constant. Many authors[170,264,265] attributed the PA red-shift to the hydrogen desorption from surface of nanoscale particles after annealing. However, the fact that the PA energy almost stays constant for as-grown sample before and after annealing in this work seems not to support their premises. Compared with Figure 6.2 (c), the Si-2*p* peaks for all the samples after annealing in Figure 6.4 (c) obviously shift towards higher binding energy. The large Si-2*p* level shift results from the crystal field enhancement induced by surface oxidation happened in high temperature annealing because during high temperature annealing even with ultrahigh, the internal surface of a PS sample can still absorb residual oxygen and form a temperature-dependant mixture of Si–OH, Si–H_x and Si–O–Si.[266] It is noticed that Cu- and Ti- deposited samples exhibits a Si-2*p* shift towards lower binding energy compared with as-grown one even after annealing. The E_{PA} and E_{2p}

ATTENTION: The Singapore Copyright Act applies to the use of this document. Nanyang Technological University Library

for annealed PS samples have been shown in Table 6.2. As observed, The annealing of Cu- and Ti-deposited samples obviously affects the absorption edge and Si-2*p* level due to the formation of copper/titanium silicides after annealing, which increases the concentrations of electrons in the conduction band of PS and modifies the crystal field. While annealing at 800 ^{o}C just drives the diffusion of Al towards the PS layer and thus doesn't affect the absorption edge and Si-2*p* level of Al-deposited sample obviously.

Table 6.2 Summary of the results for PS samples deposited with different metals after annealing

Sample	Deposition	E_{PL} (eV)	E_{PA} (eV)	$2W$ (eV)	E_G (eV)	E_{2p} (eV)
A′	/	/	2.76	/	/	103.51
B′	Al	/	2.01	/	/	/
C′	Ti	/	1.65	/	/	102.88
D′	Cu	/	1.32	/	/	102.58

(a)

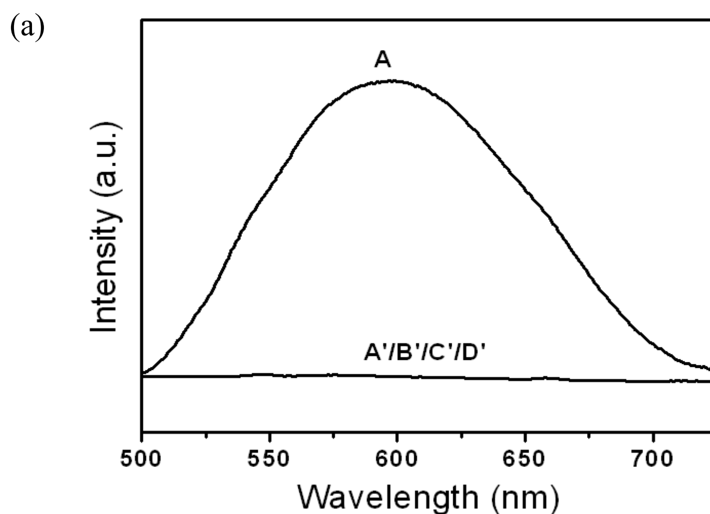

ATTENTION: The Singapore Copyright Act applies to the use of this document. Nanyang Technological University Library

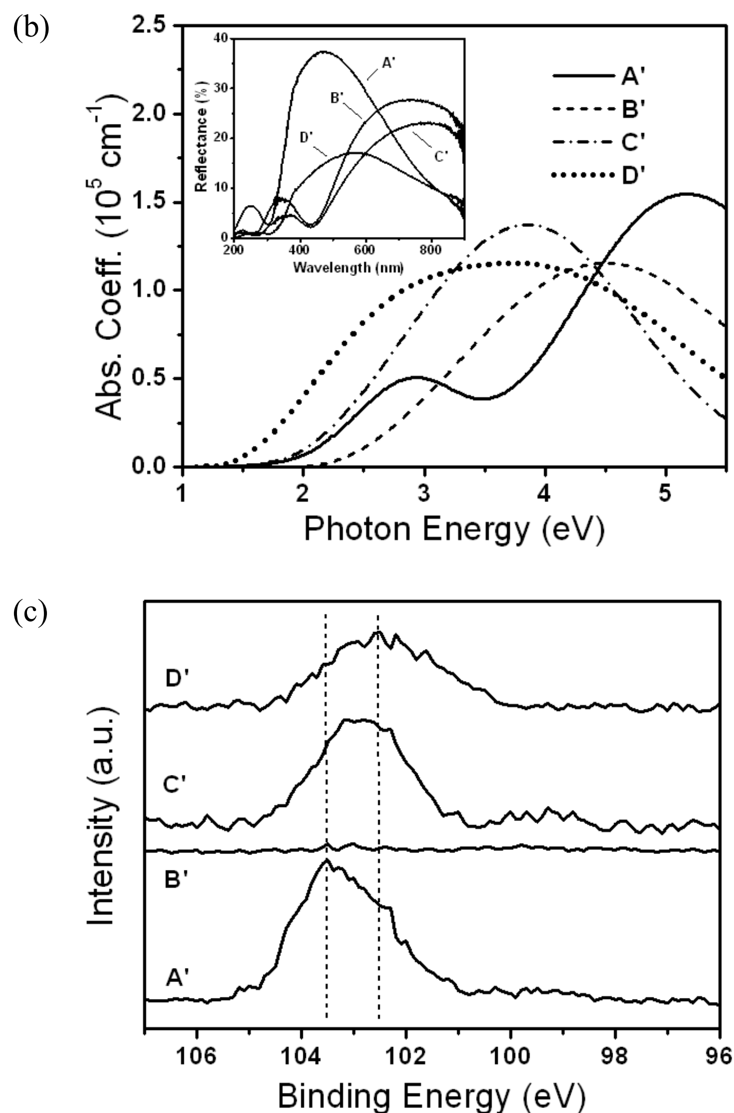

Figure 6.4 Effects of annealing at 800 ºC on (a) the RT PL spectra, (b) the absorption and reflection spectra (inset) and (c) XPS Si-2*p* profiles of as-grown and metal-deposited PS samples.

6.4 Summary

It has been found that Al and Ti deposition has no obvious effects on the electronic and optical properties of PS at RT while Cu-deposited sample exhibits PL blue-shift, PA red-shift, E_G decrease, and Si-2*p* level shift due to the Cu diffusion at the surface of PS, which modifies the surface properties of PS. After

ATTENTION: The Singapore Copyright Act applies to the use of this document. Nanyang Technological University Library

annealing, Cu- and Ti-deposited samples exhibit obvious PA red-shift and Si-2*p* level shift, which arise from the crystal field variation due to the formation of Cu/Ti silicides at the surface as well as the conduction electronic transportation.

ATTENTION: The Singapore Copyright Act applies to the use of this document. Nanyang Technological University Library

Chapter 7 Critical Anodization Temperature for Optical Transition

7.1 Introduction

The low-dimensional semiconductor structures are of high interest due to the significant technological implications in optics and microelectronics. PS is becoming increasingly important due to the prospect of producing fully integrated electronic devices. The study of the correlation between the properties of this high porosity structure and anodization conditions is essential, to control its fabrication processes for the potential applications as optoelectronic materials. Much research has been focused on the effects of anodization current density,[267] electrolyte composition,[268] and anodization time[269] on the structural and optical properties of PS. Little attention has been given yet on the effect of anodization temperature, especially above RT. Several reports focusing on the temperature effects have derived conflicting conclusions. Ono *et al*.[270] found that the luminescence intensity decreases exponentially and a red-shift in the PL peak occurs with lowering anodization temperature from 313 K to 273 K, which, as they suggested, is attributed to the dominant formation of amorphous silicon below 283 K. Setzu *et al*.[271] on the other hand, reported an increase in the PL intensity and the peak wavelength independent of temperature when the preparation temperature decreases from 300 K to 238 K. Blackwood *et al*.[272] observed a blue-shift in PL and randomly varying intensity with the anodization temperature reduction from

ATTENTION: The Singapore Copyright Act applies to the use of this document. Nanyang Technological University Library

310 K to 263 K; and they proposed that the contradictory between the aforementioned conclusions should be caused by different ethanol content of etching solutions, current density, and drying process. The explanation seems reasonable at the temperature ranging around or below RT. However, its applicability on anodization temperature at RT or higher needs to be proved. An abnormal variation of the optical behavior and the binding energy of PS fabricated at temperatures above RT have been observed, which cannot be explained based on the above mentioned mechanisms.

7.2 Experimental Details

The PS samples were prepared with a current density of 90 mA/cm^2 applied for 10 min. The anodization temperatures, which auto-controlled by a heating system with electrical contact thermometer, were set at 298 K, 323 K, 343 K and 363 K, respectively.

7.3 Results and Discussion

7.3.1 Critical Anodization Temperature

Figure 7.1 shows PL spectra of PS samples. It is observed that the PL intensity decreases with the rise of anodization temperature, which follows similar trend as reported by Setzu *et al*,[271] but they did not observe any wavelength shifts in PL spectra. While in this study, PS samples exhibit a red-shift in PL spectra when the temperature is raised from RT to 343 K. Blackwood, et. al.[272] have ascribed the PL blue-shift/red-shift to the size reduction/enlargement at different anodization

ATTENTION: The Singapore Copyright Act applies to the use of this document. Nanyang Technological University Library

temperatures. They suggested that at lower anodization temperature smaller silicon nanocrystals are stabilized due to a combination of their reduced solubility and the increased viscosity of the diffusion layer that leads to a higher localized concentration of silicon ions, thereby, allowing smaller nanocrystals to be in equilibrium with their surroundings. Interestingly, in this study, the PL is found to reversely shift towards higher energy level when the temperature is further raised to 363 K, which is beyond the scope of the abovementioned explanation.

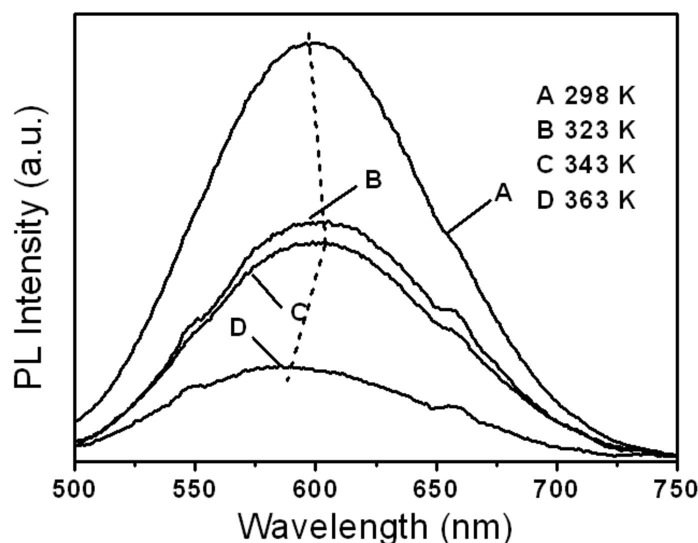

Figure 7.1 Anodization temperature dependence of the RT PL spectra of PS.

Figure 7.2 displays the spectral dependence of the absorption coefficient of PS samples obtained by fitting reflection spectra (inset). As observed, the values of absorption coefficient are strongly dependent on anodization temperature, especially in the range of higher photon energy. The XPS Si-2*p* profiles, as shown in Figure 7.3 exhibits an obvious Si-2*p* core level shift towards lower binding energy for PS samples with the elevation of anodization temperature and then shift

ATTENTION: The Singapore Copyright Act applies to the use of this document. Nanyang Technological University Library

somewhat towards higher energy at 343 K, the critical anodization temperature (T_{aC}).

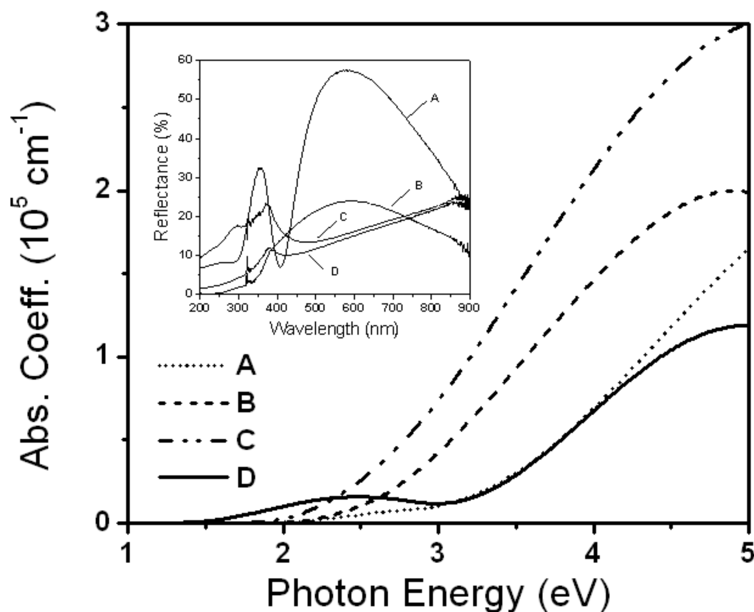

Figure 7.2 Anodization temperature dependence of the absorption and reflection spectra (inset) of PS samples, which give the PA edge energy.

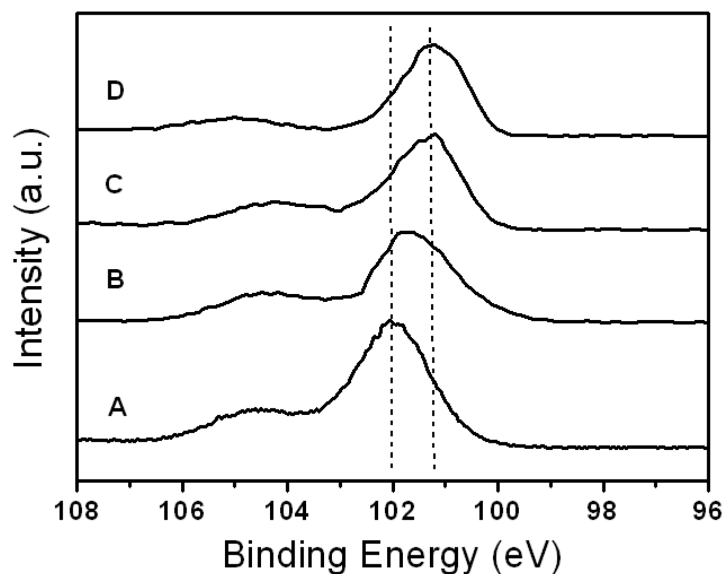

Figure 7.3 Anodization temperature dependence of Si-2*p* profiles of PS measured using XPS at RT.

ATTENTION: The Singapore Copyright Act applies to the use of this document. Nanyang Technological University Library

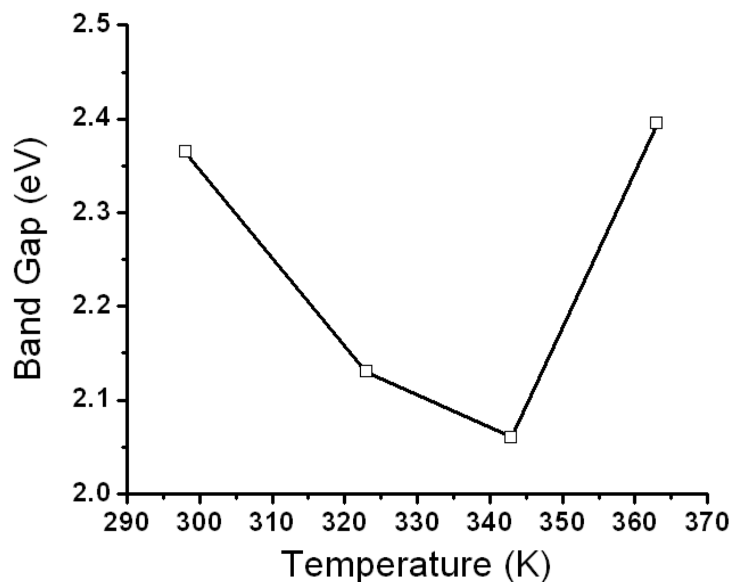

Figure 7.4 Anodization temperature dependence of E_G of PS measured by averaging the PL and PA energies.

The correlation between the E_G and the anodization temperature shown in Figure 7.4 indicates that the E_G decreases with the elevation of anodization temperature and then turns up abruptly after T_{aC}. Repeated experimental confirms this finding that is reproducible.

7.3.2 Mechanism

Mechanism for the reverse trend in the PL, PA, and Si-2*p* level energy variations happening at the temperatures below and above T_{aC}, has not yet been fully understood. We may suggest that the mechanism for the etching of silicon is far from simple, and all these variations may be not simply induced by size effects. Other factors such as surface passivation may also play an important role in that higher temperature fabrication may change the surface species and surface

ATTENTION: The Singapore Copyright Act applies to the use of this document. Nanyang Technological University Library

coverage. It is worthy of notice that the PL, PA, and Si-2*p* level energy variation almost follow the same trend with the rise of anodization temperature whether the size effect and surface passivation effect are involved or not.

7.4 Summary

The anodization temperature strongly affects the structural and optical behavior of the PS. When the anodization temperature is raised from RT to T_{aC}, PS exhibits a red-shift in PL, PA, and a decrease in the Si-2*p* level shift and E_G as well until the transition point. While at higher temperature up to 363 K, reverse variation trend for these properties occurs: Si-2*p* level shift towards higher energy and E_G expands associated with blue-shift in PL and PA. The origin for the intriguing reverse variations happening above and below T_{aC} needs further investigation.

ATTENTION: The Singapore Copyright Act applies to the use of this document. Nanyang Technological University Library

Chapter 8 Dielectric Relaxation and Transition

8.1 Introduction

Measurement of impedance is important for simultaneous dielectric characterization of materials. The technique has been widely employed to characterize the dielectric behavior of ceramic materials. [273] Impedance measurement with respect to frequency allows one to inspect the detailed physical processes inside materials through their electrical analogs.[274] In conjunction with structural characterization, impedance analysis yields a complete physical picture of various phenomena occurring in the specimen under different conditions. The most important advantage of impedance measurements is that they can distinguish individual contributions to electrical conduction or to polarization from different sources like the bulk, grain boundaries, intergranular contact regions, and electrode–sample interface regions where defects are generated. This chapter presents the findings for impedance characterization of complex dielectrics by the so-called Cole-Cole plot, as a function of the temperature along with discussion of possible mechanisms.

8.2 Experimental Details

The PS samples were prepared with an applied current density of 80 mA/cm^2 for 10 min. The PS layers formed exhibit a red PL with peak energy at about 2.0 eV and the corresponding particle size is about 1.8 nm. The dielectric

ATTENTION: The Singapore Copyright Act applies to the use of this document. Nanyang Technological University Library

measurements were performed in several stages from RT to 573 K in 50 K steps and above 573 K in 25 K steps. The temperature was held for 0.5 h prior to each measurement.

8.3 Results and Discussion

8.3.1 Impedance Response

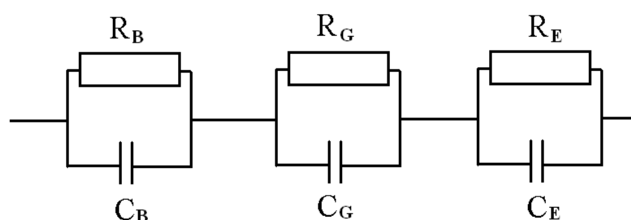

Figure 8.1 Circuit model for describing the dielectric behavior of PS, where R_B and C_B are the bulk-grain resistance and capacitance, R_G and C_G are the grain-boundary resistance and capacitance, and R_E and C_E are the electrode/film-interface resistance and capacitance, respectively. (from Ref. 187)

Relaxation of the impedance can be ideally illustrated with Debye's expression, where the material is represented by a parallel circuit with a pure resistor R and a capacitor C, as shown in Figure 8.1. When a Cole-Cole plot is considered, the impedance response commonly shows a semicircular form.[189] Figure 8.2 illustrates the impedance response of the PS sample from RT to 798 K. For temperatures below 673 K, complex impedance plots show only one depressed single semicircular arc, indicating that only one primary mechanism, the bulk grain behavior, exists for polarization within the PS film at temperatures below 673 K. The second intercept on the real axis made by the semicircle corresponds to the resistance offered by the bulk grain. As can be observed, with an increase in

ATTENTION: The Singapore Copyright Act applies to the use of this document. Nanyang Technological University Library

temperature the intercept of the semicircles shifts towards lower Z' values, indicating reduction of the bulk grain resistance.

When the temperature is increased to 673 K or above, the effects of grain boundary become more significant by the presence of another overlapping semicircle. The two semicircles at high and low frequencies can be assigned to charge transport within the grain interior and grain boundary effects, respectively. In general, the effects of grain boundaries on the electrical conductivity originates from a grain boundary potential barrier or from space charge layers that are depleted in majority charge carriers and are localized along the grain boundaries. It is found that low frequency semicircular response is dominant with an elevation in temperature compared with the high frequency one, which means that the dominant dielectric relaxation mechanism has changed from bulk grain behavior to grain boundary behavior.

(a)

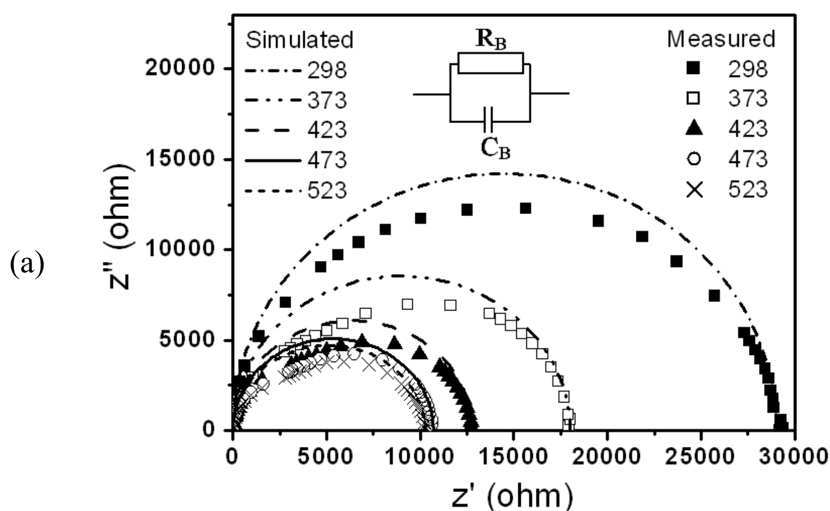

ATTENTION: The Singapore Copyright Act applies to the use of this document. Nanyang Technological University Library

(b)

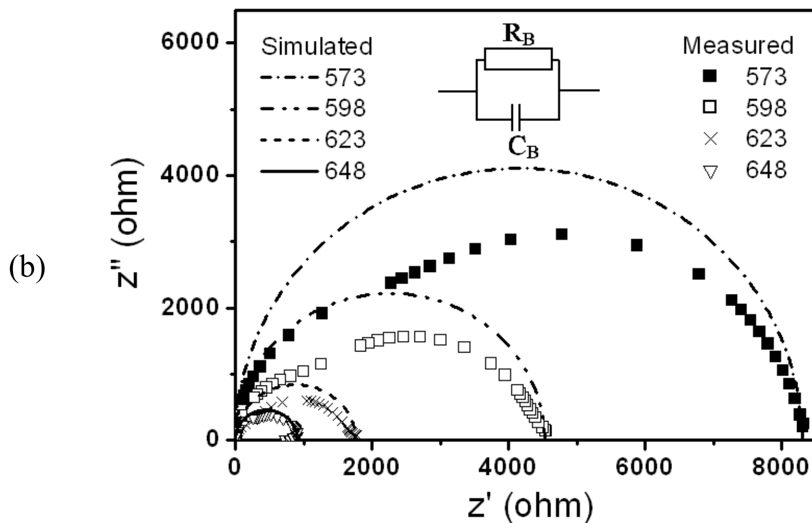

(c)

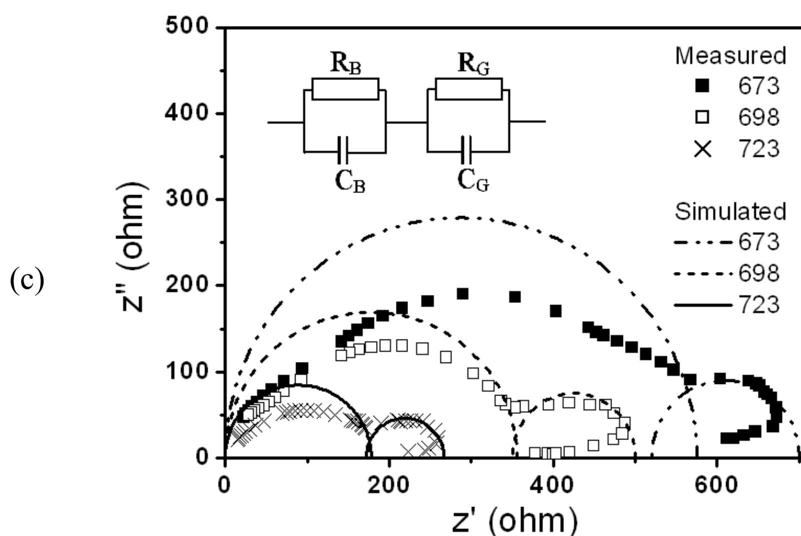

(d)

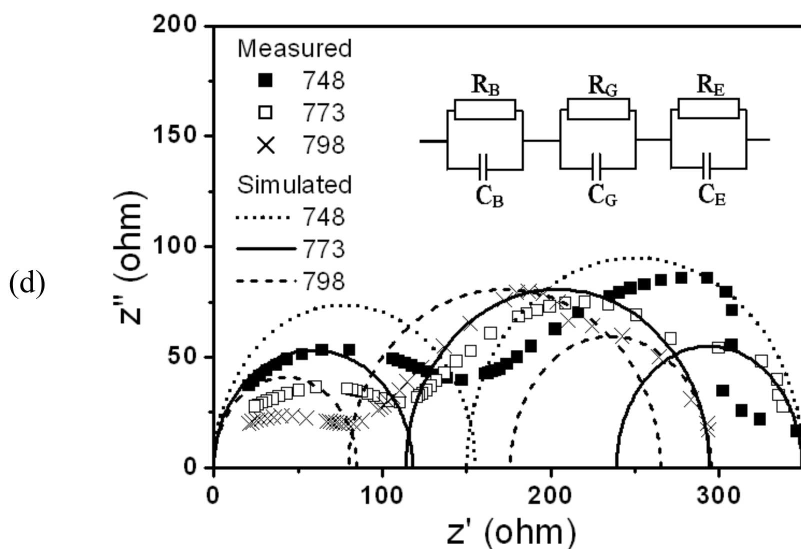

ATTENTION: The Singapore Copyright Act applies to the use of this document. Nanyang Technological University Library

Figure 8.2 Cole–Cole plots of PS at different temperatures: (a) 298–523K, (b) 573–648 K, (c) 673–723 K, and (d) 748–798 K. The dots represent the data measured by the *RCL* meter at different temperatures and the lines correspond to simulation using the *RC* parallel circuit model (inset) for typical dielectric materials. (from Ref. 187)

The impedance spectra of the PS exhibit three semicircles when the temperature reaches about 773 K, with the formation of the tertiary semicircle in the low frequency region. When the temperature is increased further, this effect is more evident. We attribute this semicircle to an electrode/film interface effect. In general, the electrode/film effect results from space charge migration.[275] Ionic species with large relaxation times diffuse towards the electrode/film contact region and accumulate there. Polarization of this space charge gives rise to capacitance C_E and corresponding resistance R_E.

The Cole–Cole plots demonstrate the dielectric transition from dominance of the grain interior to dominance of the grain boundary at about 673 K, and then to dominance of the electrode/film interface at about 773 K. The transition of a perfect semicircle into an imperfect arc on the left or right may be due to limitation of equipment, which can only measure frequencies from 50 Hz to 1 MHz.[181]

8.3.2 Equivalent Circuit

The high temperature impedance behavior can be described by a series of triple parallel *RC* circuit elements[188] that correspond to the dielectric behavior of the grain interior, the grain boundary, and the electrode/film interface, respectively, as shown in Figure 8.1. Since the grain boundary normally exhibits higher resistance than the grain interior and lower resistance than the electrode/film interface, the

ATTENTION: The Singapore Copyright Act applies to the use of this document. Nanyang Technological University Library

first semicircle in the high frequency region can be attributed to the behavior of the grain interior while the intermediate and tertiary semicircles in the lower frequency region are attributed to the grain boundary and electrode/film interface. Here the resistor *R* represents ionic or electronic conduction mechanisms, while the capacitor *C* represents the polarizability of the PS. The complex impedance *Z** measured by the *RCL* meter can be expressed as

$$\begin{cases} Z^* = Z' - jZ'', \\ Z' = \dfrac{R_B}{1+\omega^2 R_B^2 C_B^2} + \dfrac{R_G}{1+\omega^2 R_G^2 C_G^2} + \dfrac{R_E}{1+\omega^2 R_E^2 C_E^2}, \\ Z'' = \dfrac{\omega R_B^2 C_B}{1+\omega^2 R_B^2 C_B^2} + \dfrac{\omega R_G^2 C_G}{1+\omega^2 R_G^2 C_G^2} + \dfrac{\omega R_E^2 C_E}{1+\omega^2 R_E^2 C_E^2}, \end{cases} \tag{8.1}$$

where Z' and Z'' represent the real and imaginary parts of the impedance and ω is the angular frequency. R_B and C_B are the bulk-grain resistance and capacitance, R_G and C_G are the grain-boundary resistance and capacitance, and R_E and C_E are the electrode/film interface resistance and capacitance, respectively.

8.3.3 Conductivity and Activation Energy

One way by which to extract the bulk electrical conductivity σ is using

$$\sigma = \frac{l}{R_B A}. \tag{8.2}$$

The second intercept of the high frequency semicircle with the real axis corresponds to the bulk resistance R_B. l is the thickness of the sample (15 μm) which was measured upon cross section of the sample by SEM; A is the area of the silver electrode (250 mm^2). The electrical conductivity of semiconductor materials

ATTENTION: The Singapore Copyright Act applies to the use of this document. Nanyang Technological University Library

is usually thermally activated, at least over a limited temperature and follows Arrhenius law,

$$\sigma = \sigma_0 \exp(-\frac{E_a}{k_B T}) = \sigma_0 \exp(-\frac{E_{TR} - E_F}{k_B T}), \tag{8.3}$$

where σ_0 is a pre-exponential factor and is characteristics of the material. E_{TR} is defined as the average energy of the conducting electrons. E_a, E_F, k_B, and T are, respectively, the activation energy for conduction, Fermi energy, Boltzmann's constant, and absolute temperature. Thus, the activation energy for conduction can be calculated from the slope of the straight line given by least-mean-square analysis of lnσ vs 1000/T as shown in Figure 8.3.

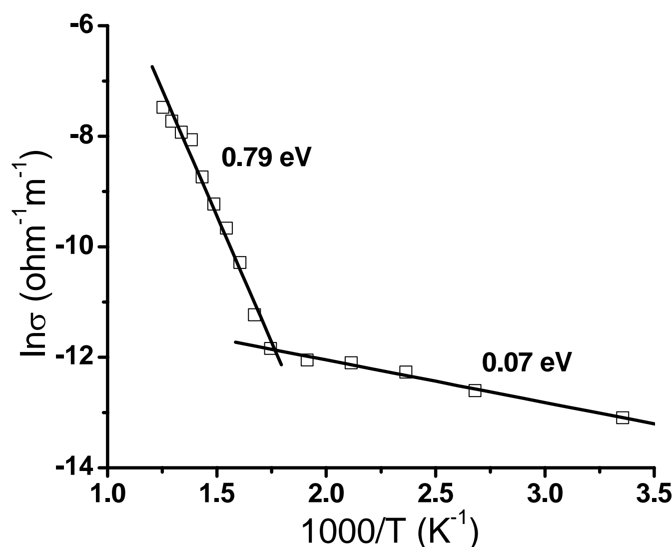

Figure 8.3 Arrhenius plot of the conductivity of PS with an activation energy transition from 0.07 to 0.79 eV at about 565 K. (from Ref. 187)

The activation energy for conduction is found to have a transition from 0.07 to 0.79 eV at about 565 K. Several researchers have proposed different mechanisms for the conduction transition of materials with a rise in temperature. Landstrass and

ATTENTION: The Singapore Copyright Act applies to the use of this document. Nanyang Technological University Library

Ravi[276] attributed the transition to the movement of hydrogen and defects from the electrically active deep level to nonactive sites during annealing. Mori *et al*.[277] suggested an existence of a surface conductive layer combined with chemical absorption and oxidation. Bharadwaja and Krupanidhi[278] proposed that the transition originated from the excitation of charge carriers from a set of shallow traps lying below the conduction band and/or oxygen ion mobility in the interior grains. Axelrod *et al.*[279] correlated the transition to the fractal geometry of PS and to thermally activated relaxation processes from localized and delocalized electronic states of silicon nanocrystallites below the Fermi edge. Here we propose this conduction transition behavior of PS originates from band tail hopping that occurs around the Fermi edge, as illustrated in Figure 8.4.

For *p*-type PS, the Fermi edge does not lie in the middle of the energy gap but instead shifts towards valence band. Because the activation energy obtained is less than half of the E_G derived from the PL measurements, E_{TR} does not equal E_C, and the main mechanism responsible for the conductivity is the band tail hopping, i.e. the electrons are transported from the Fermi edge to the conduction band tail. The inflexion 565 K can be viewed as the equilibration temperature at which a high temperature equilibrium regime and a low temperature frozen state are separate. The different variation in conductivity for the temperature above and below this critical point is due to changes in the electron concentration. Below the equilibration temperature, the electronic structure of PS is frozen and the density of electrons is constant. Hence E_{TR} is close to E_F and the corresponding activation energy is very small. Furthermore, the conductivity prefactor σ_0 is only about

ATTENTION: The Singapore Copyright Act applies to the use of this document. Nanyang Technological University Library

2.7×10^{-5} Ω^{-1} cm^{-1} as derived from the vertical intercept in Figure 8.3. When the temperature is raised above the equilibration temperature, the electrons near the Fermi edge are excited towards higher energy and E_{TR} shifts into the band tail near E_C. While the Fermi energy is pinned by the defect and dopant states due to the thermal equilibrium regime at every temperature, and consequently the shift of the Fermi edge is comparatively small. As a result, the conductivity is activated with much larger activation energy and a prefactor of about 70.3 Ω^{-1} cm^{-1}.

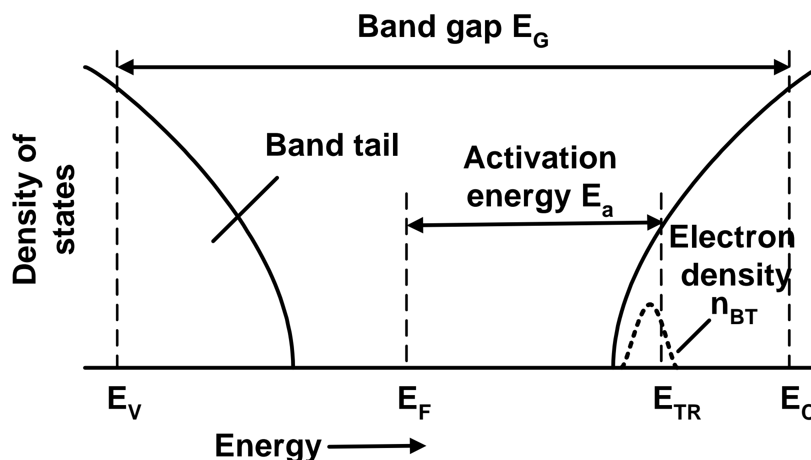

Figure 8.4 Schematic diagram of the distribution of the density of states showing the conductivity activation energy E_a, the average conduction energy E_{TR}, and the Fermi energy E_F (from Ref. 51).

8.3.4 Dielectric Relaxation and Transition

Data measured as complex impedance Z^* can be converted into the complex permittivity formalism ε^* by the relation

ATTENTION: The Singapore Copyright Act applies to the use of this document. Nanyang Technological University Library

$$\begin{cases} \varepsilon^* = \varepsilon' - j\varepsilon'' = \dfrac{1}{j\omega C_0 Z^*}, \\ \varepsilon' = \dfrac{Z''}{\omega C_0 Z^2}, \\ \varepsilon'' = \dfrac{Z'}{\omega C_0 Z^2}, \\ C_0 = \varepsilon_0 \dfrac{A}{l}, \end{cases} \tag{8.4}$$

where ε', ε'' and ε_0 represent the real and imaginary parts of the permittivity and the permittivity of vacuum, respectively. Z is the impedance modulus and C_0 is the measured vacuum capacitance of the cell and electrodes with an air in place of the sample. Figure 8.5 illustrates the evolution of the real and imaginary permittivity as a function of the frequency and temperature. When the temperature is raised to 573 K, a high degree of dispersion in the real permittivity occurs at low frequencies.

(a)

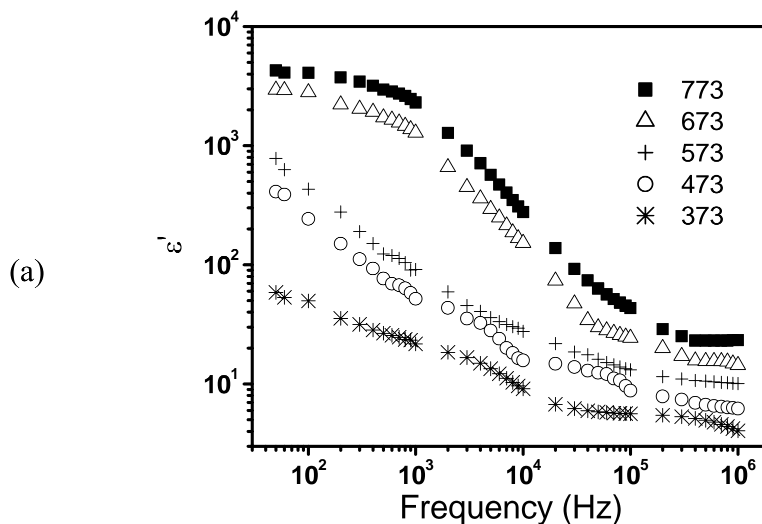

ATTENTION: The Singapore Copyright Act applies to the use of this document. Nanyang Technological University Library

(b)

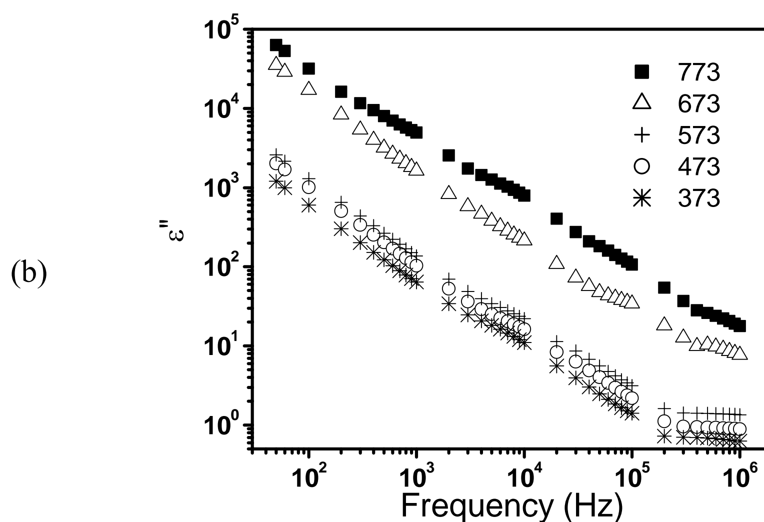

Figure 8.5 (a) Real part ε′ and (b) imaginary part ε″ of the permittivity of PS as a function of the frequency at different temperatures. (from Ref. 187)

Nobre and Lanfredi[280] attributed the dispersions to the presence of atomic defects which give the structure great flexibility and the capacity to form solid solutions. Because this dispersion behavior is generally found in dielectrics, in which a conduction hopping-type mechanism is present,[281] a more reasonable explanation would be that the appearance of band tail hopping at the equilibration temperature causes the large difference in permittivity at temperatures higher or lower than 573 K. The imaginary part ε″ decreases when the frequency increases linearly on a logarithmic scale first and then tends to be constant up to 100 kHz. The imaginary part of the complex permittivity describes the electromagnetic wave absorption, which is responsible for the loss in energy incident waves by electron excitation from the valence to the conduction band, given as[116,117]

ATTENTION: The Singapore Copyright Act applies to the use of this document. Nanyang Technological University Library

$$\begin{cases} \varepsilon''(\omega) = \dfrac{B}{\omega^2}\int ds \dfrac{f_{CV}(k)}{|\nabla[E_C(k) - E_V(k)]|}, \\ E_C(k) - E_V(k) = \hbar\omega = E_G + \hbar^2 k^2 / 2\mu, \end{cases} \tag{8.5}$$

where B is a constant. $E_C(k)$ and $E_V(k)$ correspond to energies in the conduction and valence bands at k in reciprocal space. $f_{CV}(k)$ is the intensity of the transition. $\mu = m_e m_h / (m_e + m_h)$ is the reduced mass of the e-h pair. $\hbar$ represents Planck constant. For an indirect band gap transition[282]

$$\varepsilon''(\omega) = A'(T)(\hbar\omega - E_G)^2 \tag{8.6}$$

where $A'(T)$ containing parameters for the band structure and temperature describe the momentum contribution of phonons to the indirect band gap transition. Considering $\hbar\omega << E_G$ in the frequency range of 50 Hz–1.0 MHz and fitting of the experimental data of imaginary permittivity [Figure 8.5(b)] based on the assumption of universal dynamic law,[283] the equation above can be expressed as

$$\begin{aligned} \varepsilon''(\omega) &= A'(T)\omega^\alpha E_G{}^2, \\ &= B'(T)\omega^\alpha. \end{aligned} \tag{8.7}$$

The exponent α is about –0.86 after averaging the calculated exponents at different temperatures. The correlation between $B'(T)$ and the temperature is plotted in Figure 8.6. It can be observed that there is also a transition at about 561 K which is very similar to the curve of the conduction transition. $B'(T)$ is subsequently expressed in exponential form as $B'(T) = B_0 \exp(-\beta/T)$. The coefficient β increases from 2.4×10^2 to 3.0×10^3 K^{-1} and B_0 from 8.8×10^2 to 1.2×10^5 at the equilibration temperature. The transition typically suggests the presence of specific polarization phenomenon: lattice and electronic polarization associated to band tail

ATTENTION: The Singapore Copyright Act applies to the use of this document. Nanyang Technological University Library

hopping, which contributes to the rapid rise of real and imaginary permittivity above the equilibration temperature. Electron–lattice phonon interaction allows the charge to locally distort the lattice around it and subsequently trap itself in the resulting potential well, which results in the polaron formation. [284] Moreover, weakening of the crystal field induced by lattice thermal expansion may also contribute to this permittivity transition because lattice thermal expansion can decrease the E_G[36] correlated to the permittivity of semiconductors, [115,285,71].

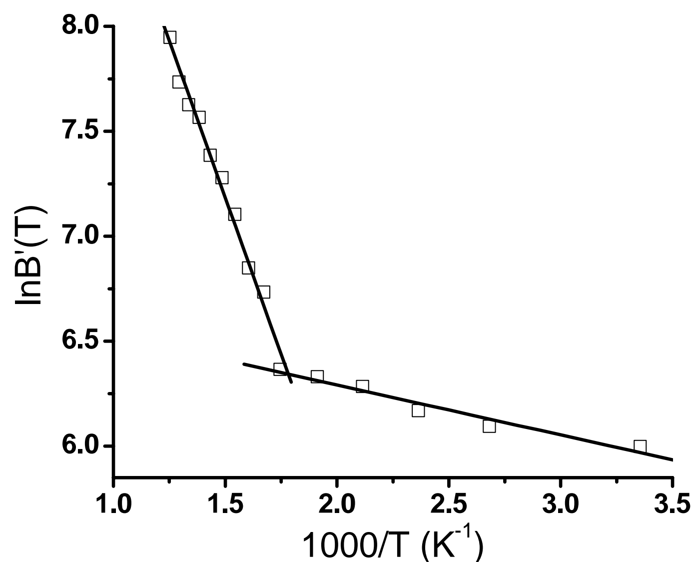

Figure 8.6 Plot of $B'(T)$ vs $1000/T$ with a transition at about 561 K. (from Ref. 187)

8.4 Summary

The temperature dependence of the complex dielectric behavior of PS exhibits a semicircle in the high frequency region, followed by an intermediate and a lowest frequency depressed semicircle. These features are attributed to the grain interior,

ATTENTION: The Singapore Copyright Act applies to the use of this document. Nanyang Technological University Library

grain boundary, and electrode/film interface contributions. The dielectric transition takes place from dominance of the grain interior to dominance of the grain boundary at about 673 K and then to dominance of the electrode/film interface at about 773 K. The activation energy transition from 0.07 to 0.79 eV at the equilibration temperature, about 565 K is suggested to be the effect of band tail hopping that occurs around the Fermi edge. When the temperature is raised to this critical temperature, a high degree of dispersion in the real and imaginary parts of the permittivity also occurs at low frequencies. This dispersion behavior is interpreted as a combination of electron-lattice polarization associated to band tail hopping and crystal field weakening due to thermal expansion.

ATTENTION: The Singapore Copyright Act applies to the use of this document. Nanyang Technological University Library

Chapter 9 Conclusions and Recommendations

9.1 Conclusions

The optical and dielectric properties of nanosolid silicon have been investigated and experimental results show that (1) PL and PA blue-shift, Raman red-shift, E_G expansion, Si-2*p* level blue-shift as well as dielectric suppression occur when the nanosolid size is reduced. (2) CF_4 plasma-passivation further enhances the size dependence of the blue-shift in PL, PA and Si-2*p* level, of the E_G expansion, and of the dielectric suppression. (3) Dielectric impedance measurements by impedance spectroscopy within the frequency range of 50 Hz–1.0 MHz and temperature range of 298–798 K reveal three semicircles in a Cole–Cole plot when the temperature is raised to 773 K. The enhancement in conductivity by heating follows an Arrhenius law with an activation energy transition from 0.07 to 0.79 eV at ~565 K.

We presented a new approach based on the *BOLS* correlation premise that is not only able to converge the theoretical prediction to the experimental results but also able to deepen our insight into the physical origin of PL and PA blue-shift, e-p interaction, Raman red-shift, E_G expansion, Si-2*p* level blue-shift, as well as dielectric suppression by the nanosolid formation. Differing from the currently available theories, the present model, without any assumption or freely adjustable parameters, emphasizes that E_G expansion, Raman red-shift, and core level shift relate to the Hamiltonian that is subject to the modification by surface *CN*-imperfection and its effect on the binding energy density in the relaxed region, and

ATTENTION: The Singapore Copyright Act applies to the use of this document. Nanyang Technological University Library

the PL and PA blue-shifts and dielectric suppression relate directly to the crystal binding density and the e-p coupling. Most strikingly, single energy level of the 2*p* electrons (–96.74 eV) of an *isolated* Si atom and vibration frequency (502.3 cm^{-1}) of a Si–Si dimer bond and their shift upon bulk and nanosolid formation have been quantified by matching predictions to the observed size and shape dependence of the XPS and Raman data, which are beyond the scope of currently available approaches.

9.2 Recommendations for Further Research

- To further develop the model in terms of size effect and surface passivation effect on optical and dielectric properties of PS.
- To explore the applications of PS on sensors.

ATTENTION: The Singapore Copyright Act applies to the use of this document. Nanyang Technological University Library

Author's Publications

1. **L. K. Pan**, C. Q. Sun, B. K. Tay, T. P. Chen, and S. Li, The Journal of Physical Chemistry B **106**, 11725 (2002), *"Photoluminescence of Si Nanosolids near the Lower End of the Size Limit"*.

2. **L. K. Pan**, H. T. Huang, and C. Q. Sun, Journal of Applied Physics **94**, 2695 (2003), *"Dielectric Relaxation and Transition of Porous Silicon"*.

3. **L. K. Pan** and C. Q. Sun, Journal of Applied Physics **95**, 3819 (2004), *"Coordination Imperfection Enhanced Electron-Phonon Interaction in Porous Silicon"*.

4. **L. K. Pan**, Y. K. Ee, C. Q. Sun, G. Q. Yu, Q. Y. Zhang, and B. K. Tay, Journal of Vacuum Science and Technology B **22**, 583 (2004), "*Band-Gap Expansion, Core-Level Shift and Dielectric Suppression of Porous Silicon Passivated by Plasma Fluorination*".

5. **L. K. Pan**, C. Q. Sun and C. M. Li, The Journal of Physical Chemistry B **108**, 3404 (2004), "*Elucidating Si-Si dimer vibration from the size-dependent Raman shift of nanosolid Si*"

6. **L. K. Pan**, C. Q. Sun, G. Q. Yu, Q. Y. Zhang, Y. Q. Fu, and B. K. Tay, Journal of Applied Physics **96**, 1704 (2004), "*Distinguishing the Effect of Surface Passivation from the Effect of Size on the Photonic and Electronic Behavior of Porous Silicon*"

ATTENTION: The Singapore Copyright Act applies to the use of this document. Nanyang Technological University Library

7. **L. K. Pan**, C. Q. Sun, and C. M. Li, Applied Surface Sciences **240**,19 (2004), "*Estimating the extent of surface oxidation by measuring the porosity dependent dielectrics of oxygenated porous silicon*"

8. **L. K. Pan**, C. Q. Sun, T. P. Chen, S. Li, C. M. Li, and B. K. Tay, Nanotechnology **15**, 1802 (2004), "*Dielectric Suppression of Nansolid Silicon*"

9. C. Q. Sun, **L. K. Pan**, Y. Q. Fu, B. K. Tay, and S. Li, The Journal of Physical Chemistry B **107**, 5113 (2003), *"Size Dependence of the 2p-Level Shift of Nanosolid Silicon".*

10. C. Q. Sun, **L. K. Pan**, H. L. Bai, Z. Q. Li, P. Wu, and E. Y. Jiang, Acta Materialia **51**, 4631 (2003), *"Effects of Surface Passivation and Interfacial Reaction on the Size-Dependent 2p-Level shift of SupportedCopper Nanosolids".*

11. C. Q Sun, T. P. Chen, B. K. Tay, S. Li, H. Huang, Y. B. Zhang, **L. K. Pan**, S. P. Lau, and X. W. Sun, Journal of Physics D: Applied Physics **34**, 3470 (2001), *"An Extended 'Quantum Confinement' Theory: Surface-Coordination Imperfection Modifies the Entire Band Structure of a Nanosolid".*

ATTENTION: The Singapore Copyright Act applies to the use of this document. Nanyang Technological University Library

Bibliography

[1] A. Uhlir, Bell Syst. Tech. J. **35**, 333 (1956). "*Electronic shaping of germanium and silicon*"

[2] C. S. Fuller and J. A. Ditzenberger, J. Appl. Phys. **27**, 544 (1957). "*Diffusion of donor and acceptor element in silicon*"

[3] D. R. Turner, J. Electrochem. Soc. **105**, 402 (1958). "*Electropolishing silicon in HF acid solutions*"

[4] R. J. Archer, J. Phys. Chem. Solids **14**, 104 (1960). "*Measurement of oxygen adsorption on silicon by ellipsometry*"

[5] Y. Watanabe and T. Sakai, Rev. Electron. Commun. Labs. **19**, 899 (1971). "*Application of a thick anode film to semiconductor devices*"

[6] Y. Watanabe, Y. Arita, T. Yokoyama, and Y. Igarashi, J. Electrochem. Soc. **122**, 1351 (1975). "*Formation and properties of porous silicon and its application*"

[7] T. Unagami and K. Kato, Jpn. J. Appl. Phys. **16**, 1635 (1977). "*Study of the injection type IPOS scheme*"

[8] K. Imai and Y. Yoriume, Jpn. J. Appl. Phys. **18**, 281 (1979).

[9] K. Imai, Solid-State Electron. **24**, 159 (1981). "*A new dielectric isolation method using porous silicon*"

[10] K. Barla, G. Bomchil, R. Herino, A. Monroy, and Y. Gris, Electron. Lett. **22**, 1291 (1986). "*Characteristics of SOL CMOS circuits made in n/n/sup +//n oxidised porous silicon structures*"

[11] S. S. Tsao, D. R. Myers, and G. K. Celler, Electron. Lett. **24**, 238 (1988). "*Gate coupling and floating-body effects in thin-film SOI MOSFETs*"

ATTENTION: The Singapore Copyright Act applies to the use of this document. Nanyang Technological University Library

[12] N. J. Thomas, J. R. Davis, J. M. Keen, J. G. Castledine, D. Brumhead, M. Goulding, J. Alderman, J. P. G. Farr, L. G. Earwaker, J. L. Ecuyer, I. M. Sturland, and J. M. Cole, IEEE Electron Device Lett. **10**, 129 (1989). "*High-performance thin-film silicon-on-insulator CMOS transistors in porous anodized silicon*"

[13] G. Bomchil, A. Halimaoui, and R. Herino, Appl. Surf. Sci. **41/2**, 604 (1989). "*Porous silicon: the material and its applications in silicon-on-insulator technologies*"

[14] L. T. Canham, Appl. Phys. Lett. **57**, 1046 (1990). "*Silicon quantum wire array fabrication by electrochemical and chemical dissolution of wafers*"

[15] V. Lehmann and U. Gösele, Appl. Phys. Lett. **58**, 856 (1991). "*Porous silicon formation: A quantum wire effect*"

[16] L. T. Canham, Phys. World **5**, 41 (1992). "*Silicon optoelectronics at the end of the rainbow*?"

[17] A. Halimaoui, C. Oules, G. Bromchil, A. Bsiesy, F. Gaspard, R. Herino, M. Ligeon, and F. Muller, Appl. Phys. Lett. **59**, 304 (1991). "*Electroluminescence in the visible range during anodic oxidation of porous silicon films*"

[18] E. Corcoran, Sci. Am. July, 108 (1991); I. Amato, Science **252**, 922 (1991). "*Shine on, holey silicon*"

[19] J. P. Proot, C. Delerue, and G. Allan, Appl. Phys. Lett. **61**, 1948 (1992). "*Electronic structure and optical properties of silicon crystallites: Application to porous silicon*"

[20] F. Buda, J. Kohanoff, and M. Parrinello, Phys. Rev. Lett. **69**, 1272 (1992). "*Optical properties of porous silicon: A first-principles study*"

ATTENTION: The Singapore Copyright Act applies to the use of this document. Nanyang Technological University Library

[21] G. D. Sanders and Y. C. Chang, Appl. Phys. Lett. **60**, 2525 (1992). "*Optical properties of free-standing silicon quantum wires*"

[22] C. Delerue, G. Allan, and M. Lannoo, Phys. Rev. B **48**, 11024 (1993). "*Theoretical aspects of the luminescence of porous silicon*"

[23] Phys. Today **45** (10) (1992).

[24] L. Banyai and S. W. Koch, *Semiconducotr Quantum Dots* (World Scientific, Singapore, 1993).

[25] J. Tersoff and R. S. Ruoff, Phys. Rev. Lett. **73**, 676 (1994). "*Structural properties of a carbon-nanotube crystal*"

[26] S. Veprek and A. S. Argon, J. Vac. Sci. Technol. B **20,** 650 (2002). "*Towards the understanding of mechanical properties of super- and ultrahard nanocomposites*"

[27] L. Lu, M. L. Sui, and K. Lu, Science **287**, 1463 (2000). "*Superplastic extensibility of nanocrystalline copper at room temperature*"

[28] H. K. Christenson, J. Phys. Condens. Matter. **13**, R95 (2001). "*Confinement effects on freezing and melting*"

[29] S. Mintova, N. H. Olson, V. Valtchev, and T. Bein, Science **283**, 958 (1999). "*Mechanism of zeolite a nanocrystal growth from colloids at room temperature*"

[30] C. T. Campbell, S. C. Parker, and D. E. Starr, Science **298**, 811 (2002). "*The effect of size-dependent nanopartilce energetics on catalyst sintering*"

[31] S. Horch, H. T. Lorensen, S. Helveg, E. Laegsgaard, I. Stensgaard, K. W. Jacobsen, J. K. Norskov, and F. Besenbacher, Nature **398**, 134 (1999). "*Enhancement of surface self-diffusion of platinum atoms by adsorbed hydrogen*"

ATTENTION: The Singapore Copyright Act applies to the use of this document. Nanyang Technological University Library

[32] T. van Buuren, L. N. Dinh, L. L. Chase, W. J. Siekhaus, and L. J. Terminello, Phys. Rev. Lett. **80**, 3803 (1998). "*Changes in the electronic properties of Si nanocrystals as a function of particle size*"

[33] A. D. Yoffe, Adv. Phys. **50**, 1 (2001). "*Semiconductor quantum dots and related systems: electronic, optical, luminescence and related properties of low dimensional systems*"; A. D. Yoffe, Adv. Phys. **51**, 799 (2002). "*Low-dimensional systems: quantum size effects and electronic properties of semiconductor microcrystallites (zero-dimensional systems) and some quasi-two-dimensional systems*"

[34] O. K. Tan, W. Zhu, Q. Yan, and L. B. Kong, Sensor. Actuat. B **65**, 361 (2000). "*Size effect and gas sensing characteristics of nanocrystalline* $xSnO_2(1-x)\alpha$-Fe_2O_3 *ethanol sensors*"

[35] C. N. R. Rao, G. U. Kulkarni, P. J. Thomas, and P. P. Edwards, Chem-European J. **8**, 29 (2002). "*Size-dependent chemistry: properties of nanocrystals*"

[36] C. Q. Sun, T. P. Chen, B. K. Tay, S. Li, H. Huang, Y. B. Zhang, L. K. Pan, S. P. Lau, and X. W. Sun, J. Phys. D **34**, 3470 (2001). "*An extended 'quantum confinement' theory: surface-coordination imperfection modifies the entire band structure of a nanosolid*"

[37] C. Q. Sun, Phys. Rev. B **69**, 045105 (2004). "*Surface and nanosolid core-level shift: Impact of atomic coordination number imperfection*"

[38] A. G. Cullis, L. T. Canham, and P. D. J. Calcott, J. Appl. Phys. **82**, 909 (1997). "*The structural and luminescence properties of porous silicon*"

ATTENTION: The Singapore Copyright Act applies to the use of this document. Nanyang Technological University Library

[39] R. W. Fathauer, T. George, A. Ksendzov, and R. P. Vasquez, Appl. Phys. Lett. **60**, 995 (1992). "*Visible luminescence from silicon wafers subjected to stain etches*"

[40] R. P. Vasquez, R. W. Fathauer, T. George, A. Ksendzov, and T. L. Lin, Appl. Phys. Lett. **60**, 1004 (1992). "*Electronic structure of light-emitting porous Si*"

[41] R. P. Vasquez, A. Madhukar, and J. A. R. Tanguay, J. Appl. Phys. **58**, 2337 (1985). "*Spectroscopic ellipsometry and x-ray photoelectron spectroscopy studies of the annealing behavior of amorphous Si produced by Si ion implantation*"

[42] M. J. Estes and G. Moddel, Phys. Rev. B **54**, 14633 (1996). "*Luminescence from amorphous silicon nanostructures*"

[43] L. Pavesi, Solid State Phenom. **44-46**, 261 (1995). "*Hydrogenated amorphous silicon*"

[44] P. D. J. Calcott, K. J. Nash, L. T. Canham, M. J. Kane, and D. Brumhead, J. Lumin. **57**, 257 (1993). "*Spectroscopic identification of the luminescence mechanism of highly porous silicon*"

[45] C. Tsai, K. H. Li, J. Sarathy, S. Shih, J. C. Campbell, B. K. Hance, and J. M. White, Appl. Phys. Lett. **59**, 2814 (1991). "*Thermal treatment studies of the photoluminescence intensity of porous silicon*"

[46] S. M. Prokes, O. J. Glembocki, V. M. Bermudez, R. Kaplan, L. E. Friedersdorf, and P. C. Searson, Phys. Rev. B **45**, 13788 (1992). "*SiH_x excitation: An alternate mechanism for porous Si photoluminescence*"

[47] D. J. Wolford, B. A. Scott, J. A. Reimer, and J. A. Bradley, Physica B **117&118**, 920 (1983). "*Efficient visible luminescence from hydrogenated amorphous-silicon*"

ATTENTION: The Singapore Copyright Act applies to the use of this document. Nanyang Technological University Library

[48] M. B. Robinson, A. C. Dillon, and S. M. George, Appl. Phys. Lett. **62**, 1493 (1993). "*Porous silicon photoluminescence versus HF etching: No correlation with surface hydrogen species*"

[49] V. Lehmann, H. Cerva, and U. Gösele, Mater. Res. Soc. Symp. Proc. **256**, 3 (1992). "*Light emission from silicon*"

[50] T. Ito, T. Ohta, O. Arakaki, and A. Hiraki, Mater. Res. Soc. Symp. Proc. **256**, 127 (1992). "*Optical properties of microcrystalline silicon in oxide matrix through partial oxidation of anodized porous silicon*"

[51] R. A. Street, *Hydrogenated amorphous silicon* (Cambridge University Press, Cambridge, 1991).

[52] G. G. Qin and Y. Q. Jia, Solid State Commun. **86**, 559 (1993). "*Mechanism of the visible luminescence in porous silicon*"

[53] S. M. Prokes, Appl. Phys. Lett. **62**, 3244 (1993). "*Light emission in thermally oxidized porous silicon: Evidence for oxide-related luminescence*"

[54] M. A. Tischler and R. T. Collins, Solid State Commun. **84**, 819 (1992). "*On the relationship of porous silicon and siloxene*"

[55] Z. Y. Xu, M. Gal, and M. Gross, Appl. Phys. Lett. **60**, 1375 (1992). "*Photoluminescence studies on porous silicon*"

[56] M. S. Brandt, H. D. Fuchs, M. Stutzmann, J. Weber, and M. Cardona, Solid State Commun. **81**, 307 (1997). "*The origin of visible luminescence from "porous silicon": A new interpretation*"

[57] T. K. Sham, D. T. Jang, I. Coulthard, J. W. Lorimer, X. H. Feng, K. H. Tang, S. P. Frigo, R. A. Rosenberg, D. C. Houghton, and B. Bryskiewicz, Nature **363**, 331

ATTENTION: The Singapore Copyright Act applies to the use of this document. Nanyang Technological University Library

(1993). "*Origin of luminescence from porous silicon deduced by synchrotron-light-induced optical luminescence*"

[58] F. Koch, V. Petrova-Koch, T. Muschik, A. Nikolov, and V. Gavrilenko, Mater. Res. Soc. Symp. Proc. **283**, 197 (1993). "*Some perspectives on the luminescence mechanism via surface-confined states of porous Si*"

[59] J. E. Brus, J. Lumin. **31-32**, 381 (1984). "*On the development of bulk optical properties in small semiconductor crystallites*"

[60] Y. Kayanuma, Phys. Rev. B **38**, 9797 (1988). "*Quantum-size effects of interacting electrons and holes in semiconductor microcrystals with spherical shape*"

[61] N. Kalkhoran, F. Namavar, and H. P. Maruska, Appl. Phys. Lett. **63**, 2661 (1993). "*Optoelectronic applications of porous polycrystalline silicon*"

[62] H. Fu and A. Zunger, Phys. Rev. B **55**, 1642 (1997). "*Local-density-derived semiempirical nonlocal pseudopotentials for InP with applications to large quantum dots*"

[63] V. Albe, C Jouanin, and D Bertho, Phys. Rev. B **58**, 4713 (1998). "*Confinement and shape effects on the optical spectra of small CdSe nanocrystals*"

[64] O. I. Micic, J. Sprague, Z. Lu, and A. J. Nozik, Appl. Phys. Lett. **68**, 3150 (1996). "*Highly efficient band-edge emission from InP quantum dots*"

[65] Y. Kanemitsu, H. Uto, Y. Masumoto, T. Matsumoto, T. Futagi, and H. Mimura, Phys. Rev. B **48**, 2827 (1993). "*Microstructure and optical properties of free-standing porous silicon films: Size dependence of absorption spectra in Si nanometer-sized crystallites*"

ATTENTION: The Singapore Copyright Act applies to the use of this document. Nanyang Technological University Library

[66] Y. D. Glinka, S. Lin, L.-P. Hwang, Y.-T. Chen, and N. H. Tolk, Phys. Rev. B **64**, 085421 (2001). "*Size effect in self-trapped exciton photoluminescence from* SiO_2*-based nanoscale materials*"

[67] L. Pauling, J. Am. Chem. Soc. **69**, 542 (1947). "*Atomic radii and interatomic distances in metals*"

[68] V. M. Goldschmidt, Ber. Deut. Chem. Ges. **60**, 1270 (1927).

[69] C. Q. Sun, B. K. Tay, S. P. Lau, X. W. Sun, X. T. Zeng, H. Bai, H. Liu, Z. H. Liu, and E. Y. Jiang, J. Appl. Phys. **90**, 2615 (2001). "*Bond contraction and lone pair interaction at nitride surfaces*"

[70] C. Q. Sun, X. W. Sun, H. Q. Gong, H. Huang, H. Ye, D. Jin, and P. Hing, J. Phys. Condens. Matter. **11**, L547 (1999). "*Frequency shift in the photoluminescence of nanostructured* SiO_x*: surface bond contraction and oxidation*"

[71] C. Q. Sun, X. W. Sun, B. K. Tay, S. P. Lau, H. Huang, and S. Li, J. Phys. D. **34**, 2359 (2001). "*Dielectric suppression and its effect on photoabsorption of nanometric semiconductors*"

[72] S. Schuppler, S. L. Friedman, M. A. Marcus, D. L. Adler, Y. H. Xie, F. M. Ross, Y. J. Chabal, T. D. Harris, L. E. Brus, W. L. Brown, E. E. Chaban, P. F. Szajowski, S. B. Christman, and P. H. Citrin, Phys. Rev. B **52**, 4910 (1995). "*Size, shape, and composition of luminescent species in oxidized Si nanocrystals and H-passivated porous Si*"

[73] P. J. Feibelman, Phys. Rev. B **53**, 13740 (1996). "*Relaxation of hcp(0001) surfaces: A chemical view*"

ATTENTION: The Singapore Copyright Act applies to the use of this document. Nanyang Technological University Library

[74] L. K. Pan, C. Q. Sun, B. K. Tay, T. P. Chen, and S. Li, J. Phys. Chem. B **106**, 11725, (2002). "*Photoluminescence of Si nanosolid near the lower end of the size limit*"

[75] T. Halicioglu, Surf. Sci. **259**, L714 (1991). "*Calculation of surface energies for low index planes of diamond*"

[76] C. Q. Sun, Vacuum **48**, 535 (1997). "*Exposure-resolved VLEED from the O-Cu(001): bonding dynamics*"

[77] S. R. Bahn and K. W. Jaconsen, Phys. Rev. Lett. **87**, 266202 (2001). "*Chain formation of mMetal atoms*"

[78] C. Q. Sun, J. Phys. Condens. Matter. **11**, 4801 (1999). "*The lattice contraction of nanometre-sized Sn and Bi particles produced by an electrohydrodynamic technique*"

[79] C. Q. Sun, H. Q. Gong, P. Hing, and H. T. Ye, Surf. Rev. Lett. **6**, L171 (1999). "*Behind the quantum confinement and surface passivation of nanoclusters*"

[80] H. Huang, C. Q. Sun, and P. Hing, J. Phys. Condens. Matter. **12**, L127 (2000). "*Surface bond contraction and its effect on the behavior of nanometric PZT*"

[81] H. Huang, C. Q. Sun, T. S. Zhang, and P. Hing, Phys. Rev. B **63**, 184112 (2001). "*Grain-size effect on ferroelectric Pb(Zr_{1-x}Tix)O3 solid solutions induced by surface bond contraction*"

[82] M. A. Omar, *Elementary Solid State Physics: Principles and Applications* (Addison-Wesley, New York, 1975), p. 253.

[83] Q. Zhang and S. C. Bayliss, J. Appl. Phys. **79**, 1351 (1996). **"***The correlation of dimensionality with emitted wavelength and ordering of freshly produced porous silicon***"**

ATTENTION: The Singapore Copyright Act applies to the use of this document. Nanyang Technological University Library

[84] F. Koch, V. Petrova-Koch, and T. Muschik, J. Lumin. **57**, 271 (1993). "*The luminescence of porous Si: the case for the surface state mechanism*"

[85] G. Allan, C. Delerue, and M. Lannoo, Phys. Rev. Lett. **76**, 2961 (1996). "*Nature of luminescent surface states of semiconductor nanocrystallites*"

[86] C. Q. Sun, B. K. Tay, X. T. Zeng, S. Li, T. P. Chen, J. Zhou, H. L. Bai, and E. Y. Jiang, J. Phys. Condens. Matter. **14**, 7781 (2002). "*Bond-order-length-strength (Bond-OLS) correlation mechanism for the shape and size dependency of a nanosolid*"

[87] Q. Jiang, Z. Zhang, and J. C. Li, Chem. Phys. Lett. **322**, 549 (2000). "*Superheating of nanocrystals embedded in matrix*"

[88] F. G. Shi, J. Mater. Res. **9**, 1307 (1994). "*Size dependent thermal vibrations and melting in nanocrystals*"

[89] A. Kux and M. B. Chorin, Phys. Rev. B **51**, 17535 (1995). "*Band gap of porous silicon*"

[90] G. D. Sanders and Y. C. Chang, Phys. Rev. B **45**, 9202 (1992). "*Theory of optical properties of quantum wires in porous silicon*"

[91] X. Wang, D. M. Huang, L. Ye, M. Yang, P. H. Hao, H. X. Fu, X. Y. Hou, and X. D. Xie, Phys. Rev. Lett. **71**, 1265 (1993). "*Pinning of photoluminescence peak positions for light-emitting porous silicon: An evidence of quantum size effect*"

[92] L. Dorigoni, O. Bisi, F. Bernardini, and S. Ossicini, Phys. Rev. B **53**, 4557 (1996). "*Electron states and luminescence transition in porous silicon*"

[93] M. S. Hybertsen and M. Needels, Phys. Rev. B **48**, 4608 (1993). "*First-principles ananlysis of electronic states in silicon nanoscale quantum wires*"

ATTENTION: The Singapore Copyright Act applies to the use of this document. Nanyang Technological University Library

[94] T. Ohno, K. Shiraishi, and T. Ogawa, Phys. Rev. Lett. **69**, 2400 (1992). "*Intrinsic origin of visible light emission from silicon quantum wires: Electronic structure and getometrically restricted exciton*"

[95] C. Y. Yeh, S. B. Zhang, and A. Zunger, Phys. Rev. B **50**, 14405 (1994). "*Confinement, surface, and chemisorption effects on the optical properties of Si quantum wires*"

[96] A. J. Read, R. J. Needs, K. J. Nash, L. T. Canham, P. D. J. Calcott, and A. Qteish, Phys. Rev. Lett. **69**, 1232 (1992). "*First-principles calculations of the electronic properties of silicon quantum wires*"

[97] H. M. Polatoglou, J. Lumin **57**, 117 (1993). "*Optical properties of H terminated Si quantum wires*"

[98] C. Delerue, M. Lannoo, and G. Allan, in: L. T. Canham (Ed.), *Properties of Porous Silicon* (IEE INSPEC, The Institution of Electrical Engineers, London, 1997), p. 212. "*Porous silicon modeled as idealized quantum dots*"

[99] S. Furukawa and T. Miyasato, Phys. Rev. B **38**, 5726 (1988). "*Quantum size effects on the optical band gap of microcrystalline Si:H*"

[100] J. von Behren, T. van Buuren, M. Zacharias, E. H. Chimowitz, and P. M. Fauchet, Solid State Commun. **105**, 317 (1998). "*Quantum confinement in nanoscale silicon: The correlation of size with bandgap and luminescence*"

[101] L. K. Pan and C. Q. Sun, J. Appl. Phys. **95**, 3819 (2004), "*Coordination imperfection enhanced electron-phonon interaction in porous silicon*".

[102] K. Borgohain, J. B. Singh, M. V. R. Rao, T. Shripathi, and S. Mahamuni, Phys. Rev. B **61**, 11093 (2000). "*Quantum size effects in CuO nanoparticles*"

ATTENTION: The Singapore Copyright Act applies to the use of this document. Nanyang Technological University Library

[103] D. Q. Yang and E. Sacher, Appl. Surf. Sci. **195**, 187 (2002). "*Initial- and final-state effects on metal cluster/substrate interactions, as determined by XPS: copper clusters on Dow Cyclotene and highly oriented pyrolytic graphite*"

[104] T. Ohgi and D. Fujita, Phys. Rev. B **66**, 115410 (2002). "*Consistent size dependency of core-level binding energy shifts and single-electron tunneling effects in supported gold nanoclusters*"

[105] D. Schmeißer, O. Böhme, A. Yafantis, T. Heller, D. R. Batcherlor, I. Lundstrom, and A. L. Spetz, Phys. Rev. Lett. **83**, 380 (1999). "*Dipole moment of nanoparticles at interfaces*"

[106] M. Aldén, H. L. Skriver, and B. Johansson, Phys. Rev. Lett. **71**, 2449 (1993). "*Ab initio surface core-level shifts and surface segregation energies*"

[107] E. Navas, K. Starke, C. Laubschat, E. Weschke, G. Kaindl, Phys. Rev. B **48**, 14753 (1993). "*Surface core-level shift of 4f states for Tb(0001)*"

[108] W. D. Phillips, Rev. Mod. Phys. **70**, 721 (1998). "*Laser cooling and trapping of neutral atoms*"

[109] L.-W. Wang and A. Zunger, Phys. Rev. Lett. **73**, 1039 (1994). "*Dielectric constants of silicon quantum dots*"

[110] J. P. Walter and M. L. Cohen, Phys. Rev. B **2**, 1821 (1970). "*Wave-vector-dependent dielectric function for Si, Ge, GaAs, and ZnSe*"

[111] D. R. Penn, Phys. Rev. B **128**, 2093 (1962). "*Wave-number dependent dielectric function of semiconductors*"

[112] R. Tsu and D. Babic, Appl. Phys. Lett. **64**, 1806 (1994). "*Doping of a quantum dot*"

ATTENTION: The Singapore Copyright Act applies to the use of this document. Nanyang Technological University Library

[113] T. P. Chen, Y. Liu, M. S. Tse, O. K. Tan, P. F. Ho, K. Y. Liu, D. Gui, and A. L. K. Tan, Phys. Rev. B **68**, 153301 (2003). "*Dielectric functions of Si nanocrystals embedded in a SiO_2 matrix*"

[114] C. Delerue, M. Lannoo, and G. Allan, Phys. Rev. B **68**, 115411 (2003). "*Concept of dielectric constant for nanosized systems*"

[115] N. Koshida, in: L. T. Canham, *Properties of Porous Silicon* (INSPEC, London, 1997), p.234. "*Dielectric Constant of Porous Silicon*"

[116] M. A. Omar, *Elementary Solid State Physics: Principles and Applications* (Addison-Wesley, New York, 1975), p. 403.

[117] D. L. Greenway and G. Harbeke, *Optical Properties and Band Structure of Semiconductors* (Pergamon Press, New York, 1968).

[118] F. G. Brown, *The Physics of Solids* (Benjamin Press, New York, 1968).

[119] T. Takagahara, Phys. Rev. Lett. **71**, 3577 (1993). "*Electron-phonon interactions and excitonic dephasing in semiconductor nanocrystals*"

[120] J. Zi, H. Büscher, C. Falter, W. Ludwig, K. M. Zhang, and X. D. Xie, Appl. Phys. Lett. **69**, 200 (1996). "*Raman shifts in Si nanocrystals*"

[121] M. Fujii, Y. Kanzawa, S. Hayashi, and K. Yamamoto, Phys. Rev. B **54**, R8373 (1996). "*Raman scattering from acoustic phonons confined in Si nanocrystals*"

[122] Z. Iqbal and S. Veprek, J. Phys. C **15**, 377 (1982). "*Raman scattering from hydrogenated microcrystalline and amorphous silicon*"

[123] E. Anastassakis and E. Liarokapis, J. Appl. Phys. **62**, 3346 (1987). "*Polycrystalline Si under strain: Elastic and lattice-dynamical considerations*"

[124] H. Richter, Z. P. Wang, and L. Ley, Solid State Commun. **39**, 625 (1981). "*The one phonon Raman spectrum in microcrystalline silicon*"

ATTENTION: The Singapore Copyright Act applies to the use of this document. Nanyang Technological University Library

[125] I. H. Campbell and P. M. Fauchet, Solid State Commun. **58**, 739 (1986). "*The effects of microcrystal size and shape on the one phonon Raman spectra of crystalline semiconductors*"

[126] C. Q. Sun, Prog. Mater. Sci. **48**(6), 521 (2003). "*Oxidation electronics*"

[127] D. Papadimitriou, J. Bitsakis, J. M. López-Villegas, J. Samitier, and J. R. Morante, Thin Solid Films **349**, 293 (1999). "*Depth dependence of stress and porosity in porous silicon: a micro-Raman study*"

[128] J. L. Andújar, E. Bertran, A. Canillas, C. Roch, and J. L. Morenza, J. Vac. Sci. Technol. A **9**, 2216 (1991). "*Influence of pressure and radio frequency power on deposition rate and structural properties of hydrogenated amorphous silicon thin films prepared by plasma deposition*"

[129] N. Ohtani and K. Kawamura, Solid State Commun.**75**, 711 (1990). "*Theoretical investigation of Raman scattering from microcrystallites*"

[130] W. Cheng and S.-F. Ren, Phys. Rev. B **65**, 205305 (2002). "*Calculations on the size effects of Raman intensities of silicon quantum dots*"

[131] Y.-N. Hwang, S. Shin, H. L. Park, S.-H. Park, U. Kim, H. S. Jeong, E.-J. Shin, and D. Kim, Phys. Rev. B **54**, 15120 (1996). "*Effect of lattice contraction on the Raman shifts of CdSe quantum dots in glass matrices*"

[132] C. Q. Sun, S. Li, and B. K. Tay, Appl. Phys. Lett. **82**, 3568 (2003). *"Comment on "Laser-like mechanoluminescence in ZnMnTe-diluted magnetic semiconductor""*

[133] L. K. Pan, C. Q. Sun, and C. M. Li, J. Phys. Chem. B **108**, 3404 (2004). "*Elucidating Si-Si dimer vibration from the size-dependent Raman shift of Nanosolid Si*"

ATTENTION: The Singapore Copyright Act applies to the use of this document. Nanyang Technological University Library

[134] C. Pickering, M. I. J. Beale, D. J. Robbins, P. J. Pearson, and R. Greef, J. Phys. C **17**, 6535 (1984). "*Optical studies of the structure of porous silicon films formed in p-type degenerate and non-degenerate silicon*"; Thin Sold Films 125, 157 (1985). "*Optical properties of porous silicon films*"

[135] M. J. Eddowes, J. Electroananl. Chem. **280**, 297 (1990). "*Anodic dissolution of p- and n-type silicon; Kinetic study of the chemical mechanism*"

[136] B. R. Weinberger, G. G. Peterson, T. C. Eschrich, and H. A. Krasinski, J. Appl. Phys. **60**, 3232 (1986). "*Surface chemistry of HF passivated silicon: X-ray photoelectron and ion scattering spectroscopy results*"

[137] H. Ubara, T. Imura, and A. Hiraki, Solid State Commun. **50**, 673 (1984). "*Formation of Si-H bonds on the surface of microcrystalline silicon covered with SiO/sub x/ by HF treatment*"

[138] V. A. Burrows, Y. J. Chabal, G. S. Higashi, K. Raghavachari, and S. B. Christman, Appl. Phys. Lett. **53**, 998 (1988). "*Infrared spectroscopy of Si(111) surfaces after HF treatment: Hydrogen termination and surface morphology*"

[139] L. T. Canham, M. R. Houlton, W. Y. Leong, C. Pickering, and J. M. Keen, J. Appl. Phys. **70**, 422 (1991). "*Atmospheric impregnation of porous silicon at room temperature*"

[140] M. I. J. Beale, J. D. Benjamin, M. J. Uren, N. G. Chew, and A. G. Cullis, J. Crystal Growth **73**, 622 (1985). "*A experimental and theoretical study of the formation and microstructure of porous silicon*"

[141] R. L. Smith, S. F. Chuang, and S. D. Collins, J. Electron. Mater. **138**, 533 (1998). "*A theoretical model of the formation morphologies of porous silicon*"

ATTENTION: The Singapore Copyright Act applies to the use of this document. Nanyang Technological University Library

[142] A. Halimaoui, in: L. T. Canham (Ed.), *Properties of Porous Silicon* (IEE INSPEC, The Institution of Electrical Engineers, London, 1997), p. 17. "*Porous silicon formation by anodisation*"

[143] O. Belmont, D. Bellet, and Y. Bréchet, J. Appl. Phys. **79**, 7586 (1996). "*Study of the cracking of highly porous p+ type silicon during drying*"

[144] O. K. Andersen and E. Veje, Phys. Rev. B **53**, 15643 (1996). "*Experimental study of the energy-band structure of porous silicon*"

[145] E. Vazquez, J. Taguena-Martinez, L. E. Sansores, and C. Wang, J. Appl. Phys. **91**, 3085 (2002). "*Surface relaxation effects on the properties of porous silicon*"

[146] M. Thonissen, S. Billat, M. Kruger, H. Luth, M. Berger, U. Frotschen, and U. Rossow, J. Appl. Phys. **80**, 2990 (1996). "*Depth inhomogeneity of porous silicon layers*"

[147] J. J. Yon, K. Barla, R. Herino, and G. Bomchill, J. Appl. Phys. **62**, 1042 (1987). "*The kinetics and mechaism of oxide layer formation from porous silicon formed on p-Si substrates*"

[148] T. M. Bhave and S. V. Bhoraskar, J. Vac. Sci. Technol. B **16**, 2073 (1998). "*Surface work function studies in porous silicon*"

[149] B. D. Cullity, *Elements of X-ray Diffraction* (Addison-Wesley, Reading, MA 1956), p. 99.

[150] A. H. Mahan, J. Yang, S. Guha, and D. L. Williamson, Phys. Rev. B **61**, 1677 (2002). "*Structural changes in a-Si:H film crystallinity with high H dilution*"

[151] C. Q. Sun, S. Li, B. K. Tay, and T. P. Chen, Acta. Mater. **50**, 4687 (2002). "*Upper limit of blue shift in the photoluminescence of CdSe and CdS nanosolids*"

ATTENTION: The Singapore Copyright Act applies to the use of this document. Nanyang Technological University Library

[152] M. V. Wolkin, J. Jorne, and P. M. Fauchet, G. Allan, and C. Delerue, Phys. Rev. Lett. **82**, 197 (1999). "*Electronic states and luminescence in porous silicon quantum dots: The role of oxygen*"

[153] H. Yokomichi, H. Takakura, M. Kondo, and K. Morigaki, J. Non-Cryst. Solids **164/166**, 957 (1993). "*Nature of electron spin resonance centers in porous silicon*"

[154] H. Yokomichi, H. Nakagawa, M. Kondo, and K. Morigaki, Proc. 22nd Int. Conf. the Physics of Semiconductors, Vancouver, 1994, ed. D. J. Lockwood, World Scientific, 2177 (1995). "*Light-induced defects in porous silicon*"

[155] S. Gardelis and B. Hamilton, J. Appl. Phys. **76**, 5327 (1994). *"The effect of surface modification on the luminescence of porous silicon"*

[156] Z. H. Xiong, L. S. Liao, S. Yuan, Z. R. Yang, X. M. Ding, and X. Y. Hou, Thin Solid Films **388**, 271 (2001). "*Effects of O, H and N passivation on photoluminescence from porous silicon*"

[157] Y. Fan, J. Ju, W. Zhang, Y. Xia, Z. Wang, Z. Fang, and L. Wang, Solid State Commun. **120**, 435 (2001). *"A new passivation method for porous silicon"*

[158] A. Masuda, A. Morimoto, M. Kumeda, T. Shimizu, Y. Yonezawa, and T. Minamikawa, Appl. Phys. Lett. **61**, 816 (1992). "*Novel oxidation process of hydrogenated amorphous silicon utilizing nitrous oxide plasma*"

[159] A. Masuda, I. Fukushi, Y. Yonezawa, T. Minamikawa, A. Morimoto, M. Kumeda, and T. Shimizu, Jpn. J. Appl. Phys., Part 1 **32**, 2794 (1993). "*Spectroscopic study on N_2O-plasma oxidation of hydrogenated amorphous silicon and behavior of nitrogen*"

ATTENTION: The Singapore Copyright Act applies to the use of this document. Nanyang Technological University Library

[160] A. Masuda, Y. Yonezawa, A. Morimoto, and T. Shimizu, Jpn. J. Appl. Phys., Part 1 **34**, 1075 (1995). "*NH_3-plasma-nitridation process of (100) GaAs surface observed by angle-dependent x-ray photoelectron spectroscopy*"

[161] H. Yokomichi, A. Masuda, Y. Yonezawa, and T. Shimizu, Thin Solid Films **281-282**, 568 (1996). "*N_2–plasma-nitridation effects on porous silicon*"

[162] J. Charrier, M. Guendouz, L. Haji, and P. Robert, Phys. Stat. Sol. A **182**, 431 (2000). "*Porosity gradient resulting from localised formation of porous silicon: the effect on waveguiding*"

[163] L. A. Balagurov, D. G. Yarkin, G. A. Petrovicheva, E. A. Petrova, A. F. Orlov, and S. Ya. Andryushin, J. Appl. Phys. **82**, 4647 (1997). "*Highly sensitive porous silicon based photodiode structures*"

[164] H. Shinoda, T. Nakajima, K. Ueno, and N. Koshida, Nature **400**, 853 (1999). "*Thermally Induced Ultrasonic: Emission From Porous Silicon*"

[165] K. Kawakami, T. Fuji, S. Yae, and Y. Nakato, J. Phys. Chem. B **101**, 4508 (1997). "*Improvement in photovoltage and stability of porous n-Si electrodes coated with platinum by regulation of the thickness of nanoporous layers*"

[166] S. Ghosh, K. Hong, and C. Lee, Mat. Sci. Eng. B **96**, 53 (2002). "*Structural and physical properties of thin copper films deposited on porous silicon*"

[167] Y. H. Cheng, B. K. Tay, S. P. Lau, X. Shi, and H. S. Tan, J. Vac. Sci. Technol. A **19**, 2102 (2001). "*Influence of substrate bias on the microstructure and internal stress in Cu films deposited by Filtered Cathodic Vacuum Arc*"

[168] X. Shi, B. K. Tay, H. S. Tan, E. Liu, J. Shi, L. K. Cheah, and X. Jin, Thin Solid Films **345**, 1 (1999). "*Transport of vacuum arc plasma through an off-plane double bend filtering duct*"

ATTENTION: The Singapore Copyright Act applies to the use of this document. Nanyang Technological University Library

[169] E. J. Johnson, *Semiconductors and Semimetals*, Vol. 3 (Academic Press, New York, 1967), p 153.

[170] L. A. Balagurov, D. G. Yarkin, E. A. Petrova, A. F. Orlov, and S. N. Karyagin, Appl. Phys. Lett. **69**, 2852 (1996). "*Effects of vacuum annealing on the optical properties of porous silicon*"

[171] W. Theiss, *Scout Thin Film Analysis Software Handbook* (Aachen, Germany: M. Theiss– Hard- and Software for optical spectroscopy, www.mtheiss.com).

[172] W. Theiß, Surf. Sci. Rep. **29**, 91 (1997). "*Optical properties of porous silicon*"

[173] V. Lehmann, B. Jobst, T. Muschik, A. Kux, and V. Petrova-Koch, Jpn. J. Appl. Phys. **32**, 2095 (1993). "*Correlation between optical properties and crystallite size in porous silicon*"

[174] M. A. Butturi, M. C. Carotta, G. Martinelli, L. Passari, G. M. Youssef, A. Chiorino, and G. Ghiotti, Solid State Commun. **101**, 11 (1997). "*Effects of ageing on porous silicon photoluminescence: Correlation with FTIR and UV-Vis spectra*"

[175] S. Guha, P. Steiner, and W. Lang, J. Appl. Phys. **79**, 8664 (1996). "*Resonant Raman scattering and photoluminescence studies of porous silicon membranes*"

[176] P. M. Derlet, T. C. Choy, and A. M. Stoneham, J. Phys. Condens. Matter **7**, 2507 (1995). "*An investigation of the porous silicon optical absorption power law near the band edge*"

[177] N. Suzuki, T. Makino, Y. Yamada, T. Yoshida, and S. Onari, Appl. Phys. Lett. **76**, 1389 (2000). "*Structures and optical properties of silicon nanocrystallites prepared by pulsed-laser ablation in inert background gas*"

ATTENTION: The Singapore Copyright Act applies to the use of this document. Nanyang Technological University Library

[178] T. Makino, Y. Yamada, N. Suzuki, T. Yoshida, and S. Onari, J. Appl. Phys. **90**, 5075 (2001). "*Annealing effects on structures and optical properties of silicon nanostructured films prepared by pulsed-laser ablation in inert background gas*"

[179] T. Unagami, J. Electrochem. Soc. **127**, 476 (1980). "*Formation mechanism of porous silicon layer by anodization in hydrofluoric acid solution*"

[180] V. Lehmann, F. Hofmann, F. Möller, and U. Grüning, Thin Solid Films **255**, 20 (1995). "*Resistivity of porous silicon: a surface effect*"

[181] K. Miyata and D. L. Dreifus, Jpn. J. Appl. Phys., Part 1 **33**, 4526 (1994). "*Effect of annealing in air on electrical resistances of B-doped polycrystalline diamond films*"

[182] H. T. Ye, C. Q. Sun, and P. Hing, Thin Solid Films **381**, 52 (2001). "*Single semicircular response of dielectric properties of diamond films*"

[183] D. D. D. Ma, C. S. Lee, F. C. K. Au, S. Y. Tong, and S. T. Lee, Science **299**, 1874 (2003). "*Small-diameter silicon nanowire surfaces*"

[184] C. Q. Sun, L. K. Pan, Y. Q. Fu, B. K. Tay, and S. Li, J. Phys. Chem. B **107**, 5113 (2003). "*Size dependent 2p-level shift of nanosolid silicon*"

[185] F. Ferrieu, A. Hallimaoui, and D. Bensahel, Solid State Commun. **84**, 293 (1992). "*Optical characterisation of porous silicon layers by spectrometric ellipsometry in the 1.5–5 eV range*"

[186] H. Looyenga, Physica **31**, 401 (1965). "*Dielectric constants of heterogeneous mixtures*"

[187] L. K. Pan, H. T. Huang, and C. Q. Sun, J. Appl. Phys. **94**, 2695 (2003). "*Dielectric transition and relaxation of nanosolid silicon*"

[188] J. R. Macdonald, *Impedance Spectroscopy* (Wiley, New York, 1987), Chap. 4.

ATTENTION: The Singapore Copyright Act applies to the use of this document. Nanyang Technological University Library

[189] J. W. Orton and M. J. Powell, Rep. Prog. Phys. **43**, 1266 (1980). "*The Hall effect in polycrystalline and powdered semiconductors*"

[190] S. Lanfredi, J. F. Carvalho, and A. C. Hernandes, J. Appl. Phys. **88**, 283 (2000). "*Electric and dielectric properties of $Bi_{12}TiO_{20}$ single crystals*"

[191] M. Lannoo, C. Delerue, and G. Allan, Phys. Rev. Lett. **74**, 3415 (1995). "*Screening in semiconductor nanocrystallites and its consequences for porous silicon*"

[192] G. Viera, S. Huet, and L. Boufendi, J. Appl. Phys. **90**, 4175 (2001). "*Crystal size and temperature measurements in nanostructured silicon using Raman spectroscopy*"

[193] P. M. Fauchet and I. H. Campell, Crit. Rev. Solid State Mater. Sci. **14**, S79 (1988).

[194] A. K. Sood, K. Jayaram, D. Victor, and S. Muthu, J. Appl. Phys. **72**, 4963 (1992). "*Raman and high-pressure photoluminescence studies on porous silicon*"

[195] C. Ossadnik, S. Vepřek, and I. Gregora, Thin Solid Films **337**, 148 (1999). "*Applicability of Raman scattering for the characterization of nanocrystalline silicon*"

[196] G.-X. Cheng, H. Xia, K.-J. Chen, W. Zhang, and X.-K. Zhang, Phys. Stat. Sol. A **118**, K51 (1990).

[197] I. Mihalcescu, M. Ligeon, F. Muller, R. Romestain, and J.-C. Vial, J. Lumin. **57**, 111 (1993). "*Surface passivation: a critical parameter for the visible luminescence of electrooxidised porous silicon*"

[198] J. N. Chazalviel, F. Ozanam, and V. M. Dubin, J. Phys. (France) **4**, 1325 (1994).

ATTENTION: The Singapore Copyright Act applies to the use of this document. Nanyang Technological University Library

[199] L. Brus, Phys. Rev. B **53**, 4649 (1996). "*Model for carrier dynamics and photoluminescence quenching in wet and dry porous silicon thin films*"

[200] A. A. Filios, S. S. Hefner, and R. Tsu, J. Vac. Sci. Technol. B **14**, 3431 (1996). "*Correlation of Raman and optical studies with atomic force microscopy in porous silicon*"

[201] S. Bayliss, Q. Zhang, and P. Harris, Appl. Surf. Sci. **102**, 390 (1996). "*Network dimensionality of porous Si and Ge*"

[202] L. K. Pan, Y. K. Ee, C. Q. Sun, G. Q. Yu, Q. Y. Zhang, and B. K. Tay, J. Vac. Sci. Technol. B **22**, 583 (2004). "*Band-gap expansion, core-level shift, and dielectric suppression of porous silicon passivated by plasma fluorination*"

[203] B. M. Kostishko, S. V. Appolonov, and A. E. Kostishko, Appl. Surf. Sci. **189**, 113 (2002). "*Fluorine surface concentration change during the argon–oxygen ion treatment of porous silicon*"

[204] D. Petit, J. N. Chazalviel, F. Ozanam, and F. Devreux, Appl. Phys. Lett. **70**, 191 (1997). "*Porous silicon structure studied by nuclear magnetic resonance*"

[205] Y. Okada, J. Chen, I. H. Campbell, P. M. Fauchet, and S. Wagner, J. Non-Cryst. Solids **114**, 816 (1989). "*Mechanism of microcrystalline silicon growth from silicon tetrafluoride and hydrogen*"

[206] K. Baert, P. Deschepper, J. Nijs, and R. Mertens, Appl. Phys. Lett. **60**, 442 (1992). "*Selective Si epitaxial growth by plasma-enhanced chemical vapor deposition at very low temperature*"

[207] C. Ortega, J. Siejka, and G. Vizkelethy, Nucl. Instrum. Methods. Phys. Res. B **45**, 622 (1990). "*Characterization of porous silicon by NRA, RBS and channeling*"

ATTENTION: The Singapore Copyright Act applies to the use of this document. Nanyang Technological University Library

[208] C. Q. Sun, Appl. Phys. Lett. **72**, 1706 (1998). "*A model of bonding and band-forming for oxides and nitrides*"

[209] L. L. Wang, A. Zunger, Phys. Rev. Lett. **73**, 1039 (1994). "*Dielectric constants of silicon quantum dots*"

[210] L. K. Pan, C. Q. Sun, G. Q. Yu, Q. Y. Zhang, Y. Q. Fu, and B. K. Tay, J. Appl. Phys. **96**, 1704 (2004). "*Distinguishing the effect of surface passivation from the effect of size on the photonic and electronic behavior of porous silicon*"

[211] Y. Y. Li, F. Cunin, J. R. Link, T. Gao, R. E. Betts, S. H. Reiver, V. Chin, S. N. Bhatia, and M. J. Sailor, Science **299**, 2045 (2003). "*Polymer replicas of photonic porous silicon for sensing and drug delivery applications*"

[212] J. C. Maxwell-Garnett, Philos. Trans. R. Soc. London **203**, 385 (1904).

[213] D. A. G. Bruggeman, Ann. Phys. (Leipzig) **24**, 636 (1935). "*The calculation of various physical constants of heterogeneous substances. I. The dielectric constants and conductivities of mixtures composed of isotropic substances*"

[214] A. M. Campos, J. Torres, and J. J. Giraldo, Surf. Rev. Lett. **9**, 1631 (2002). "*Porous silicon dielectric function modeling from effective medium theories*"

[215] O. Teschke, Appl. Phys. Lett. **68**, 2129 (1996). "*Visualization of nanostructured porous silicon by a combination of transmission electron microscopy and atomic force microscopy*"; O. Teschke, F. Alvarez, L. Tessler, and M. U. Kleinke, Appl. Phys. Lett. **63**, 1927 (1993). "*Nanosize structures connectivity in porous silicon and its relation to photoluminescence efficiency*"

[216] H. Koyama, T. Nakagama, T. Ozaki, and N. Koshida, Appl. Phys. Lett. **65**, 1656 (1994). "*Post-anodization filtered illumination of porous silicon in HF solutions: An effective method to improve luminescence properties*"

ATTENTION: The Singapore Copyright Act applies to the use of this document. Nanyang Technological University Library

[217] P. V. Galiy, T. I. Lesiv, L. S. Monastyrskii, T. M. Nenchuk, and I. B. Olenych, Thin Solid Films **318**, 113 (1998). "*Surface investigations of nanostructured porous silicon*"

[218] S. Labbé-Lavigne, S. Barret, F. Garet, L. Duvillaret, and J. L. Coutaz, J. Appl. Phys. **83**, 6007 (1998). "*Far-infrared dielectric constant of porous silicon layers measured by terahertz time-domain spectroscopy*"

[219] L. V. Belyakov, T. L. Makarova, V. I. Sakharov, I. T. Serenkov, and O. M. Sreseli, Semiconductors **32**, 1003 (1998). "*Composition and porosity of multicomponent structures: porous silicon as a three-component system*"

[220] J. E. Lugo, H. A. Lopez, S. Chan, and P. M. Fauchet, J. Appl. Phys. **91**, 4966 (2002). "*Porous silicon multilayer structures: a photonic band gap analysis*"

[221] E. V. Astrova and V. A. Tolmachev, Mat. Sci. Eng. B **69-70**, 142 (2000). "*Effective refractive index and composition of oxidized porous silicon films*"

[222] C. Jin, J. D. Luttmer, D. M. Smith, and T. A. Ramos, MRS Bulletin **22**(10), 39 (1997). "*Nanoporous silica as an ultralow-k dielectrics*"

[223] X. Xiao, S. Reinhard, G. Ruan, R. Song, T. Otta, and T. Gessner, Microelectron. Eng. **54**, 295 (2000). "*Modelling and simulation for dielectric constant of aerogel*"

[224] P. A. Badoz, D. Bensahel, G. Bomchil, F. Ferrieu, A. Halimaoui, P. Perret, J. L. Regolini, I. Sagnes, and G. Vincent, Mater. Res. Soc. Symp. Proc. **283**, 97 (1993). "*Characterization of porous silicon: structural, optical and electrical properties*"

[225] M. Adam, Z. J. Horvath, I. Barsony, L. Szolgyemy, E. Vazsonyi, and V. V. Tuyen, Thin Solid Films **255**, 266 (1995). "*Investigation of electrical properties of Au/porous Si/Si structures*"

ATTENTION: The Singapore Copyright Act applies to the use of this document. Nanyang Technological University Library

[226] J. J. Si, H. Ono, K. Uchida, S. Nozaki, and H. Morisaki, Appl. Phys. Lett. **79**, 3140 (2001). "*Correlation between the dielectric constant and porosity of nanoporous silica thin films deposited by the gas evaporation technique*"

[227] L. W. Hrubesh, L. E. Keene, and V. R. Latorre, J. Mater. Res. **8**, 1736 (1993). "*Dielectric properties of aerogels*"

[228] S. Z. Yu, T. K. S. Wong, X. Hu, and K. Pita, J. Electrochem. Soc. **150**, F116 (2003). "*The effect of TEOS/MTES ratio on the structural and dielectric properties of porous silica films*"; J. Vac. Sci. Technol. B **20**, 2036 (2002). "*Synthesis of organically modified nesoporous silica as a low dielectric constant intermetal dielectric*"

[229] A. Loni, L. T. Canham, M. G. Berger, R. Arens-Fischer, H. Munder, H. Luth, H. F. Arrand, and T. M. Benson, Thin Solid Films **276**, 143 (1996). "*Porous silicon multilayer optical waveguides*"

[230] P. Basmaji, G. Surdutovich, R. Vitlina, J. Kolenda, V. S. Bagnato, H. Mohajeri-Moghaddam, and N. Peyhambarian, Solid State Commun. **91**, 649 (1994). "*Anisotropy investigations and photoluminescence properties of porous silicon*"

[231] I. Sagens, A. Halimaoui, G. Vincent, and P. A. Badoz, Appl. Phys. Lett. **62**, 1155 (1993). "*Optical absorption evidence of a quantum size effect in porous silicon*"

[232] C. Mazzoleni and L. Pavesi, Appl. Phys. Lett. **67**, 2983 (1995). "*Application to optical components of dielectric porous silicon multilayers*"

[233] E. V. Astrova, V. B. Voronkov, A. D. Remenyuk, V. B. Shuman, and V. A. Tolmachev, Semiconductors **33**, 1149 (1999). "*Variation of the parameters and

ATTENTION: The Singapore Copyright Act applies to the use of this document. Nanyang Technological University Library

composition of thin films of porous silicon as result of oxidation: ellipsometric studies"

[234] J. Charrier, E. Le. Gorju, L. Haji, and M. Guendouz, J. Porous Mat. **7**, 243 (2000). "*Optical waveguides fabricated from oxidised porous silicon*"

[235] L. V. Belyakov, T. L. Makarova, V. I. Sakharov, I. T. Serenkov, and O. M. Sreseli, Fizika i Tekhnika Poluprovodnikiv (in Russian) **32**, 1122 (1998). "*Composition and porosity of multicomponent structures: porous silicon as a ternary system*"

[236] R. J. Martín-Palma, J. Pérez-Rigueiro, and J. M. Martínez-Duart, J. Appl. Phys. **86**, 6911 (1999). "*Study of carrier transport in metal/porous silicon/Si structures*"

[237] F. A. Harraz, T. Tsuboi, J. Sasano, T. Sakka, and Y. H. Ogata, J. Electrochem. Soc. **149**, C456 (2002). "*Metal deposition onto a porous silicon layer by immersion plating from aqueous and nanaqueous solutions*"

[238] Z. A. Ansari, K. Hong, and C. Lee, Mat. Sci. Eng. B **90**, 103 (2002). "*Structural and electrical properties of porous silicon with rf-sputtered Cu films*"

[239] M. Jeske, J. W. Schultze, and R. Arens-Fischer, Thin Solid Films **255**, 63 (1995). "*Electrodeposition of metals into porous silicon*"

[240] Y. M. Huang, Appl. Phys. Lett. **69**, 2855 (1996). "*Photoluminescence of copper-doped porous silicon*"

[241] D. Andsager, J. Hilliard, and M. H. Nayfeh, Appl. Phys. Lett. **64**, 1141 (1994). "*Behavior of porous silicon emission spectra during quenching by immersion in metal ion solutions*"

ATTENTION: The Singapore Copyright Act applies to the use of this document. Nanyang Technological University Library

[242] D. Andsager, J. Hilliard, J. M. Hetrick, L. H. AbuHassan, M. Plisch, and M. H. Nayfeh, J. Appl. Phys. **74**, 4783 (1993). "*Quenching of porous silicon photoluminescence by deposition of metal adsorbates*"

[243] U. Labunov, V. Bondarenko, L. Glinenko, A. Dorofeev, and L. Tabulina, Thin Solid Films **137**, 123 (1986). "*Heat treatment effect on porous silicon*"

[244] M. De Crescenzi, Surf. Sci. **162**, 838 (1985). "*Extended energy loss fine structures (EELFS): A new structural probe for surfaces and interfaces*"

[245] T. Ito and A. Hiraki, Jpn. J. Appl. Phys. **26**, 1219 (1987). "*Stuffing of noble metals into anodized porous silicon by direct evaporation*"

[246] T. Yonehara, K. Sakaguchi, and N. Sato, Appl. Phys. Lett. **64**, 2108 (1994). "*Epitaxial layer transfer by bond and etch back of porous Si*"

[247] J. Pérez-Rigueiro, C. Jiménez, R. Pérez-Casero, and J. M. Martínez-Duart, J. Vac. Sci. Technol. B **14**, 2623 (1996). "*Nonlinear analysis of the I–V characteristics in Ti/Si and $TiSi_2$/Si Schottky diodes*"

[248] R. Hérino, Mat. Sci. Eng. B **69-70**, 70 (2000). "*Nanocomposite materials from porous silicon*"

[249] J. X. Shi, X. X. Zhang, M. L. Gong, J. Y. Zhou, K. W. Cheah, and W. K. Wong, Phys. Stat. Sol. A **182**, 353 (2000). "*Photoluminescence of erbium, zinc and copper doped porous silicon and a phenomenological model for the metal electrodeposition*"

[250] R. N. Hall and J. H. Racette, J. Appl. Phys. **35**, 379 (1964). "*Diffusion and solubility of copper in extrinsic and intrinsic germanium, silicon, and gallium arsenide*"

ATTENTION: The Singapore Copyright Act applies to the use of this document. Nanyang Technological University Library

[251] A. A. Istratov and E. R. Weber, J. Electrochem. Soc. **149**, G21 (2002). "*Physics of copper in silicon*"

[252] B. Meyer, D. Hofmann, W. Stadler, V. Petrova-Koch, F. Koch, P. Omling, and P. Emanuelsson, Appl. Phys. Lett. **63**, 2120 (1993). "*Defects in porous silicon investigated by optically detected and by electron paramagnetic resonance techniques*"

[253] F. Rong, J. Harvey, E. Pointdexter, and G. Gerardi, Appl. Phys. Lett. **63**, 920 (1993). "*Nature of P_b-like dangling-orbital centers in luminescent porous silicon*"

[254] D. Andsager, J. M. Hetrick, J. Hilliard, and M. H. Nayfeh, J. Appl. Phys. **77**, 4399 (1995). "*Diffusion of copper in porous silicon*"

[255] L. Levin, T. Werber, A. Katsman, Z. Atzmon, and A. Ginzburg, Solid State Phenom. **41**, 253 (1995). "*Controlled formation of intermediate phases in the Cu-Si system*"

[256] C. A. Chang, J. Appl. Phys. **67**, 566 (1990). "*Formation of copper silicides from Cu (100)/Si(100) and Cu(111)/Si(111) structures*"

[257] T. Ito, A. Yamama, and A. Hiraki, Appl. Surf. Sci. **41/42**, 301 (1989). "*Silicidation of porous silicon and its application for the fabrication of a buried metal layer*"

[258] T. Ito, A. Hiraki, and M. Satou, Appl. Phys. Sci. **33/34**, 1127 (1988). "*Metal reactions to anodized porous silicon crystals*"

[259] N. OoKubo, H. Ono, Y. Ochiai, Y. Mochizuki, and S. Matsui, Appl. Phys. Lett. **61**, 940 (1992). "*Effects of thermal annealing on porous silicon photoluminescence dynamics*"

ATTENTION: The Singapore Copyright Act applies to the use of this document. Nanyang Technological University Library

[260] M. B. Robinson, A. C. Dillon, D. R. Haynes, and S. M. George, Appl. Phys. Lett. **61**, 1414 (1992). "*Effect of thermal annealing and surface coverage on porous silicon photoluminescence*"

[261] H. Sugiyama and O. Nittono, Jpn. J. Appl. Phys. **28**, L2013 (1989). "*Annealing effect on lattice distortion in anodized porous silicon layers*"

[262] P. Gupta, V. L. Colvin, and S. M. George, Phys. Rev. B **37**, 8234 (1988). "*Hydrogen desorption kinetics from monohydride and dihydride species on silicon surfaces"*

[263] B. K. Meyer, V. Petrova-Koch, T. Muschik, H. Linke, P. Omling, and V. Lehmann, Appl. Phys. Lett. **63**, 1930 (1993). "*Electron spin resonance investigations of oxidized porous silicon*"

[264] T. van Buuren, T. Tiejie, and S. N. Patitsas, Phys. Rev. B **50**, 2719 (1994). "*Effect of thermal annealing on the conduction- and valence- band quantum shifts in porous silicon*"

[265] A. Larré, A. Halimaoui, F. Glovacki, F. Ferrieu, Y. Campidelli, and D. Bensahel, Appl. Phys. Lett. **65**, 1566 (1994). "*In situ spectroscopic ellipsometry of porous silicon layers annealed under ultrahigh vacuum*"

[266] D. Buttard, G. Dolino, C. Faivre, A. Halimaoui, F. Comin, V. Formoso, and L. Ortega, J. Appl. Phys. **85**, 7105 (1999). "*Porous silicon strain during in situ ultrahigh vacuum thermal annealing*"

ATTENTION: The Singapore Copyright Act applies to the use of this document. Nanyang Technological University Library

[267] Z. Gaburro, H. You, and D. Babic, J. Appl. Phys. **84** 6345 (1998). "*Effect of resistivity and current density on photoluminescence in porous silicon produced at low HF concentration*"

[268] K. Kordas, J. Remes, S. Beke, T. Hu, and S. Lappavuori, Appl. Surf. Sci. **178**, 90 (2001). "*Manufacturing of porous silicon: porosity and thickness dependence on electrolyte composition*"

[269] N. Koshida, Nanotechnology **3**, 192 (1992). "*Photoluminescent and electroluminescent properties of porous silicon*"

[270] H. Ono, H. Gomyou, H. Morisaki, S. Nozaki, Y. Show, M. Shimasaki, M. Iwase, and T. Izumi, J. Electrochem. Soc. **140**, L180 (1993). "*Effects of anodization temperature on photoluminescence from porous silicon*"

[271] S. Setzu, G. Lerondel, and R. Romenstain J. Appl. Phys. **84** 3129 (1988). "*Temperature effect on the roughness of the formation interface of p-type porous silicon*"

[272] D. J. Blackwood and Y. Zhang, Electrochim. Act. **48**, 623 (2003). "*The effect of etching temperature on the photoluminescence emitted from, and the morphology of, p-type porous silicon*"

[273] S. Lanfredi and A. C. M. Rodrigues, J. Appl. Phys. **86**, 2215 (1999). "*Impedance spectroscopy study of the electrical conductivity and dielectric constant of polycrystalline* $LiNbO_3$"; D. Ivanov, M. Caron, L. Ouellet, S. Blain, N. Hendricks, and J. Currie, J. Appl. Phys. **77**, 2666 (1995). "*Structural and dielectric properties of spin-on barium-strontium titanate thin films*"; S. Saha and S. B.

ATTENTION: The Singapore Copyright Act applies to the use of this document. Nanyang Technological University Library

Krupanidhi, J. Appl. Phys. **87**, 849 (2000). "*Dielectric response in pulsed laser ablated (Ba,Sr)TiO_3 thin films*"

[274] N. Hirose and A. R. West, J. Am. Ceram. Soc. **76**, 1633 (1996). "*Impedance spectroscopy of undoped BaTiO3 ceramics*"

[275] O. K. Varghese and L. K. Malhotra, J. Appl. Phys. **87**, 7457 (2000). "*Studies of ambient dependent electrical behavior of nanocrystalline SnO_2 thin films using impedance spectroscopy*"

[276] M. I. Lanstrass and K. V. Ravi, Appl. Phys. Lett. **55**, 1391 (1989). "*Hydrogen passivation of electrically active defects in diamond*"

[277] Y. Mori, N. Eimori, A. Hatta, T. Ito, and A. Hiraki, Jpn. J. Appl. Phys., Part 2 **31**, L1718 (1992). "*Effect of ambient on the surface resistance of diamond films during cooling after deposition*"

[278] S. S. N. Bharadwaja and S. B. Krupanidhi, Mater. Sci. Eng., B **78**, 75 (2000). "*Dielectric relaxation in antiferroelectric multigrain $PbZrO_3$ thin films*"

[279] E. Axelrod, A. Givant, J. Shappir, Y. Feldman, and A. Sa'ar, Phys. Rev. B **65**, 165429 (2002). "*Dielectric relaxation and transport in porous silicon*"; J. Non-Cryst. Solids **305**, 235 (2002). "*Dielectric relaxation and porosity determination of porous silicon*"

[280] M. A. L. Nobre and S. Lanfredi, Mater. Lett. **47**, 362 (2001). "*Dielectric properties of $Bi_3Zn_2Sb_3O_{14}$ ceramics at high temperature*"

[281] A. K. Jonscher, J. Mater. Sci. **16**, 2037 (1981). "*A new understanding of the dielectric relaxation of solids*"

ATTENTION: The Singapore Copyright Act applies to the use of this document. Nanyang Technological University Library

[282] F. J. Blatt, *Physics of Electronic Conduction in Solids*, (McGraw–Hill, New York, 1968).

[283] A. K. Jonscher, Nature **267**, 673 (1977). "*The 'universal' dielectric response*"

[284] W. H. Jung, J. Appl. Phys. **90**, 2455 (2001). "*Dielectric loss anomaly and polaron hopping conduction of* $Gd_{1/3}Sr_{2/3}FeO_3$"

[285] R. Tsu, D. Babic, and L. Ioriatti, Jr., J. Appl. Phys. **82**, 1327 (1997). "*Simple model for the dielectric constant of nanoscale silicon particle*"